

NOVEL APPROACHES IN IMAGING AND IMAGE-GUIDED
THERAPY: MICROFABRICATION, QUANTITATIVE
DIAGNOSTIC METHODS, AND A MODEL OF
LYMPHANGIOGENESIS

DISSERTATION

Presented in Partial Fulfillment of the Requirements for the
Degree Doctor of Philosophy in the Graduate School of
The Ohio State University

By

Robert F. Short, M.S.

The Ohio State University
2005

Dissertation Committee:

Derek Hansford, Ph.D. Advisor

Frederick Long, M.D.

Alan Litsky, M.D., Sc.D.

William Shiels II, D.O.

Approved by

Advisor

Graduate Program in Biomedical Engineering

Copyright by
Robert F. Short
2005

ABSTRACT

The work presented herein describes the investigation in several key areas related to imaging and image-guided therapy. Each area is of interest for advancing the state of the art and development of new techniques in image-guided therapy. First, the rationale and approaches for microfabrication of microparticles is advanced. A technique for microfabrication of biodegradable microparticles of tailorable geometry and monodisperse size is described as well as efforts and the design of an experimental set-up to optimize production. The applications of such microparticles as drug delivery vehicles or as agents for embolization (or both as in chemoembolization) make them a promising technology in image-guided therapy.

A second related focus of study is presented in the area of quantitative diagnostics. Combining imaging techniques and analysis algorithms can both identify and quantify disease states. Precise determination the extent of disease can be used to gauge response to therapy, i.e. provide outcome measures to develop new therapies, including those advanced by image-guidance. A novel imaging method for identification of disease states of the major airways and lungs in pediatric populations is presented.

Lastly, an animal model suitable for the testing of therapies directed against lymphatic malformations and lymphangiogenesis is presented. This method of site-specific induction of *de novo* lymphatic malformations (LMs) expressing specific growth

factor receptors will allow investigations in the function and formation of lymphatic vessels. Macrocystic LMs observed in this model are shown to be large enough to target using current image-guided approaches (sclerotherapy) to optimize treatment capabilities. Microcystic LMs are also induced in this model, which might allow development of therapy against this variant. The LMs cysts have promise as bioreactors to test particle-based therapies directed against lymphatic endothelium.

Each of the presented areas has bearing for future advancements in the field of image-guided therapy. An understanding of the research in these areas will allow for appreciation and perhaps development of future innovations in imaging and image-guided therapy.

Dedicated to my mother and father.

ACKNOWLEDGMENTS

I wish to thank my biomedical engineering advisor Professor Derek Hansford for his enthusiasm, creativity, and support. I am grateful to Professor Alan Litsky for his sage advice and steady accessibility. I remain indebted to Dr. Frederick Long for introducing me to the world of radiology and radiology research. His generosity, patience, and convivial spirit have allowed this work and prompted the birth of a career. I am thankful to Dr. William Shiels, a kindred spirit and mentor, whose creative vision and backing afforded me the opportunity to pursue this body of work; whose gusto inspired motivation; and whose wisdom has guided me along the way.

I wish to thank Nicholas Ferrell for his assistance with microfabrication, and Jing Jiao Guan for his ingenuity and assistance with particle microfabrication; Jim Cooper, D.V.M, Ph.D and his staff for their assistance in animal work; Thomas J. Sferra, M.D. for use of his lab and advice in molecular studies, and Kathy Nicol, M.D. for help with pathology.

I am grateful for my friends' faith in me. I am thankful to my parents, Kevin and Roxie Short, and to my brother Greg Short, for fostering my fortitude and for their enthusiasm for my success. In particular, I must acknowledge the love and support of my fiancée Jeanna Knoble, M.D., who understood my detour and helped bear the burden.

This work was supported in parts by the following: Radiological Society of North America Scholar Assistant Grant; The NCI Unconventional Innovations Program; and The Society of Pediatric Radiology Research and Education Foundation, and the Children's Radiological Institute, Columbus, Ohio.

VITA

- May 14, 1976.....Born—Wright Patterson Air Force Base, Ohio, USA
- June 12, 1998.....B.S. Biomedical Engineering, Wright State University
- June 11, 2002.....M.S. Biomedical Engineering, The Ohio State University
- July 13, 1998—present.....Medical Scientist Program Fellow,
The Ohio State University,
College of Medicine and Public Health, and the
Biomedical Engineering Center
- Jan 2002—present.....Researcher, Children’s Radiological Institute
Columbus, Ohio

FIELDS OF STUDY

Major Fields: Biomedical Engineering
Medicine

Minor Fields: Therapeutic Micro/Nanotechnology, Quantitative Diagnostic Radiology,
Biomaterials, Lymphangiogenesis, Nanomedicine, Drug Delivery

TABLE OF CONTENTS

Abstract.....	ii
Dedication.....	iv
Acknowledgements.....	v
Vita.....	vi
List of Tables.....	x
List of Figures.....	xi
Chapters:	
1. Introduction.....	1
2. Microfabrication and drug delivery.....	7
2.1 Overview.....	7
2.2 Background.....	8
2.3 Promise of microfabrication technology.....	12
2.4 Advantages of microfabricated particles.....	13
2.5 Selected microfabricated devices and strategies in development.....	17
2.5.1 Nanopore based devices.....	17
2.5.2 Microfabricated capped reservoirs:.....	22

2.5.3	Free-form fabrication (3-D printing) devices:	28
2.5.4	Conclusion.....	33
2.6	Production of spherical microparticles of differing porosity using emulsion methods.....	36
2.7	Microfabrication of polymeric microparticles of specific size and geometry for biomedical applications.....	42
2.7.1	Background.....	42
2.7.2	Methods.....	47
2.7.3	Results.....	50
2.7.4	Key considerations identified for MTM process and improvements made.....	51
2.7.5	Project goals not accomplished and how they might be addressed.....	61
2.7.6	Potential experiments for evaluating particle biointeractions.....	64
2.7.7	Conclusions.....	69
3.	Quantitative diagnostics using noninvasive controlled ventilation computed tomography in infants and young children overview.....	94
4.	Noninvasive quantification of tracheal distension and geometry for identification of tracheomalacia and main airway pathology	101
5.	Air trapping as early indicator of obstructive lung disease in infants and young children with cystic fibrosis: comparison of quantitative thin-section CT and pulmonary function tests.....	154

6.	Site-specific induction of lymphatic malformations: an animal model for image-guided therapy and lymphangiogenesis.....	179
7.	Bibliography.....	201

LIST OF TABLES

Table	Page
4.1 Patient characteristics used as normal reference group.....	121
4.2 Patient characteristics of tracheomalacia group.....	123
4.3 P values from comparisons of static and dynamic (%changes) measurements of tracheal dimensions, distension and indicators of shape for NL, CF, TM groups.....	125
5.1 CT correlations with pulmonary function tests.....	171
5.2 Correlation of degree of visual air trapping with abnormal CT findings and PFT measures.....	172
6.1 Sclerotherapy agents used for treatment of lymphatic malformations.....	190

LIST OF FIGURES

Figure	Page
2.1	Current strategies and geometries of self-assembled particulate controlled drug delivery devices.....11
2.2	Schematic showing the difference in contact area for planar and self-assembled spherical endovascular drug delivery devices on endothelium.....14
2.3	Examples of envisioned geometries of microfabricated controlled drug delivery devices using traditional microfabrication processes.....16
2.4	Microfabrication technique for production of a of a drug delivery capsule with nanosized pores.....18
2.5	Capsule being implanted via robotic surgery into the pericardium.....20
2.6	Schematic of the biocapsule for immunoisolation of transplanted cells.....21
2.7	Microchip device and reservoirs.....23
2.8	Steps necessary to fabricate the microchip.....26
2.9	Release profiles achieved by galvanic upcapping of the gold reseviors.....27
2.10	Operation of the 3DP Therics, Inc., machine.....29

2.11	Therics, Inc., schematic of a fully biodegradable implant.....	30
2.12	Strategies for production of implantable drug delivery devices.....	32
2.13	Microparticle produced using emulsion solvent evaporation.....	39
2.14	Microparticle produced using emulsion solvent extraction.....	39
2.15	Steps in the photolithography process for production of a mold master.....	73
2.16	Schematic of photolithography process in 3-D.....	75
2.17	Schematic of photolithography process in 2-D.....	75
2.18	Steps for production of PDMS mold.....	76
2.19	Mold (stamp) production using soft lithography (schematic).....	77
2.20	Schematic of the two-stamp MTM process.....	78
2.21	Experimental set-up for optimizing the MTM process.....	79
2.22	Detail of heat-press.....	80
2.23	Sacrificial stamp from early MTM efforts (PPMA, 5-micron circles).....	81
2.24	Fluorescence micrograph showing embedded PLGA particles.....	82

2.25	Fluorescence micrograph of properly transferred sacrificial stamp.....	83
2.26	Light micrograph of sacrificial stamp for 5 μm circles.....	84
2.27	Fluorescence micrograph of large area of 10 micron square PCL particles before release.....	85
2.28	Scanning electron micrograph of 10 micron PCL squares on sacrificial layer...	86
2.29	5 micron PCL circles being released in water.....	87
2.30	10 micron PLGA squares being released in water.....	87
2.31	Light micrograph of 2 μm PLGA circular particles.....	88
2.32	5 μm PCL circles stamped on sacrificial layer.....	88
2.33	OSU particles produced by MTM process.....	89
2.34	Particles with model functional groups attached.....	90
3.1	Apparatus for non-invasive induction of transient apnea during CVCT.....	97
3.2	CVCT being performed on a child.....	98
3.3	Infant pulmonary function test (IPFT) device.....	99
4.1	Apparatus used in CVCT.....	120
4.2	Trachea areas at full inflation (A_i) with 25 cm H_2O mask pressure.....	126

4.3	Trachea areas at paused expiration (A_e) with 0 cm H_2O mask pressure.....	127
4.4.	Tracheal area distension (%) as a function of length.....	128
4.5	Tracheal sagittal diameter distension (%) as a function of length.....	129
4.6	Method for calculation of circularity.....	130
4.7	Normalized circularity of the trachea by length during paused inspiration.....	131
4.8	Normalized circularity of the trachea by length during paused expiration.....	132
4.9	Quantitative analysis curves of a normal trachea using CVCT.....	134
4.10	Quantitative analysis curves of a trachea in a patient with cystic fibrosis.....	136
4.11	Quantitative analysis curves of the trachea using CVCT in a patient with innominate artery syndrome.....	138
4.12	Quantitative analysis curves of the trachea using CVCT in a patient with a right-sided aortic arch.....	140
4.13	CVCT images of the patient with the right-sided aortic arch.....	141
4.14	Quantitative analysis curves of the trachea using CVCT in a patient with focal tracheal stenosis.....	143
4.15	Quantitative analysis curves of the trachea using CVCT in a patient with diffuse tracheomalacia.....	145

4.16	Compliance lines of the trachea comparing different conditions.....	146
4.17	Analysis of the trachea using cine CT.....	147
4.18	CVCT analysis of the matched level from figure 4.18.....	148
4.19	Extension of the CVCT technique to tracheobronchomalacia.....	149
4.20	Airways distension in diffuse tracheobronchomalacia.....	150
5.1	Bar graphs showing the associations of air trapping with bronchial abnormalities and mosaic attenuation pattern.....	173
5.2	Scatterplot shows correlation of FEF _{25-75%} values reported as z-scores and percent visual air trapping with linear correlation.....	174
5.3	Scatterplot shows correlation of RV/TLC values reported as z-scores and percent visual air trapping with linear correlation.....	175
5.4	Scatter plot shows correlation of the percent pixels less than -800HU and the residual volume.....	176
6.1	Example of a lymphatic malformation in an infant.....	188
6.2	Cystogram showing treatment of lymphatic malformation by sclerotherapy.....	189
6.3	High resolution ultrasound images of cysts over time.....	191
6.4	High resolution ultrasound image of lymphatic malformation.....	192

6.5	T-2 weighted 4.7 Tesla MRI image of lymphatic malformation.....	192
6.6	Animal facility 4.7/40cm Tesla magnet.....	193
6.7	Pathological specimens from animal model intraperitoneal injections.....	194
6.8	Gross specimens of lymphatic malformations from neck injections.....	195
6.9	Infiltration of LM into the muscle tissues.....	195
6.10	Tissue stained with eosin and flt-4.....	196
6.11	Smooth muscle actin staining of cyst wall.....	197

CHAPTER 1

INTRODUCTION

The dawn of the 21st century heralds a new era in medicine. Recent advances in a multitude of scientific areas are converging to succor medical successes. The recent sequencing of the human genome and the birth of functional genomics have allowed the identification of specific gene locations and sequence with insights into the associated related functions. Efforts have progressed to now include more sophisticated functional proteomics, which denotes the next sublevel of mechanisms in sub-cellular physiology. The extrapolation of this cataloguing to proteins will procure an even more precise understanding of pathophysiology, allowing the engineering of therapeutics to counter disease states. An entirely new discipline—bioinformatics--has developed to hasten discovery, catalogue, unravel and even predict the sequence, structure, and function of genes and proteins. To do so, the discipline relies on advances in computer science and algorithms for pattern recognition and ever-increasing computing power. The related discipline of molecular dynamics, which uses advanced understanding of the physics between molecules (including quantum theory) combined with powerful computer simulations to predict molecular interactions, serves to speed development of clinically useful therapeutic agents through theoretical trial and error.

The emergence of these disciplines offers enormous promise for development of new therapeutic biological agents. Anti-sense oligonucleotides that inactivate pathological genes by blocking expression through complementary binding sequences are being developed as new therapies for diseases. The insertions of new therapeutic genes into the patient's own genetic make-up will effectively allow the autonomous production of the desired therapy. Numerous biological vectors have been attempted for this purpose with only modest success to date (and in some cases very publicized failure). This ability to turn on and turn off gene expression portends to revolutionize the way we approach treatment of disease.

The explosion of the elucidation of sub-cellular pathophysiology in the biological sciences has been accompanied by a simultaneous and equally amazing deluge of advances in the physical sciences in ever-smaller dimensions. These discoveries have spawned the fields of micro and nanotechnology. For various reasons the latter term has been used to describe both fields. The technical definitions for each are implied from their names, i.e. microtechnology refers to study of materials less than 1 millimeter (mm) usually on the order of ~ 100 micrometers. Recall a micrometer represents 1×10^{-6} meters. Nanotechnology—according to a strict definition--refers to the study and manipulation of materials at the nanometer dimension (1×10^{-9} meters) generally ~ 100 nm or smaller. At such small dimensions the physical and chemical characteristics of materials can be significantly different. These unique properties can be exploited for various purposes. The National Institute of Health (NIH) has recently referred to the application of nanotechnology in the diagnosis, treatment, monitoring, or manipulation of biological systems as nanomedicine(1).

The technological innovations of nanotechnology have extreme promise for the field of medicine, a notion recognized by the national funding boards for research in the United States. The National Institutes of Health (NIH, Bethesda, MD) identifies nanomedicine as a key area in its roadmap of new pathways for discovery and the National Cancer Institute (NCI) formally announced a \$144.3 million 5-year Alliance for Nanotechnology in Cancer (*Nature Biotechnology*, 22:11). This follows on the heels of the creation of multi-agency National Nanotechnology Initiative (NNI) called for by the 21st Century Nanotechnology Research and Development Act of 2003 (Public Law 108-153). Admittedly some predicted benefits are overstated; however, the benefits of nanotechnology are being realized in the areas of drug delivery and medical imaging(2, 3). These latter two areas define the mission of the newest branch of the NIH, the National Institute of Biomedical Imaging and Bioengineering (NIBIB), whose 2004 annual budget was \$282.1 million.

While not exclusively focused on nanomedicine, the NIBIB has a strong interest in the field. The special properties of nanotechnology-derived materials are of particular value in imaging as contrast agents. Targeting of specific tissues using special protein ligands is an area of NIH (NIBIB and NCI) focus for therapy and imaging, or ideally both. Addressing the need for quantitative approaches to determine the presence and progression of disease states as well as follow response to therapies (outcome measures) a goal of the NIBIB. A high priority for the organization is the development of suitable animal models of human disease for the development and testing of novel therapies, including those guided by imaging. The basic science of imaging and of image-guided

therapy translates clinically into the fields of radiology and in the latter case, specifically interventional radiology(4).

Much of the promise of the revolutions in the biological sciences of proteomics and gene therapies remain hindered by practical limitations of delivery of the therapeutics themselves. Active targeting of specific tissues through parenteral injection of ligand-mediated binding is has not yet actualized. Either the therapeutic itself is too fragile to survive the difficult environment it must traverse to reach its therapeutic target, or the body reacts to sequester or clear the agent. The limitations are biological in nature, but the problems are essentially engineering constructs. Already there are some successes at overcoming these challenges through nanotechnology(1, 3). Encapsulated therapeutics such as drugs, DNA, proteins, viral vectors, and even entire cells can be directed to the preferred site of action—lymph node, kidney, liver, tumor, etc.—by image-guided injection or endovascular catheter access. Localized delivery through image-guidance has shown success for such therapies(5).

This work contained within this document recognizes and attempts to address several of the problems presented by the integration of nanotechnology in medicine and deficiencies recognized by the branches of the NIH. It stands to reason that the most likely and greatest cumulative benefit can be derived in the study of pediatric imaging and image-guided therapy. Namely, genetic disorders are generally manifest early in life causing significant morbidity and mortality; thus early treatment with gene therapy provides greatest benefit in both economic and human costs. Quantitative means for monitoring the response to such therapies that minimize risks to the patient will be required. Novel approaches for the testing of such therapeutics will be required. This

document serves to demonstrate how each might be accomplished in the study of imaging and image-guided therapy.

The first area details work with development of polymeric, degradable microparticulate drug delivery systems. In a distinct but related area a development of means for quantifying and monitoring pediatric airway disease is discussed as well as a rationale for minimization of ionizing radiation to patients. Work is presented detailing a novel model of lymphatic malformations and lymphangiogenesis. This model may prove ideal for testing of image-guided therapies and nanomedicines directed at pathophysiology of the lymphatic system (*e.g.* lymphatic malformation, lymphangiomatosis, lymphangectesia) or even understanding and preventing the lymphatic metastasis of cancers. Lastly, a brief discussion of future directions and implications for study of imaging and image-guided therapy is related.

REFERENCES

1. Moghimi SM, Hunter AC, Murray JC. Nanomedicine: current status and future prospects. *Faseb J* 2005;19(3):311-30.
2. Koh D-M, Cook GJR, Husband JE. New Horizons in Oncologic Imaging. *N Engl J Med* 2003;348(25):2487-2488.
3. Kayser O, Lemke A, Hernandez-Trejo N. The impact of nanobiotechnology on the development of new drug delivery systems. *Curr Pharm Biotechnol* 2005;6(1):3-5.
4. Carson PL, Giger M, Welch MJ, Halpern H, Kurdziel K, Vannier M, et al. Biomedical Imaging Research Opportunities Workshop: report and recommendations. *Radiology* 2003;229(2):328-39. Epub 2003 Aug 18.
5. Becker GJ. 2000 RSNA annual oration in diagnostic radiology: The future of interventional radiology. *Radiology* 2001;220(2):281-92.

CHAPTER 2

MICROFABRICATION AND DRUG DELIVERY

2.1 Overview

In recent years research advances in the biological sciences have led to intensified needs in the area of controlled drug delivery. The field of controlled drug delivery itself has greatly accelerated both independently and in response to emerging therapies. Controlled drug delivery offers a number of clear therapeutic advantages for therapy including extended dosing, increased patient compliance, minimization of side effects, and protection of or prolonged drug activity *in vivo*. Various strategies have emerged for targeted, site-specific therapy and several are being utilized. To date most, if not all, of these strategies rely on self-assembled (colloidal) carriers such as liposomes and polymeric particulates such as microspheres and microparticles. While these formulations have clear utility, further development is limited by restrictions in manufacturing parameters and geometry. Pragmatic limitations of these strategies may be overcome by innovations in microfabrication. Efforts at producing microdevices for controlled drug delivery are well underway. However, most innovations thus far are

based on forward thinking ideas with the actual device yet to be achieved. The purpose of this review is to highlight some of the accomplishments in the area of microfabricated devices with the emphasis on realized devices that may soon be marketable.

2.2 Background

Controlled drug delivery as a therapeutic innovation is no longer a novel concept. Researchers have long recognized the potential benefits of controlled drug delivery, in medicine as well as other disciplines including foods, cosmetics, pesticides, paper. Beginning in the 1960s and 1970s, early efforts concentrated on achieving zero-order release kinetics to maintain a constant, ideal drug concentration within a given therapeutic window (Santini *et al* 2000). Numerous devices, materials, and strategies have received considerable attention in this regard with varying degrees of success. Implantable drug infusion pumps (Medtronic™) have been clinically realized, as have polymeric implants eluting actives for long-term, reversible female chemical sterilization (Norplant™). These devices have the disadvantage in that both implantation and retrieval are required via rather invasive procedures. Biodegradable implantable polymeric disks (Gliadel™), scaffolds, and hydrogels have been advanced to provide desired controlled release kinetics without the need for retrieval. Recent tissue engineering efforts have focused heavily in this area.

Other more desirable approaches for controlled drug delivery have evolved through encapsulation of agents in particulate formulations such as liposomes and polymeric microspheres and microparticles. Biodegradable polymers such as ϵ -

polycaprolactone (PCL), polylactide/glycolide (PLGA), and others have been researched extensively in this regard. These microparticulate carriers have the advantage of being able to be ingested or injected directly into the bloodstream. Furthermore, in addition to being able to carry a wide variety of agents (drugs, DNA, transfection vectors, cells, etc.) these particles have been increasingly modified to achieve *targeted* drug delivery.

Advances in biochemistry and immunology have allowed the fabrication of monoclonal antibodies and other ligands that can be coupled to the particles (liposomes, micro/nano-spheres/particles) to target specific cell lines such as cancers, improving the efficacy of a given drug while reducing systemic dosages and side-effects.

Clearly, research efforts in controlled drug delivery have moved swiftly in the direction of devices made of resorbable biomaterials for obvious reasons. However, most research in the field has focused on “the chemical and physical properties of the biodegradable polymer matrix” such as degradation times, porosity, improving encapsulation efficiency, etc. Considerable less attention has been given to controlling the “three-dimensional architecture, microstructure, and composition” of such devices. This apparent lack of interest stems from the fact that until quite recently there were no existing methods that offered accurate, reproducible means of controlling these parameters (Wu *et al* 1996). Liposomes offer no control over their geometry: they are very much “take-it-or-leave-it” recipes. Polymeric microparticles prepared by traditional methods (emulsions, spray drying, coacervation, etc.) do afford some flexibility in their microstructure (mainly porosity) with resulting altered release profiles (see below, section 2.2). In these situations, though, protocols can be very sensitive making reproducible products difficult. Also the devices are limited to one of a few strategies for

incorporating the agent of interest into or on the particle. More recent work has focused on creating processes that produce monodisperse batches of particles (all of the same size).

Monodisperse batches of particles produced by such proprietary means are ideal for applications where an exact particle size is desired such as embolization of vessels of a particular size. Clinical applications of such technology include Embospheres™ used for uterine fibroid embolization (UFE), Theraspheres™ used for treatment of hepatocellular carcinomas (HCC). In both cases the goal is to cause death to the pathological tissue by obstructing its blood supply. Embolization is achieved by percutaneously inserting a catheter and advancing it within proximity of the target lesion. Particles are then released into the blood and become lodged in and around the lesion, thereby causing obstruction of blood flow. Particles that are too large may not flow far enough and cause obstruction too close to release and too far from the lesion resulting in healthy tissue destruction. Particles too small could flow through the targeted lesion(s) and lodge in other sensitive areas of the body such as the microvasculature of brain.

More recent designs for larger polymeric implants do often contain geometric considerations; these were initially aimed at just achieving desired release profiles but more recently consider interactions at micro levels. Such progressive design of features at both the macro and micro scale has led to a number of advances in tissue engineering through the creation of smart scaffolds that both induce and support new tissue growth. These early bioengineering successes in the application of microfabrication at a tissue level bode well for the application of microfabrication technology at the cellular and subcellular level.

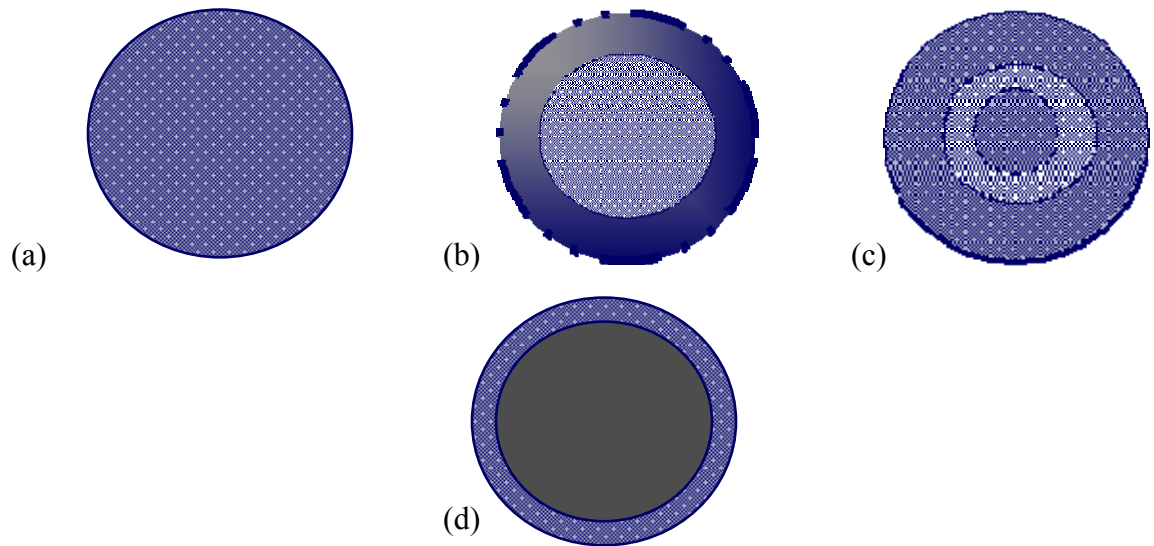


Figure 2.1: Current strategies and geometries of self-assembled particulate controlled drug delivery devices. Whether a liposome or polymeric formulation is employed the same basic configurations are possible, (a) microparticle, a matrix type device that elutes its content as the capsule erodes, (b) microsphere, where a reservoir contains the drug, (c) concentric shell morphology (multi-lamellar), (d) drug absorbed on the surface of particles such as those in a, b, or c.

2.3 The Promise of Microfabrication Technology

A promising alternative to previous controlled drug delivery devices utilizes microfabrication technology. Research has established that cells respond to and express preference for certain microstructural features in the physical environment (Braber *et al* 1995). Current work in tissue engineering is focused at elucidating and exploiting the mechanism of responses to such microfeatures (Desai *et al*, 1999). Microfabricated drug delivery devices offer the advantage of being able to implement microstructural features into the design of the device. Moreover, advances in targeting strategies for earlier drug delivery vehicles are easily applied to microfabricated devices with even greater control of their number, spacing, and diversity. Microfabrication also allows greater flexibility in the possible materials for construction of the device. Microfabricated controlled drug delivery devices therefore make promising candidates for clinical use.

Devices of the future will likely incorporate micro pumping mechanisms, valves, and other moving parts for very sophisticated micromachined devices. Forward-thinking microfabrication and microfluidics research for such components is already well underway (Bohm *et al* 1999) as is the rush to patent ideas to be developed. Currently, though, the devices that exhibit realistic promise for the most immediate success (i.e. clinical use), however, do not tend to rely on elaborate designs (i.e. contain no moving parts). Instead, these devices tend to exploit more passive features of microfabrication technologies, such as the ability to fabricate very defined diffusion channels with

predictable diffusion characteristics. The focus of the remainder of this review is to highlight a sampling of these promising microfabricated controlled drug delivery devices with special consideration given to achievable geometries as well as their manufacture, application, development.

Broad and sweeping claims made by patents filed for microfabricated controlled drug delivery are suspect in that a device need not actually exist to be patented. This shortcoming complicates the investigation and reporting of the status quo of development of microfabricated devices, but does give some insight as to what current devices may evolve into. Presented below is a sampling of some examples of how microfabrication techniques can be applied to engineer drug delivery devices.

2.4 The Advantages of Microfabricated Particles

As mentioned above, self-assembled or colloidal particles have been studied extensively for controlled drug delivery with various loading, targeting, and triggering strategies have been realized for use with them. When compared to microfabricated particles, these self-assembled particles have significant disadvantages. One such constraint is their spherical nature. This geometry results in a couple of disadvantages for given applications. One, the physical contact area spherical particles with a target cell is less than what might be achieved with a planar particle, as shown below in figure 2.2.

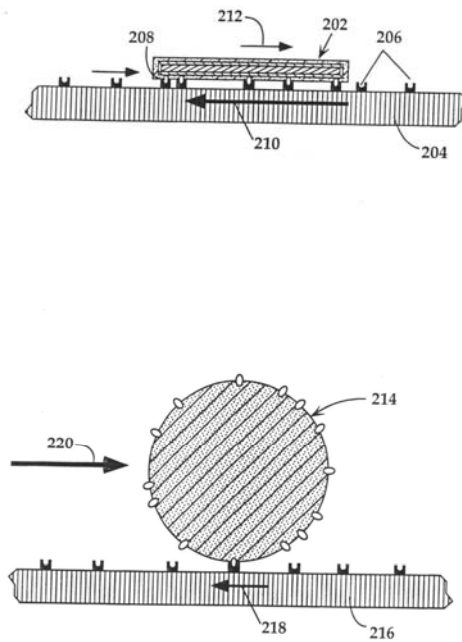


Figure 2.2: Schematic showing the difference in contact area for planar (top) and self-assembled spherical endovascular drug delivery devices on endothelium (from reference 6).

This limitation might affect adhesion and therefore targeting to a specific cell or tissue. Also, since there is less surface area in direct contact with the cell of interest, less of the active agent being carried would be released directly onto the cell. This also means that

although the self-assembled carrier might target the cell(s) of interest, the carrier contents may be released more systemically if, for example, the particle were attached to an endothelial cell in the lumen of a vessel. Once conjugated, a planar (microfabricated) device could deliver its contents (proteins, drugs, etc.) in a vectored fashion directly onto the cell. This prevents loss of the agent of interest to denaturing by plasma proteins or convective flow of the blood. Furthermore, a planar particle could have more therapeutic blocking antibodies on its surface in close proximity to act as a “super-antagonist/agonist” for a given cell (or tighter adhesion). Also of great advantage is that microfabrication surface modification technology allows the attachment of multiple different functional groups at discrete locations, whereas self-assembled particles generally do not. As a corollary this means that a single device could include multiple therapeutic agents as seen in a microchip device described below. In summary, microfabrication offers several distinct advantages in controlled drug delivery. For a given device:

- 1) Discrete geometries can be exploited to increase interaction with the cell
- 2) Multiple therapeutics can be incorporated for release with different release profiles
- 3) A wide range of device materials can be considered
- 4) Different functional groups can be attached at specific locations for targeting, therapy, or avoidance of immune detection.

Some of the possible geometries for a given device are presented from U.S. patent number 6,107,102 (Ferrari, 2000) in figure 3.

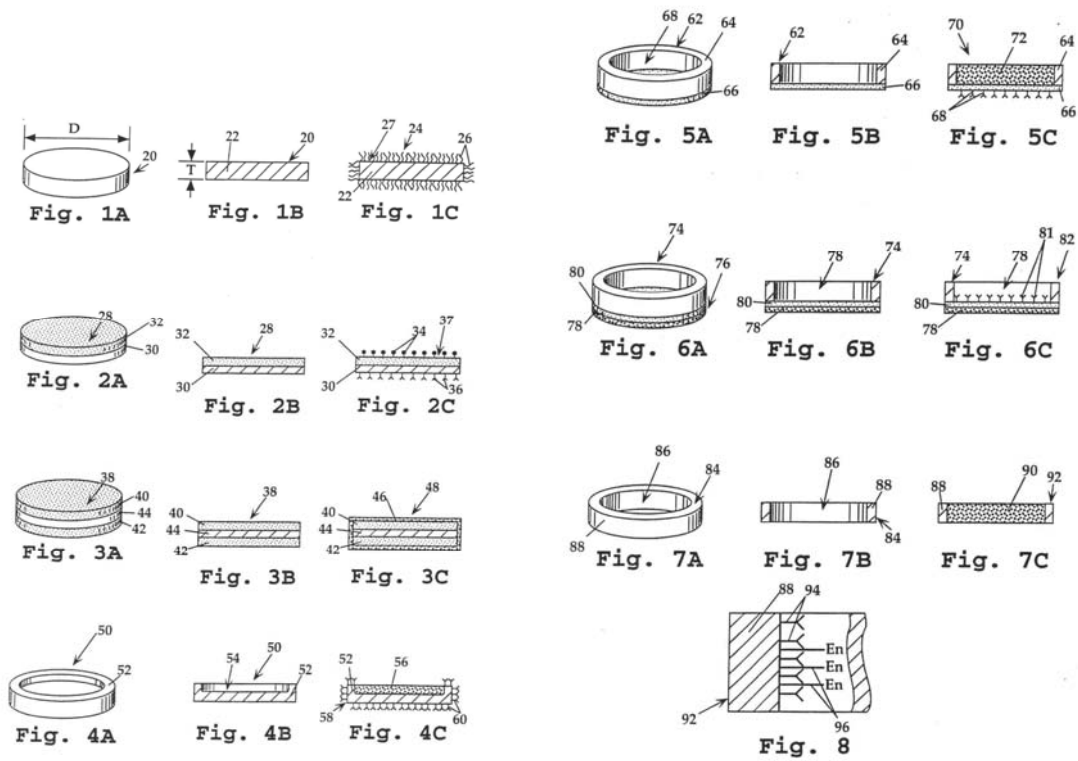


Figure 2.3: Some examples of envisioned geometries of microfabricated controlled drug delivery devices using traditional microfabrication processes. As shown, the devices are planar with the possibility of various 2-D geometries. Also shown are some of the strategies for multi-lamellar structures.

2.5 Selected Devices and Strategies in Development

2.5.1 Nanopore based devices

As shown above, the techniques of microfabrication (photolithography, chemical vapor deposition, reactive ion etching, plasma etching, X-ray and/or electron beam lithography) are well established to allow the fabrication of any number of possible designs for drug delivery capsules. Critical to enabling this technology was the development of reproducible protocols that allowed the design and fabrication of membrane pores in the tens of nanometer range. One such protocol is shown below.

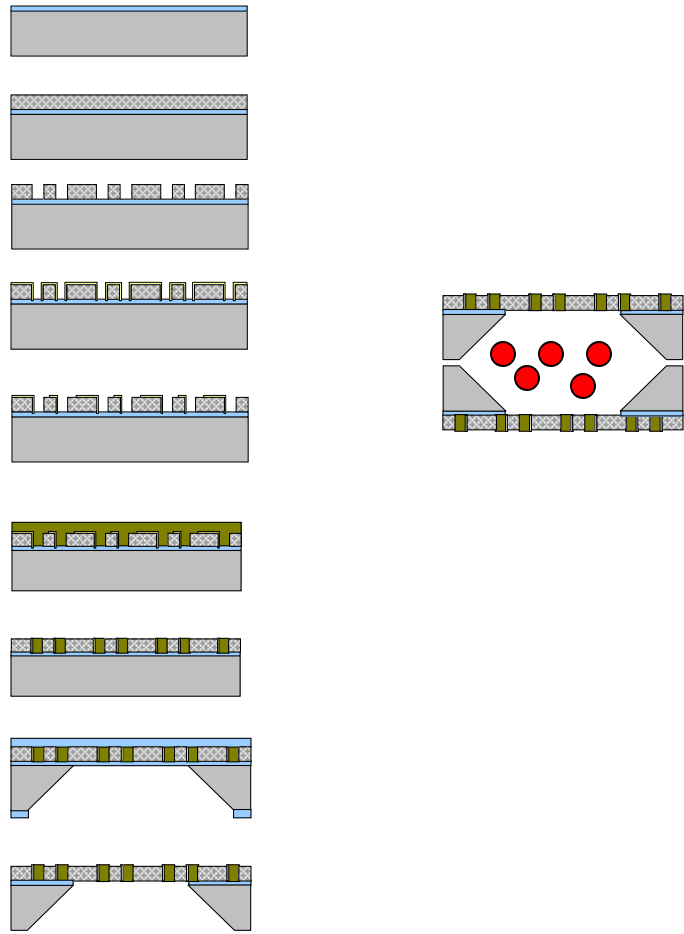


Figure 2.4: Schematic flow chart showing microfabrication technique for production of a drug delivery capsule with nanosized pores through use of sacrificial layers and selective etching. The left side shows how one half of the capsule is produced. The once loaded (with therapeutic agent or cells, represented in red) the capsule is completed by bonding two halves together (right).

Creating membranes with specifiable pore dimensions allows two very interesting properties to be exploited:

- 1) The membranes can be semi-permeable, and
- 2) Diffusion rates through the membrane can be precisely controlled.

The latter allows the fabrication of a microchip type device or particles that can be implanted to deliver almost any agent of interest at a specific rate over extended periods of time. Empirical studies have been conducted documenting different release profiles for various pore sizes, configurations, and materials. Intense efforts in microfluidics research are aimed at developing a predictive model for such diffusion channels. One visionary example of single device application is the Angiochip in development at Ohio State University (figure 2.5).

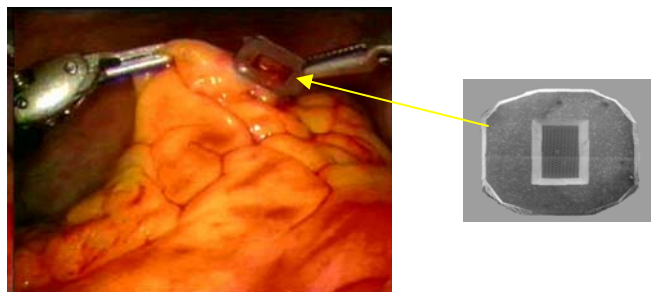


Figure 2.5: Example of microfabricated drug delivery capsule being implanted via robotic surgery into the pericardium. In theory, the capsule could be loaded with substances to promote angiogenesis in the ischemic heart (e.g. VEGF) for the purpose of growing new vessels to increase oxygen supply to the myocardium.

This device might be implanted following a cardiac ischemia to encourage the formation of new blood vessels to supply the heart with oxygen. Another strategy is to employ a suspension of millions of devices might be injected or implanted. The eventual hope is that such tiny particles can be made “smart” by attachment of chemical ligands for targeting and therapy. Another strategy being championed by iMEDD, also yet to be proven, is oral delivery of peptides and proteins that traditionally can only be administered by injection because the gut breaks down such compounds (Oral-

MEDDS™). The simple strategy calls for the use of multiple features within the same device such targeting/binding agents, transport enhancers, and the agent of interest. Similar and more complicated strategies are envisioned for controlled drug delivery applications, but have yet to be developed.

Of particular interest is the fact that the semi-permeable nature of microfabricated nanoporous membranes can be exploited to construct immunoisolation chambers for the implantation of live, responsive yet immunoisolated cells.

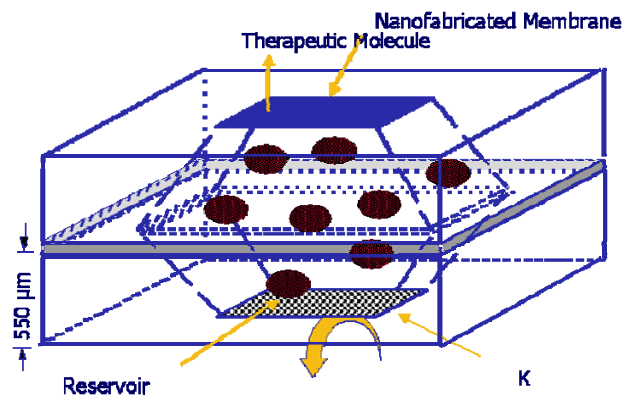


Figure 2.6: Schematic of the biocapsule for immunoisolation of transplanted cells. Metabolites can pass freely, but immune molecules are excluded.

Such a “biocapsule” consists of two microfabricated membranes bonded together with the desired cells inside. These biocapsules have already been tested for treatment of diabetes in proof-of-principle studies showing the viability of the cells and their ability to release insulin in response to stimuli. The membranes on the top and bottom of the capsule have pores designed to be large enough that allow necessary metabolites (insulin, glucose, oxygen, carbon dioxide) to diffuse in and out of the chamber. However, the pores are sufficiently small to prevent immune components from passing and affecting the transplanted cells inside the biocapsule (Desai *et al* 1999). The result is the ability to create a living controlled drug delivery system that continually senses and responds to the patient’s physiological state. In essence, a person is able to receive thousands or millions of tiny transplants without fear of rejection by the immune system or immunosuppressive therapy.

2.5.2 Microfabricated Capped Reservoirs: MicroCHIPS, Inc.

A controlled-release microchip has been developed to provide complex release patterns of a single or multiple chemicals from a single device. The theory behind the design takes advantage of now standard microfabrication technology to fabricate a solid-state silicon microchip that releases its contents on demand. Such a device consists of an array of microfabricated reservoirs that house tiny amounts of a given substance. A degradable material that erodes passively (degradable polymer) or on demand (galvanic erosion) caps these reservoirs. By design of the channel parameters, their number, and

contents different release profiles can be achieved by intelligent “uncapping” of these reservoirs. A prototype of this device was used to demonstrate controllable release profiles (continuous and pulsatile) for both single and multiple substances.

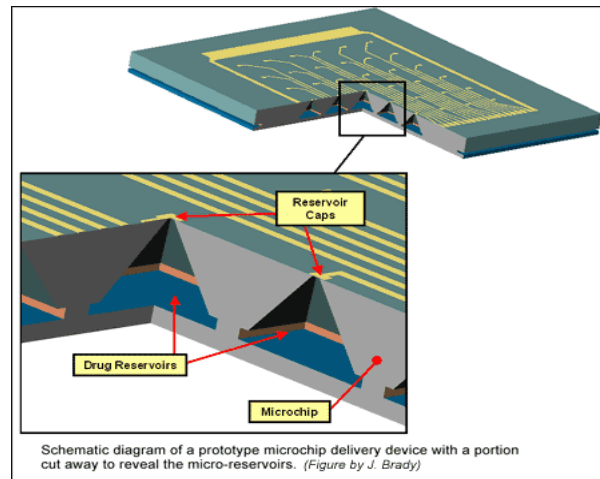


Figure 2.7: Schematic from microCHIPS, Inc., showing microchip device and reservoirs.

The prototype was constructed as detailed in figure 2.9. The prototype device contained 34 separate 40-60 μm -square reservoirs on a 17 mm x 17 mm silicon wafer. It is possible to fabricate up to 1400 such reservoirs at this dime-sized dimensions. These reservoirs extended through the thickness of the wafer and were capable of holding a volume of ~ 25 nanoliters. These were capped through microfabrication methods with gold electrodes on the smaller reservoir opening. The larger opening was utilized as an access port to fill the reservoirs using Inkjet printing technology and then capped using silicon nitride. The

gold caps were made to erode on demand by applying voltage (1.04 V) that caused galvanic erosion. Essentially, the gold overlaying the reservoirs reacts to the applied voltage by losing some of its electrons. When the gold is oxidized in the presence of chloride ions (as in the body), it forms soluble complexes causing the surface to dissolve. As shown in figure 2.10, the prototype was used to demonstrate that varying amounts of chemical substances in various states (solid, liquid, gel) can be released in solution in numerous release profiles. Using microfabricated reservoirs in this way, a single device can be made that accomplishes the release of one or several drugs in either pulsatile or continuous manners, sequentially or simultaneously. Visions of grandeur for this strategy include coupling of the device to a microbattery and microprocessor to program release profiles (as would be required for gold-capped reservoirs), external activation through antenna to elicit release, or integration of biosensors to form a closed-loop, responsive, autonomous drug delivery system (Santini *et al* 1999).

Figure 2.8: Schematic showing the steps necessary to fabricate the microCHIP, Inc., delivery device. Fabrication begins by deposition of $\sim 0.12 \mu\text{m}$ of silicon nitride on both sides of a 100 silicon wafer using a vertical tube reactor. Photolithography is used to pattern one wafer side and electron cyclotron resonance (ECR) enhanced reactive ion etching (RIE) allows the wafer to be cut into 17 mm square pieces. Silicon nitride is used as an etch mask, allowing for KOH at 85 degrees C to anisotropically etch square pyramidal reservoirs along the (111) crystal planes through the wafer to the silicon nitride film on the opposite side. Silicon nitride is later used to cap the backside of the reservoirs after filling. Fabrication of the gold electrodes is also shown. These electrodes are deposited ($0.3 \mu\text{m}$ thick, with $0.01 \mu\text{m}$ chromium adhesion layer) and patterned over silicon nitride membranes through electron beam evaporation and lift-off. A $0.6 \mu\text{m}$ silicon dioxide layer is then deposited using plasma enhanced chemical vapor deposition at 350 degrees C. RIE is used on the silicon dioxide to expose the gold anode caps, and to remove the silicon nitride and chromium layers underneath these caps. Also shown is a schematic for the inkjet method of loading the reservoirs.

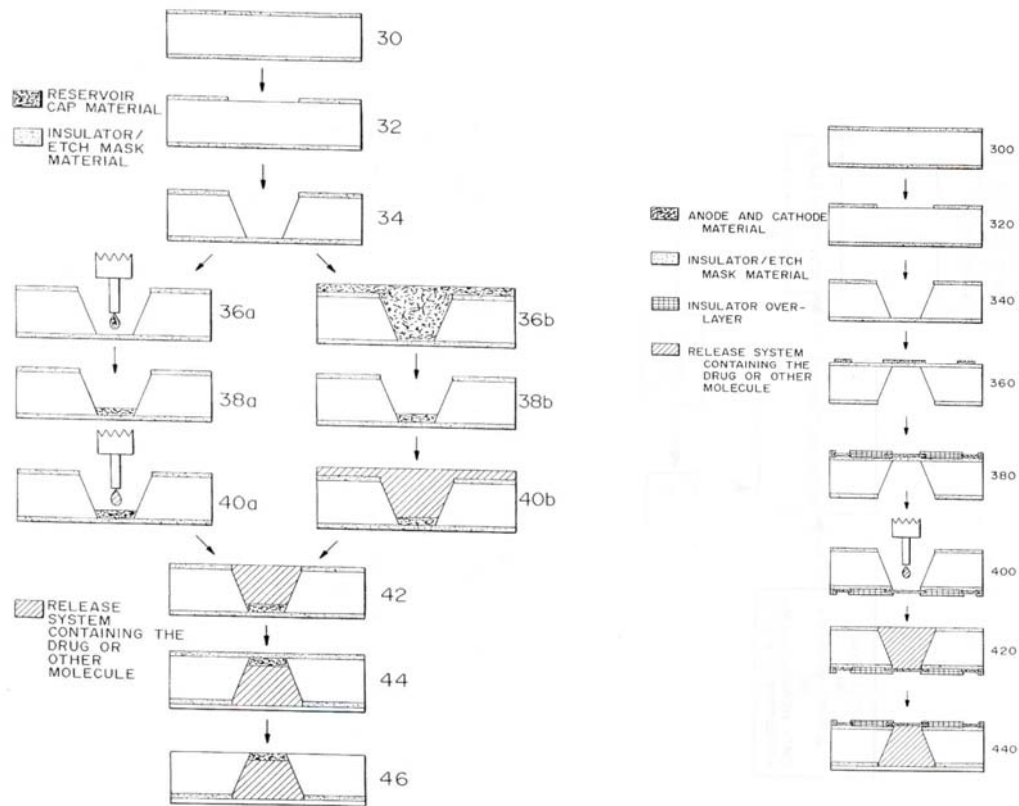


Figure 2.8: Microfabrication schematic of microchip, Inc. device (left) with loading technique (right).

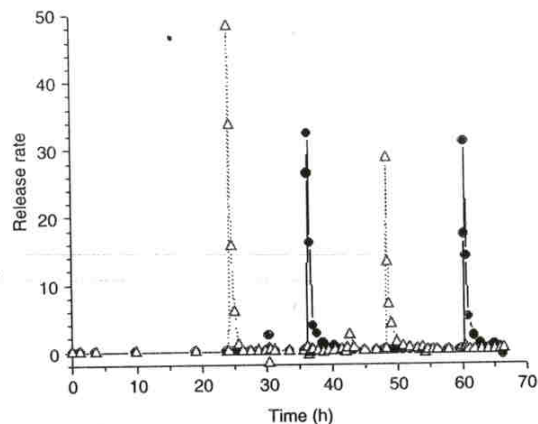


Figure:2.9 Release profiles achieved by galvanic uncapping of the gold reservoirs on the microChips device.

While these innovations are a ways off from realization, the multi-reservoir design has clear application for intelligent controlled drug delivery. Such a device might be used for hormonal delivery, or even implanted in soldiers for release of antidotes in case of chemical attack. The therapeutic utility of such device is limited though in terms of its payload capacity of the reservoirs. Treatments that require large amounts of a substance to be delivered are not good candidates to benefit from this design. Instead, such a device is better suited for carrying highly potent neurotransmitters or hormones that elicit their therapeutic effect in tiny concentrations and pulsatile patterns. Example candidates include highly potent painkillers or analogues of the hormones of the anterior pituitary.

2.5.3 Free-form fabrication (3-D printing) Devices: Therics, Inc.

Therics, Inc is advancing another interesting approach to the fabrication of controlled drug delivery devices. Their approach employs Inkjet technology known as three-dimensional printing (3DP) to create resorbable devices capable of eluting complex release patterns. A three-dimensional device is created through a series of two-dimensional layers laid down as microdrops deposited from an array of printing nozzles. Current technology allows up to 800 microdrops per second to be printed, with each drop being placed within 10 μm of its intended position in space. At this resolution, this allows the fabrication of devices with complex three-dimensional shapes with well-defined features on the micrometer scale. Any number of materials or combinations thereof can be used in this manner to create biodegradable controlled drug delivery devices (Therics, 2000).

The patented 3DP process has been described in detail in the literature. In short, the process utilizes a layered printing process, i.e. adding successive two-dimensional layers creates a three-dimensional product. Each layer is added sequentially by depositing a fine coating of powder on a piston and cylinder containing the powder bed. An appropriate binder material (solvent) eluted from the inkjets selectively joins the new powder layer. The piston lowers the bed and a new powder layer is deposited then selectively bonded. This process continues until the desired device is completely printed.

Finally, unbound powder is removed to yield the final product. This is shown schematically in figure 2.10.

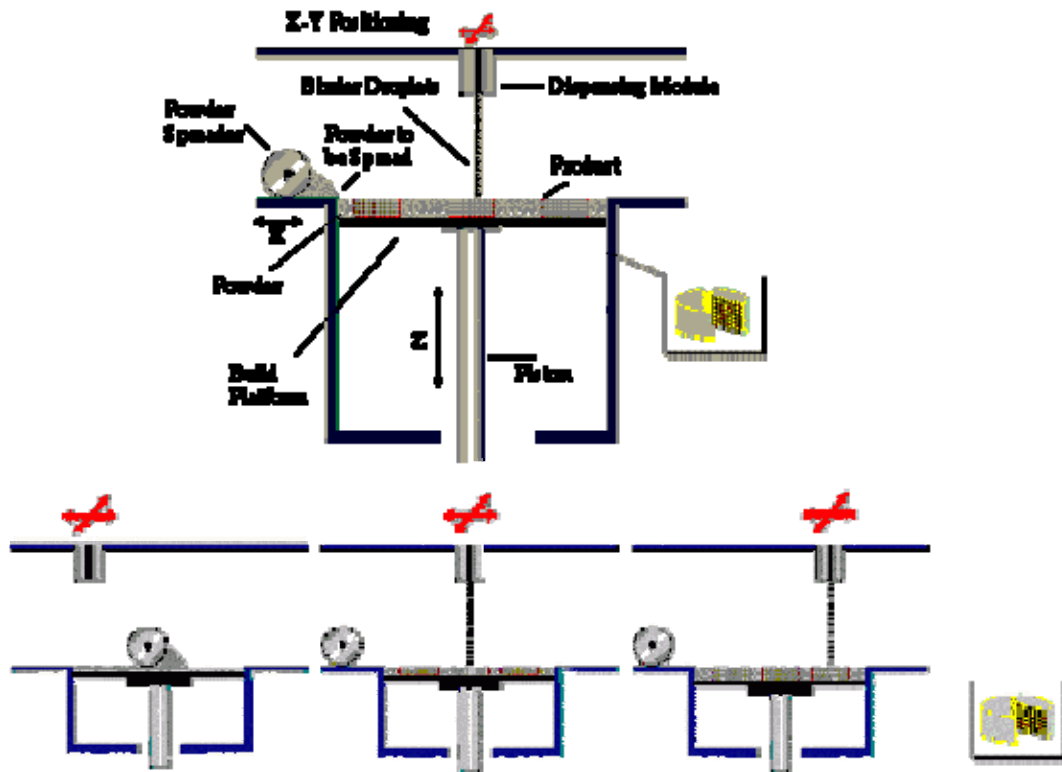


Figure 2.10: Schematic showing the operation of the 3DP Therics, Inc., machine. Layers of powdered material are laid down and bonded by printing nozzles on a piston. The piston moves down and another layer is deposited and bonded appropriately. The process is repeated layer by layer until the 3-dimensional product is produced.

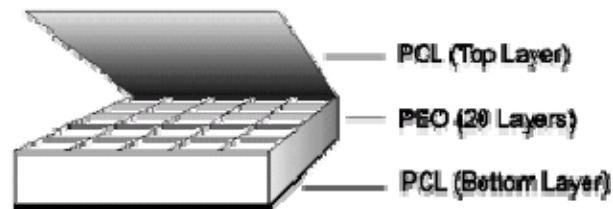


Figure 2.11: Therics, Inc., schematic of a fully biodegradable implantable drug delivery device. The device is composed of 20 polyethylene oxide (PEO) layers sandwiched between two polycaprolactone (PCL) layers. Selective bonding of the PEO layers creates compartments for drugs to be deposited in.

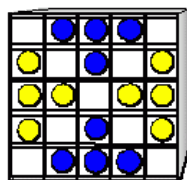
For this device, the powder material consisted of biodegradable polymers (polycaprolactone (PCL) and polyethylene oxide (PEO)) while the binding material typically was a solvent solution of these polymers (chloroform/PCL solution). The top and bottom of the tabular device are made of PCL, a relatively nonresorbable semicrystalline polymer. The interior layers consist of PEO bound by printing binder solutions to form perpendicular walls inside the devices. This creates distinct chambers into which agents to be delivered are deposited during fabrication. (Initial studies,

described below, used dyes). Sheets are formed by repeatedly printing lines directly adjacent to each other. Because the top and bottom sheets (and potentially internal walls) are composed of dense PCL, they serve as diffusion barriers impeding degradation. Not only does this limit diffusion to the plane of the device (PEO layer), but it also allows tailoring of diffusion characteristics through microstructural control of wall thickness and composition.

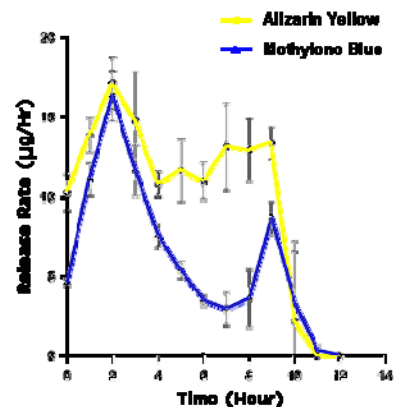
Using this device and 3DP technology, experiments were designed to demonstrate the different release profiles that could be achieved from the same elementary structure by utilizing the effects of various geometric positions, different wall microstructures and composition. A sampling of these structures and the resulting release profiles are given below. The difference in release profiles demonstrates the effect of different printing parameters as well as the spatial positioning of molecules of interest. For example, a slower print speed or double printing for a wall results in increased thickness of that wall and therefore a greater barrier to diffusion (increased diffusion distance). Multiple parallel wall configurations can also be used to customize diffusion characteristics by influencing the rate and extent of water penetration into the barriers (Wu *et al*, 1996). Wall microstructure can be made to be more or less porous by using different binding solutions to affect the tortuosity of the diffusion path. For example, using binders in which the powder layer is less soluble makes a more porous structure.

**Microstructural Control - Symmetric Spatial Distribution
Varying Wall Microstructure**

- Alizarin Yellow
- Methylene Blue
- 4 Lines per Wall
- 2 Lines per Wall
- Unprinted PEO Powder



Binder: 20% PCL-LPS in CHCl_3



**Positional Control - Asymmetric Spatial Distribution
Identical Walls**

- Alizarin Yellow
- Methylene Blue
- 20% PCL-LPS in CHCl_3
- Unprinted PEO Powder

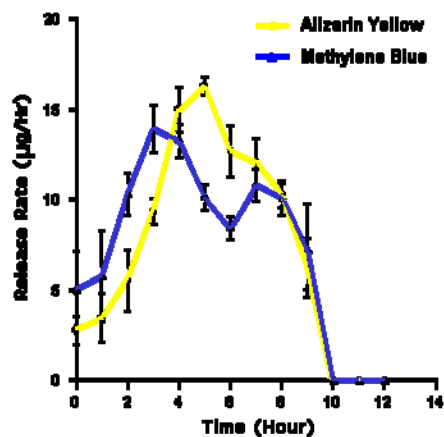
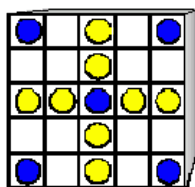


Figure 2.12: Examples of different microfabrication (3-D printing of polymers) strategies for production of implantable drug delivery devices, employing TheriForm™ microfabrication process.

Devices made by 3DP processing are very promising in that multiple diffusion gradients can be produced in the same device to create sophisticated drug release profiles. Through control of three-dimensional position, wall microarchitecture, and overall composition during construction any number of dosing profiles can be achieved. Adding to the appeal of this method is the ability to fabricate complex 3-D structures on macro level. Such constructs are of great interest for reconstructive implants and tissue engineering.

2.5.4 Conclusion

Within the last few decades the field of controlled drug delivery has evolved into its own discipline. The recent sequencing of the human genome and subsequent advances in pharmacology, molecular genetics, proteomics, immunology, pharmacogenetics, etc., will reinforce the need for adequate delivery vehicles to take full advantage of these technologies. Technologies based on various self-assembled beads, particles, and coatings have been developed and many are being utilized with a great deal of promise. However, the practical limits of these technologies will soon be reached or have already. Recent technology based on microfabrication strategies such as those discussed above offers an innovative and viable alternative to continue to pursue the initial goals of the controlled drug delivery with renewed promise. As evidenced above, the foundations for this pursuit have been laid already with novel fabrication strategies and demonstration of functional devices.

REFERENCES

- E. Allemann, J. Leroux, R. Gurny, Polymeric nano- and microparticles for the oral delivery of peptides and peptidomimetics. *Advanced Drug Delivery Reviews* 34, 171-189, (1998).
- G. Barratt, Therapeutic applications of colloidal drug carriers. *PSST* 3(5), 163-171, (2000).
- S. Bohm, W. Olthuis, P. Bergveld, An integrated micromachined electrochemical pump and dosing system, *J. of Biomedical Microdevices* 1:2, 121-130, (1999).
- T.A. Desai, J. Deutsch, D. Motlagh, W. Tan, B. Russell, Microtextured cell culture platforms: biomimetic substrates for the growth of cardiac myocytes and fibroblasts, *J. of Biomedical Microdevices* 2:2, 123-129, (1999).
- T.A. Desai, D.J. Hansford, L. Kulinsky, A.H. Nashat, G. Rais, J. Tu, U. Wang, M. Zhang, M. Ferrari, Nanopore technology for biomedical applications, *J. of Biomedical Microdevices* 2:1, 11-40 (1999).
- Desai, TA et al. Nanoporous Anti-fouling Silicon Membranes for Biosensor Applications. *Biosensors and Bioelectronics* 15, 453-462. 2000.
- Desai TA, Hansford DJ, and Ferrari M. Characterization of Micromachined Silicon Membranes for Immunoisolation and Bioseparation Applications. *J of Memb Science* 159, 221-231. 1999.
- Desai TA, Hansford DJ, Ferrari M, et al. 1999. Nanopore Technology for Biomedical Applications. *Biomedical Microdevices* 2:1, 11-40. M. Ferrari, US Patent No. 6,107,102, (2000).
- R. Kumar, Nano and microparticles as controlled drug delivery devices. *J Pharm Pharmaceut Sci* 3(2), 234-258, (2000).
- M. Larkin, Pharmacy on a microchip looks promising, *The Lancet*, Vol. 353, p. 385, (1999).

F. Martin and C. Grove. Microfabricated Drug Delivery Systems: Concepts to Improve Clinical Benefit, *Biomedical Microdevices* 3:2, 97-108.. 2001.

H. Pinto-Alphandary, A. Andreumont, P. Couvreur, (Review) Targeted delivery of antibiotics using liposomes and nanoparticles: research and applications. *International Journal of Antimicrobial Agents* 13, 155-168, (2000).

J.T. Santini, A.C. Richards, R. Scheidt, M.J. Cima, R. Langer, Microchips as controlled drug-delivery devices, *Angew. Chem. Int. Ed.* 39, 2396-2407, (2000).

J.T. Santini, M.J. Cima, R. Langer, A controlled release microchip, *Nature*, Vol. 397, 335-338, (1999).

J.T. Santini, M.J. Cima, R.S. Langer, US Patent No. 5,797,898, (1998).

J.T. Santini, M.J. Cima, R.S. Langer, US Patent No. 6,123,861, (2000).

R. Service, Silicon chips find role as in vivo pharmacist, *Science*, Vol. 283, p. 619, (1999).

Website: <http://mchips.com/>, Microchips, Inc., (2000).

Website: <http://www.therics.com/>, Therics, Inc., (2000).

Website: <http://192.148.246.31/imeddpr.html>, iMEDD, Inc., (2000).

B.M. Wu, S.W. Borland, R.A. Giordano, L.G. Cima, E.M. Sachs, M.J. Cima, Solid free-form fabrication of drug delivery devices, *J. Cont. Release* 40, 77-87, (1996).

2.6 PRODUCTION OF SPHERICAL MICROPARTICLES OF DIFFERING POROSITY USING EMULSION METHODS

Overview

This section highlights the author's initial work for production of traditional spherical biodegradable polymeric microparticles. These types of particles have been used for delivery of drugs in numerous experimental studies. This work was undertaken to gain understanding of production parameters and results of more traditional polymeric drug delivery particles by emulsion methods. Additionally, the author was able to demonstrate two distinct patterns of porosity by slight variations in the production method, and thus achieve qualitative differences in degradation through hydrolytic cleavage. Numerous studies have shown that deliberate alterations in porosity allow control over drug release characteristics.

Introduction

Biodegradable polymer microparticles of spherical geometry have been investigated for many years now. Many studies have shown advantages of these microparticles in for drug delivery and therapy of diseases. Numerous methods of production exist with entire journals being devoted to the manufacture, modification and application of spherical microparticles (Jain, 2000). The work described below was undertaken to demonstrate production of biodegradable microparticles with simple equipment common to most laboratories.

Methods

Particles were produced according to the protocol described by Chen *et al* using emulsification methods with minor modifications. Polycaprolactone (PCL), molecular weight (MW) of 80,000 (Aldrich, St. Louis, MO, USA) was used in these studies. To prepare the oil phase, 1 gram (g) of PCL was dissolved in 20 mL of methylene chloride or chloroform (Aldrich, St. Louis, MO, USA) using a 25 mL Erlenmeyer flask. An aqueous phase was prepared in an by completely dissolving 2 g of polyvinyl alcohol (88% hydrolyzed, MW~25,000 (Polysciences catalogue #02975, Warrington, PA, USA) and 0.1 mL of Tween 80 (Sigma, St. Louis, MO, USA) in 200 mL of distilled water, using a 500mL Erlenmeyer mask. The oil phase was then added dropwise to the aqueous phase while stirring with a magnetic stir bar on a stir plate. Various trials employed different settings for the stirrer. Mixtures were either 1) stirred with low heat (setting of 2) overnight to evaporate oil phase solvents (solvent evaporation); or 2) stirred similarly

for 10 minutes and then added to 2 liter of distilled water and then stirred overnight (solvent extraction).

Particles were collected by vacuum filtration using a Buchner funnel and filter paper (Whatman membrane filters, Newton, MA, USA). Particles were observed and photographed under light microscopy for general size distribution. Observation of morphology and porosity was made by scanning electron microscopy (SEM) Particles were incubated at in phosphate-buffered-saline (PBS) at 37 degrees centigrade for three weeks and observed for differences in degradation by light microscopy.

Results

Variations in manufacture techniques produced alterations in particle size distributions and morphology. Qualitative differences were observed for differing spin speeds during stirring of the two phases. Higher spin rates tended to produce batches containing increased numbers of smaller particles. These batches also appeared to have overall larger distributions in particle sizes. No differences were noted between particle batches from different solvents used in preparing the oil phase. Particles produced by solvent-extraction in distilled water were noted with SEM to have increased porosity compared to those produced with solvent evaporation (Figure 2.13). After 3 weeks of incubation more of the solvent extraction particles appeared to have degraded.

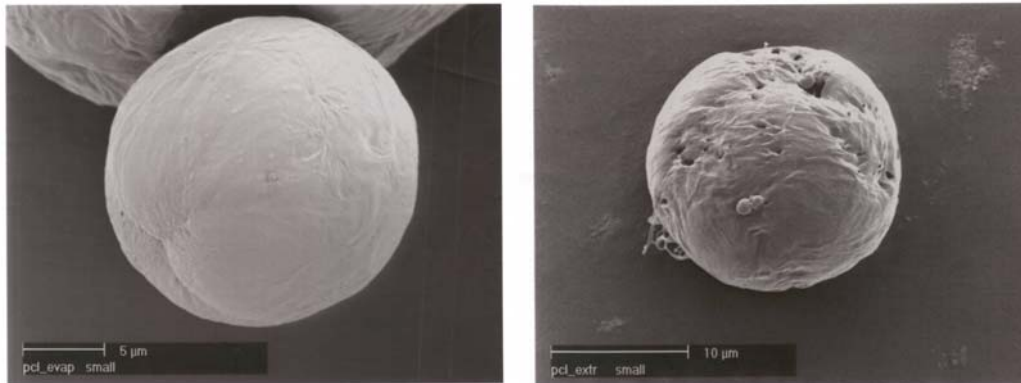


Figure 2.13 (left) and 2.14 (right): Scanning electron micrographs of polycaprolactone microparticles produced using the two different emulsion fabrication techniques.

Particles like those in figure 2.13 were produced using solvent evaporation. Particles like those in figure 2.14 were produced using solvent extraction.

Conclusions

This study was undertaken to gain a simple understanding of production of biodegradable microparticles using emulsion based methods. More elaborate work on emulsion based biodegradable particles has been accomplished elsewhere by others using technical advances and sophisticated equipments. This was primarily a preliminary study in the emulsion-based production of microparticles before attempting to develop polymer microfabrication techniques to produce microparticles of controlled geometries and size distributions. As such there was little emphasis on quantitative results of the production

methods employed. Instead a general understanding of parameters and limitations of emulsion methods was sought. To this end, the goals of the study were accomplished.

REFERENCES

Chen, DR, JZ Bei, SG Wang, Polycaprolactone Microparticles and Their Biodegradation, *Polymer Degradation and Stability*, 2000, 67, 455-459.

Jain RA. The manufacturing techniques of various drug loaded biodegradable poly(lactide-co-glycolide) (PLGA) devices. *Biomaterials* 2000;21(23):2475-90.

2.7 MICROFABRICATION OF POLYMERIC MICROPARTICLES OF SPECIFIC SIZE AND GEOMETRY FOR BIOMEDICAL APPLICATIONS

Overview

This section details the author's studies to develop and optimize a process for microfabrication of polymeric microparticles with specific size and geometry for biomedical applications.

2.7.1 Background

Microencapsulation of therapeutics offers several strategic advantages for drug delivery including sustained release, site-specific delivery, and protection or preservation of delicate agents' therapeutic effects; thus, leading to improved efficacy and reduced toxicity. Microencapsulation technologies to date (e.g. emulsions, atomization, coacervation, etc.) are limited in terms of geometry and uniformity, i.e. to the production of spherical carriers, generally produced in a range of sizes. Enhanced functionality can be obtained by use of other geometries with increased surface area to volume ratio (as in ligand-mediated binding). Adjustment of particle geometries and associated aerodynamics has implications for injections and pulmonary delivery of drugs. Also,

methods for producing monosized batches particles are desirable. Microfabricated particles have many applications including drug delivery, contrast agents for medical imaging, vaccine adjuvants, functional additives for tissue engineering scaffolds, reinforcing fibers for materials applications, and as platforms for more advanced biomedical micromachinery.

In the last few decades, controlled drug delivery has exploded as a field. More recently, entire subdisciplines have evolved such as microencapsulation of therapeutic materials. Literally thousands of articles have been published addressing various materials suitable for encapsulation and associated applications for medical therapy. The advantages of controlled drug delivery through microencapsulation have long been recognized:

- Improved patient compliance
- Improved efficacy
- Prolonged treatment and reduced dosing/interventions (surgery, etc.)
- Reduced toxicity (side effects)
- Patent opportunities/extensions
- Potential for targeted delivery
- Preservation/protection of therapeutic effect of agent

The latter of these advantages has become even more relevant in recent times due to the sequencing of the human genome and the advent of structural genomics. Thousands of new therapies are being advanced in the form of peptides, proteins, gene inserts (DNA),

and gene blockers (antisense oligonucleotides). Such therapies suffer, though, by their immunogenic nature, *i.e.* immune system clearance before their therapeutic potential can be realized. Previous work has shown that protecting these therapeutic agents by microencapsulation is a viable approach for the preservation of therapeutic activity.

A myriad of methods have been devised for microencapsulation, most notably liposomes and polymeric microparticles. Both of these modalities have grown increasingly sophisticated in terms of possible agents that can be included, means of manufacture, and organizational scheme. Several systems have been approved for clinical use, with many more in clinical trials. Even combinations of polymeric microparticles and liposomes have been introduced for therapy. The literature is full of examples of methods for incorporating different drugs into such particulate carriers, their characterization, and their use both *in vivo* and *in vitro*. Whether the encapsulating material is a biopolymer (collagen, chitosan, etc.), synthetic polymer (polycaprolactone (PCL), polylactoglycolide (PLGA), or phospholipids (as in the case of liposomes), all such methods rely on self-assembly of the particle material via some sort of reaction. As such, these methods offer little or no control over the geometry of the particulate carriers. All the microparticles produced are generally spherical in nature or some variant thereof. Moreover, the production process for the particles often results in a varied size distribution and other inconsistencies in particle geometry.

More recently, surface modifications of microparticulate carriers have been advanced to allow tissue-specific targeting of the microparticles and/or increased reticular

endothelial system (RES) evasion. These methods have demonstrated improvements over their predecessors, and some have been approved clinically. However, the adapted particles still suffer from a lack of spatially specific surfaces—chemical adjustment of any portion of the surface of the particles must occur over the entire surface.

This research described attempts to address some of the shortcomings of previous microparticulate carriers. Specifically, development of microfabrication method(s) for the production of microparticles of specific geometries for the purposes of controlled drug delivery is described, as well as the propositions for these particles for use as an improved general platform for controlled drug delivery through microencapsulation. The project intends to explore the effect of particle geometry on cellular/subcellular processes. Current research has made it increasingly clear that physical surface topology/geometry affects cellular processes such as cell-surface attachment and spreading. Speculation regarding future work attempts to address how subcellular particle microgeometry might affect various cell-particle interactions through precise control of particle geometry via microfabrication methods.

Microfabricated particles offer distinct advantages over previous spherical particulates. The flat surface of the particles could allow increased surface area contact with cellular substrates. This increased surface area may allow enhanced adhesion to a particle through an increased number of ligand-mediated contacts. Additionally, this increased surface area contact may allow for significantly more agonist or antagonist function from chemical mediators carried on the surface of such microfabricated

particles. Included in the proposal are plans to make particles uniquely spatially functional, *i.e.* allow for the specific attachment of chemical ligands on just one side of the particles. Not only does this reduce the amount of potentially expensive ligands, but it also reduces the chances of agglutination reactions that might occur with spherical particles bound to cellular substrates. For example, the latter might occur with spherical particles bound at one (or a few) point(s) to vascular endothelial cells with the remaining surface area ligands exposed to the blood stream. Furthermore, plans are outlined to achieve one-sided vectored release of the active agent from the particle. The intended advantage in doing so is to exploit the intimate contact between the particles and their given substrate (cells, etc.). This spatially specific degradation and ligand mediated binding may have distinct advantage for the mediation of the reactions between the particles and a substrate, while further decreasing the likelihood of undesired reactions elsewhere in the system (*e.g.* organism). Lastly, the microfabricated particles will be made biodegradable through the use of biodegradable polymers. Intuitively, this provides increased safety to the individual (or organism) receiving therapy, or when used in other applications, provides for the decreased chance of injury to the given biological environment.

In summary, the microparticles and associated protocols in development are intended to remain adaptable to a variety of applications. However, the development of the microparticles thus far was in conjunction with a National Cancer Institute (NCI) project where the particles are intended to mimic natural killer cells. The particles in this case are intended to bind to the vascular endothelium of growing tumors and release a

lysing agent locally onto the cells, thereby arresting tumor growth through an anti-angiogenesis approach.

Project Goals

Intitial goals for this project included:

- Develop protocols for production of microfabricated particles of specific geometries (nonspherical)
- Produce both nondegradable particles in sufficient quantity to allow for evaluation of safety testing based on shape, size, and dose through i.v. injections
- Improve safety of particles by use of biodegradable polymers
- Achieve vectored-release of active agents carried by the particles
- Adapt particles to allow spatially specific attachment of chemical ligands/moieties
- Characterize protocol parameter effects on particle properties (morphology, etc.)
- Investigate effects of particle geometry *in vitro* and *in vivo* for potential applications

2.7.2 Methods

Choice Of Fabrication Process For Polymer Microparticles

The process presented to fabricate polymeric microparticles of specific geometry involves a soft lithography method know as micro transfer molding (MTM). This process was selected for the following key reasons:

- Applicable to a wide variety of polymer materials
- Layering on stamping substrate allows for release of particles
- Potential for scaling up to high-volume production
- The fabrication of 40- μm particles was previously demonstrated at OSU using the MTM process, so scaling the size down to 2, 5, and 10 μm was considered feasible.
- Necessary equipment available and operational at Ohio MicroMD

MTM Process Overview

The following steps summarize the MTM process developed at The Ohio State University to produce polymer microparticles using microfabrication.

Making the Mold

- 1) The desired features (*e.g.* 5 micron circles) are incorporated into a photolithography mask.
- 2) UV-sensitive polymer (photoresist) is then spun onto a silicon wafer. (The thickness of this spun layer controls final mold depth features).
- 3) Selective exposure of the photoresist to UV light via the mask causes chemical crosslinking only in those areas defined by the mask.

- 4) The photoresist on the wafer is then chemically developed leaving behind only the crosslinked polymer on the wafer.
- 5) The photoresist on the wafer is then coated using a silastic epoxy (PDMS--polydimethylsiloxane).
- 6) The epoxy hardens forming a mold from the photoresist features.
- 7) The wafer is then separated from the PDMS leaving an elastic mold with the negative of the desired features.

Stamping of Mold Features (Particles)

- 1) A polymer/solvent solution is applied to the PDMS mold.
- 2) The solvent is allowed to evaporate leaving behind a polymeric film on the mold.
- 3) An initial stamp (sacrificial stamp) with the coated mold is made at low pressure on a heated glass substrate. (This removes the polymer on the raised portions of the mold, while polymer within the mold features remains).
- 4) A second subsequent stamp (production stamp) is made at higher pressure with the same mold on a heated, coated* glass substrate to produce the desired polymer particles. (*This coating will serve as a sacrificial release layer).
- 5) The particles are then released by dissolving the water-soluble sacrificial layer via immersion of the substrate and attached particles in water.

As mentioned above Micro Transfer Molding (MTM) was used microfabricate polymer particles with specific geometries. This technique is based on established

methods of photolithography and soft lithography[Whitesides, 2001 #5][Becker, 2000 #6] The technique is analogous to the production of mold or a rubber stamp. A mold master with the desired geometrical features is produced with microfabrication techniques (photolithography and/or selective etching of a silicon wafer). The features defined in the photolithography mask control particle size and shape precisely. An elastic polydimethylsiloxane (PDMS) mold is produced from the mold master by soft lithography. Various polymer solutions (inks) are applied to the mold by spin-coating and allowed to dry under vacuum. Functionalizing materials (drugs, magnetic nanoparticles, etc.) can be included in the particles by direct incorporation in the polymer solution. (Fluorescein was used as a model in these studies). Microparticles are then stamped out of the molds on a glass substrate pre-coated with a specific polymer solution. The glass substrate serves as a handling substrate that allows for manipulation of the surface of the top and sides of laid-down particles. The polymer pre-coating then serves as a sacrificial release layer that allows the particles to be released upon immersion in water. These methods are shown in detail through figures 2.15-2.34.

2.7.3 Results

The processes and experimental set-up (figure 2.21) developed allowed for optimization of process parameters such as polymer/solvent concentration, stamping heat/pressure, etc. Particles were produced using both nondegradable and biodegradable polymers. Square and disk shapes were achieved for particles intended as injectable drug

carriers (2 micron, 5 micron, 10 micron). Larger more sophisticated geometries have been produced as well. Results were observed to be dependent on the wetting behavior of the polymer solution with the PDMS interface. 2.34. Production of polycaprolactone (PCL) particles, polylactic acid (PLA), and poly(DL)-lactic-co-glycolic acid (PLGA) was achieved using the MTM process. See figures 2.23- These poly(alpha ester) polymers were chosen since they are biocompatible and approved by the FDA for use in humans. By observing particles after incubation at 37 degrees centigrade in PBS for fixed periods of time (days-weeks), degradation rate of these particles was qualitatively observed to depend polymer crystallinity, molecular weight, co-polymer ratio of lactic acid to glycolic acid, and the inclusion of hydrophilic materials (PVA).

Use of the heat-presses with a polymer solution of PPMA (polypropylmethacrylate) in acetone has showed that a temperature near 90 C produced the best sacrificial films. As the polymer passes its glass transition temperature (T_g) it becomes more pliant. This pliancy, or “leathery” state, allowed better adhesion to the glass and better peeling from the mold. Changing the polymer employed (and the subsequent glass transition (T_g) and melting temperatures (T_m) required adjusting of the substrate temperature and stamping pressures. For the stamping out of particles, the “production stamp,” better results were achieved at temperatures above the T_g close to but not beyond T_m. Best sacrificial stamps were achieved by heating the sacrificial glass substrate to the T_g of the polymer of interest. Shown below are examples of “good” stamps and “bad” ones (figures 2.23-2.27). Note that these areas can both occur on the same glass substrate and often did. The effects were likely due to uneven heating and

uneven pressures. Optimization of process parameters in the future will likely require refined methods for pressure and heat control.

2.7.4 Key Considerations Identified for MTM Particles Process and Improvements

Made

Based on the empirical studies above several key elements of the process were identified. Unfortunately the project was terminated before efforts to study these key considerations could be realized. However, these elements and potential means of addressing them are worthy of discussion. These elements and potential for addressing them are discussed below.

Photolithography Masks and Negative and Positive Resists

Production of improved molds was attempted several ways. Early in the course of these studies there was some confusion in the proper selection of photoresist for the given 5 micron circle photolithography mask. After careful microscopic re-examination of the mask, the determination was made that a negative tone photoresist (SU-8, Microchem, Newton, MA) was appropriate. A mask initially provided contained 5-micron circles of light surrounded by dark; therefore, a resist that crosslinks areas exposed to UV was required. The earliest attempts utilized a positive tone resist (Shipley 1818) and thus had produced molds with inverted features. While seemingly obvious in retrospect, the confusion was compounded by the fact that PDMS molds and SU-8 on silicon could initially were not easily imaged directly using standard scanning electron microscopy

(SEM) techniques available at Ohio MicroMD. Both materials in question rapidly develop a surface charge as a result of the bombardment of the electrons from the electron beam. When such a charge develops the resulting image is a “white out” such that features cannot be distinguished or no image is obtained. This imaging problem was solved by refinement in sample preparation, i.e. sputter coating of the material with a thin layer of metal or vapor phase deposition of metal on the surface. After ascertaining the need for a negative photoresist with the given mask, several molds were fabricated using SU-8 (25) photoresist. In this case, the designation “(25)” refers to the optimal photoresist thickness for use in photolithography, according to supplier guidelines. For any given microdevice, the normal photolithography process for the photoresist is: spincoat, softbake, expose, postexpose bake, and develop. This process must be optimized individually for the device in question (in our case a 5-micron particle mold master) with guidelines from the manufacturer. Determining the proper exposure time and intensity of UV light for the photoresist was a key aspect of this process. Under or overexposure of the photoresist leads to undesirable physical features that manifest themselves as defects in the mold. Previous process parameters with the 40-micron particles did not translate exactly and had to be re-examined. The lamp was changed in the aligner, which explained some variation from previous results (in addition to the necessary deviation for a difference in attributes/geometry). Once the photolithography process was considered optimized, several new molds were produced from the SU-8 masters.

Nonstandard Heat and Pressure During Stamping

Once the PDMS molds were produced they were then used for attempts at stamping out polymeric microparticles. A two-stamp process, as described above, had demonstrated previous success with 40-micron particles. Heating of the glass stamping substrate had been accomplished initially with a Bunsen burner and then, in later trials, with a convective oven. Heating was determined to assist in adhesion of the polymer to the glass substrate.

The elastic properties of the PDMS mold under pressure allow a two-step stamping process, where the first stamp serves as a sacrificial stamp and the second stamp produces the desired features (particles). Pressure previously was applied to the molds by subjective use of the hands and thumbs. As such the process was known to be both temperature dependent (the glass substrate) and pressure dependent, but the optimal temperature and pressure for stamping was unknown. To address these issues, two heat-presses were fabricated to allow for optimization of process temperatures and pressures. One heat-press can be used to determine optimal pressure for the sacrificial stamp, and the other for the production stamp. This device is shown below (.figure 2.22). The key features are the pressure indicator and temperature controlled stage for the glass substrate.

Initial experience with the devices led to improvements in their design. First, the temperature controllers' markings for temperature were not accurate. This was determined using a handheld thermocouple. As such, there was no indicator of the actual surface temperature of the heated stages (and thus the glass slide). The observation was also made that the temperature of the stage may be fluctuating. To address this issue, a K

type digital thermometer with dual thermocouple inputs was bonded to the surface. The thermocouple inputs were attached to the heated stages (via thermal putty) to more closely monitor the stamping substrate temperature. This modification allowed more thorough investigation of the temperature-dependent behavior of the polymer films both in the sacrificial stamp and the production stamp. When modified by attachment of surface thermocouples, the heat-presses allowed more accurate and precise trials. The device was further modified with a locking feature to allow extended applications of known pressure. This feature allowed empirical determination that substrate contact time does not appear to be a significant parameter in the stamping process. Experiments conducted where the temperature was deliberately varied below, near, and above the glass transition (T_g) and melting (T_m) temperatures of the polymers in the solutions showed that proximity to polymer T_g and T_m influences separation from the mold/adhesion to the substrate.

Interfacial Characteristics/Surface Chemistry

Careful consideration of the interfacial chemical characteristics of the polymer solution(s) is needed. The overall particle process involves the following three interfaces:

- 1) between the polymer solution and the PDMS mold
- 2) between the dried polymer solution (on PDMS mold) and the glass substrate
(low pressure sacrificial stamp)

- 3) between the coated (sacrificial layer) glass substrate with the polymer mold (high pressure production stamp)

These processes are largely functions of the solvent characteristics of the solution and the solids (polymer) content. Employing various concentrations of PPMA that worked previously with 40-micron particles did not work well with smaller particles (5, 10 microns).

Geometrical Considerations in the MTM process

Difficulties were encountered using the MTM process for the 5-micron circles, when compared to previous success (40-micron squares), are likely attributable to the change in geometry of the molds combined with the interfacial physicochemical characteristics of the polymer solution being employed. Previous success had been achieved with 40-micron squares using an SU-8 (25) photoresist. This epoxy has optimal characteristics at 25-micron film thickness, according to the manufacturer (Microchem, Newton, MA). The photoresist can be spun down to around 20 microns. These numbers indicated an aspect ratio of less than 2 and a feature area to feature depth ratio of nearly 80. Using the same SU-8 (25) photoresist for a 5-micron diameter circle mask implies an aspect ratio of 5, and an area to depth ratio of less than 1. The geometrical attributes of the mold certainly affect mold filling, especially when considering the physicochemical properties of the solvent/polymer solution. The wetting properties of the polymer solution affect how the mold features are coated/filled. It remains unclear as to how the polymer solution penetrates into the features of the mold. The features are not

necessarily “filled” with polymer solution. This concept was demonstrated when a solution of acetone and dye were applied to PDMS molds. The mold “holes” did not appear to contain any dye by light microscopy. This supports the notion that the polymer solution may only wet the surface of any features and was too deep to be seen (or that the dyed solution failed entirely to penetrate the features). This wetting phenomenon may explain why such thin particles are produced for the 40-micron molds. However, at some critical aspect ratio the intermolecular adhesive forces of the polymer/solvent solution coupled with that solution’s PDMS-wetting behavior might lead to filling of the mold features by capillary action: thus, a “dip pen” technique (where the mold is dipped in solution) might be feasible. Such capillary filling would depend on the wetting properties of the polymer/solvent solution on PDMS, the intermolecular adhesion of the solution itself, and the mold geometry (aspect ratio). The physical behavior of the fluid (polymer solution) in the mold is influenced by solvent choice (polarity, volatility, etc.) and solids content (concentration, molecular weight, hydrophilic/hydrophobic interactions, viscosity, etc.).

These geometrical considerations likely result in repercussions for

- Manufacture of the mold
- Filling/coating of the mold
- Mechanically stamping out the final products (particles).

Use of a high aspect ratio mold complicates the mechanical stamping out of the particles, making this aspect of the stamping protocol nontrivial. This notion seems

intuitive given that we rely on the elastic deformation of the coated PDMS for a two-stamp process. Decreasing the aspect ratio of the molds (and mold masters) facilitated stamping out of the particles in the second high-pressure stamp. Smaller deformations of the PDMS are required, reducing the likelihood of particle deformation. Adjustment of this geometrical parameter was accomplished by using a thinner initial photoresist layer in the photolithography stages of PDMS mold production. This appeared to improve particle production presumably by enhanced filling/coating of the molds at these lower aspect ratios.

Mold Manufacture from Etched Silicon Wafers

The problem of aspect ratio for mold production was addressed by development of a method of polymer production using etched silicon wafer. An etched silicon wafer with 10-micron squares of <2-micron thickness to served as a mold master. This wafer was then used to attempt to fabricate a PDMS mold. Unfortunately, early attempts were unsuccessful. Strong adhesion between the PDMS and etched silicon prevented separation of the two surfaces. The wafer could not be separated from the silicon and shattered while remaining imbedded in the PDMS mold. This problem was circumvented using a contraption to deposit a thin layer of silanes on the etched wafer. The layer allowed separation of PDMS molds from the silicon master and some success was achieved using these molds to produce 10 micron particles.

Mold Filling/Coating

Previously, PDMS molds were filled/coated using a swabbing technique of polymer solution on an inverted mold. This method contributed to the observed result that particles were only being produced in select areas, or the mixed results for the same stamping. Attempts to improve mold loading were achieved by placing the solvent/polymer solution onto the molds in known volumes via pipette to achieve complete coverage of the mold surface. These attempts produced sacrificial films that appeared to be thicker centrally (where the pipette drops had been placed) and did not improve particle yields. Another strategy to improve uniformity of the coating layer was developed. The PDMS molds were coated on the spinner by drop-wise addition of polymer solution with a ramped spin speed. The process did not show improvement for particle production but appeared to produce better sacrificial films (more even, enhanced removal). At higher spin speeds, though, the sacrificial polymer films occasionally lacked the holes characteristic of other efforts. The hypothesis is that with such a high aspect ratio the polymer film might be bridging the 5-micron gaps rather than entering them. Swabbing, on the other hand, induces some pressure on the polymer solution to enter the mold features. A combination of swabbing and subsequent spinning to level the top layer of polymer solution showed some benefit and may merit further investigation.

Resusing and Cleaning PDMS Molds

Another plausible explanation for the varying results was identified. Trials often reused the same PDMS molds; thus, molds may not have been completely empty from

previous trials. Stamps had been cleaned between trials (after stamping) by use of adhesive tape. Incomplete cleaning could also have created imbedded particles and mixed results. Cleaning PDMS stamps by immersion in acetone followed by drying with blasts of compressed nitrogen was found to be more effective. The best method for cleaning the stamps between use was found to be by use of a sonicator as shown in figure 2.21.

Behavior of Polymer Solutions

To consider the effect of the physicochemical characteristics of the polymer solution, different solvents were investigated for their effect on particle production. PDMS has a hydrophobic surface and solvents with varying hydrophilic/phobic composition were investigated. Because the particles being investigate were had intended use in humans, solvents with increased biocompatibility had to be identified. The MTM process was empirically adjusted for the solvents THF and DMSO

In order to advance the understanding and prediction of the underlying physics/chemistry wetting behavior, contact angle measurements and wetting characteristics of the aforementioned interfaces (polymer on PDMS; polymer on glass; polymer on glass with sacrificial layer) might provide some insight. A tensiometer and/or a goniometer are devices for examining surface interactions between liquids and solids . These devices allow estimation of the combined wetting characteristics and intermolecular adhesion of a solution on a substrate. Rapid, systematic examination of the solvent properties and polymer concentration could be conducted using this equipment. Studies of polymers of the same composition and concentration varying only in tacticity,

molecular weight, or modified side chains might be conducted to advance the understanding and prediction of MTM results.

Particle Release/Sacrificial Layer Considerations

For 40-micron squares, a thin layer of water-soluble polymer (PVA) has been demonstrated in principle as an effective sacrificial layer for particle release. Initial experiences stamping PPMA 5-micron circles onto the PVA are consistent with the possibility that PVA can be used as well in this process. The sacrificial layer's effect on interfacial phenomena and surface properties may have to be considered, especially later when using biodegradable polymers and attaching a targeting ligand. The optimal concentration of PVA though has not yet been determined, nor has a quantitative investigation of wetting/adhesion of polymer solutions on such sacrificial layers. Goniometer and tensiometer experiments of polymer solutions on proposed sacrificial layers will be considered. It may be proven to be beneficial to take advantage of a sacrificial layer as an adhesion/extraction promoter to “pull” particles out of the molds. On the other hand, a sacrificial layer may be proven to be unnecessary if the particles can be released by sonication without damage.

2.7.5 Project Goals Not Accomplished and How They Might be Addressed

Achieving one-sided degradation

A stated goal was to produce a particle that degrades from one side achieving vectored release of an agent. Before particles are released from the sacrificial layer they

can be modified on all sides except one. The MTM process in theory could be modified such that the particles are encased in a diffusion barrier on all sides except the one from which release is desired. This may be accomplished several ways. Polymer of lower degradation rate (less susceptibility to hydrolysis) should encase a faster degrading core. The diffusion barrier could be PCL encasing a PGA core (or PLA, PLGA, etc.) The core degradation kinetics would control release of the active agent. Faster degradation would be achieved with lower molecular weight PGA or more amorphous PLGA combinations. Some variant of PLGA (50:50) could be the core while a more crystalline version (PLGA 90:10) could be the outer shell (diffusion barrier). Deposition of the outer core would commence before release of the particles from the glass substrate. Sputtering or evaporation could be used to accomplish deposition of one polymer onto another (PCL onto PLGA). Alternatively, this might be accomplished by applying multiple polymeric layers on the PDMS mold. The diffusion barrier(s) would be applied first, followed by the core polymer/agent solution. Some adjusting of the MTM protocol might be required in order to account for the multiple layers. Still another promising alternative might be to use some sort of radiation (heat, light, UV, X-ray, etc.) to cross-link the outer layer of the polymer particles. The cross-linked layer would then serve as the diffusion barrier. Other processing modifications could allow adjustment of particle degradation such as increasing the porosity of the particles/particle core. Increased porosity can be achieved by rapid evacuation of solvent either through heat or through quenching (as discussed in section 2.6). This increase in porosity will also lead to faster degradation. In summary the aim is to create a selective diffusion barrier for water and thus hydrolysis one of several means including:

- Sputter coating
- VPD of polymeric film on particles prior to release,
- Outer layer cross-linking by irradiation, UV, or visible light
- Layering

For verification of vectored release, fluorescence imaging could be used (or another appropriate assay). For example, PCL might be doped with green fluorophore and the PLGA core with red fluorophore. Through fluorescence microscopy, particles could then be inspected for layering and observed for release of fluorescence, or red/green background fluorescence changes could be monitored over time for a solution of particles.

Chemoselective Ligand Attachment

Attachment of a chemoselective ligand for site-specific targeting of particles would incorporate the following:

- Ligand selection
- Cross-linking (CL) agent selection
- Use premodified polymers in production process to be compatible with CL
- Selective modification of particle surface by microfabrication methods (for CL)

The stated goal is to make these particles adaptable for use as a general drug delivery platform, with the ligand choice being dictated by the intended purpose. As such it is expected that the user would carry out the ligand conjugation. Ideally, the particles

should be universally adaptable to almost any ligand. Numerous protocols are well described for protein conjugation chemistry. For the NCI artificial NK project, the ligand of choice is EGF, VEGF, or FGF-2. Positional control of chemical conjugation for these and other proteins can be achieved by using premodified polymers in the MTM process. A significant advantage of *a priori* modification is that conjugation reactions will be able to be carried out in solution. Amine group and thiol group modified polymers of PLGA are commercially available and could be tested for this purpose. Also of interest is that this method of using premodified polymers enables the possibility of further modifying the particles with immune evasion molecules such as polyethylene glycol (PEG). Methods of verifying ligand attachment would need to be considered.

2.7.6 Potential Experiments for Evaluating Particle BioInteractions

In Vitro

The experiments described below could be conducted as the MTM particle protocol(s) become refined. Ideally, these experiments will be carried out with both circular and square particles--each in the 2, 5, and 10-micron sizes. Spherical particles can be included in these experiments for “baseline” comparison as well.

Ligand-Mediated Binding/Cell Killing

Demonstration of site-specific ligand attachment and subsequent *in vitro* ligand mediated binding might be accomplished in several ways. One way would be to use the a Laser Scanning Cytometer (LSC). Cells could be treated with an appropriate fluorescent marker and the microfabricated particles could be dyed with a different color of

fluorescence by direct incorporation (figure 2.27). The particles would then be added to the cells in culture medium and observed for binding interaction, and eventual cellular effect (*i.e.* cell death). This experimental setup might be generalized for any combination of cells, ligand choice, particle geometry, or particle size. Use of the LSC is compelling in that four different fluorescent dyes can be monitored simultaneously. Indeed, it would be possible to incorporate particles of various size and/or geometry into a protocol that tests each particle size/geometry independently and then again in combination, for cellular interactions/binding. The results of these tests could then be used to assess what effect particle geometry and size, if any, have on cellular processes. Appropriate fluorescent staining of the cells in subsequent trials could elucidate subcellular processes occurring.

Biocompatibility/Biodegradation Testing

Elution Tests

In order to test for biocompatibility of the particles in question, simple *in vitro* testing could be conducted using the particles. This might include sequential elution testing of the particles where a given number of particles are placed in phosphate-buffered-saline (PBS) at 37C for some amount of time to allow for diffusion/degradation of particle constituents (such as residual solvent). Fixed amounts of the solution could then be added to cultured cells and observed for perturbations; cells from the same batch in plain PBS would serve as controls. These tests would be especially informative for particles made with cytotoxic solvents. Particles for this test would likely be plain (*i.e.* void of payload/ligand), but could be modified particles.

The elution solution should be monitored for changes in pH and biodegradation of particles (where appropriate), and could be assayed for release of particle products in later tests. In such later tests, biodegradable particles should be watched for changes in morphology and overall degradation characteristics. This could be accomplished via the LSC, or more generally with light microscopy. Subsequent digital image acquisitions would allow morphological assessment of the particles. Using an appropriate image analysis package, particles could be assessed for changes in area, perimeter, and count. These values could then be used to determine geometrical changes such as circularity and rectangularity for round and square particles, respectively.

Confluence Tests

Separate biocompatible tests could be conducted where a cell line (*i.e.* mouse aortic endothelial cells, MAECs) is grown to confluence in a petri dish. Particles (modified and/or unmodified) of various size and geometry could then be placed directly on the cells. The confluent layer will be observed over time for cellular loss or perturbations in the region of the particles. Digital image analysis will be conducted (on cells and particles), as describe above, to determine the effect(s) of particle composition, size, geometry, and degradation on the cells and the range (*i.e.* distance) of these effects.

A Geometric Phagocytosis Assay

Much work has been described and is under way that relates microsurface features (topology) on cellular interactions. However, there is little information on how geometrical features affect subcellular processes. Along these lines, there is no literature thus far that describes the effect of changes in microstructural geometry on the

phagocytosis of microparticles. Because the microfabricated particles are being advanced as a general platform for intravenous (i.v.) injection, a phagocytosis assay could be developed using the LSC. The reason for such an assay is two-fold: 1) avoidance of phagocytic clearance of the particles by the reticular endothelial system (RES), 2) deliberate targeting of the RES. The former refers to the tendency of injectable particles to be cleared from the bloodstream before reaching their site of therapeutic action. In most cases, this undesirable consequence limits the efficacy of microencapsulation therapeutic modalities. Strategies have been developed to limit RES clearance of particles, such as PEGylating particles (Stealth™ Liposomes, Sequus). On the other hand, this natural tendency of particles to be taken up by immune system constituents might be exploited for deliberate targeting of immune system disorders or adjuvants/vaccines. Therefore, determining which how particle geometry alone influences the RES clearance is essential to maximize therapeutic goals, especially for a general particulate drug delivery system.

Initially, unmodified polymeric particles could be evaluated using the Laser Scanning Cytometer. Macrophages are known to phagocytotize particles up to 10 microns. Therefore, the fabrication of particles 2, 5, and 10 microns of various geometries (squares and circles) would be ideal for such a phagocytosis assay. Initial studies might involve PPMA, a nondegradable polymer. Later biodegradable polymers (PLA, PLGA, PCL) could be considered for comparison of the effect of chemical composition. Further studies where the particles have been chemically modified (*e.g.* PEGylated) for RES evasion would then possible.

The experimental design would rely on selection of an appropriate phagocytic cell line. Such a cell line might be ordered from commercially available suppliers, or produced from either human or animal blood products. Typically when whole blood is collected, as in donation, only the red blood cells are desired. Centrifuging the blood at specific speeds and tilts produces what is known as a “buffy coat”. This buffy coat contains the white blood cells, or mononuclear cells (neutrophils, monocytes, NK cells, lymphocytes). Generally, this buffy coat is discarded. These cells can be harvested and/or further separated to obtain a phagocytic cell line. Phagocytosis by these cells is particularly interesting because they have the ability to act as antigen presenting cells (APCs). APCs are the cells responsible for vaccine efficacy. If an appropriate antigen is incorporated into the particles and the phagocytosis process of the particles might lead to increased vaccine efficacy. Even further targeting to subcellular components to enhance biological effects might be possible. For example, incorporation of liposomes targeted to the Golgi apparatus might enhance cellular processing of the antigens for presentation to other immune cells, thereby increasing the possibility of a therapeutic vaccine. If this antigen is one that is unique to cancer (tumor associated antigen, TAA), then it may be possible to enhance current cancer vaccines. In theory, all diseases where unique antigens are identifiable might benefit from the geometrical adjuvant effect of microfabricated particles.

The LSC experiments could be carried out much as described above, taking advantage of the positional discrimination and multicolor capabilities of the LSC. Particles of the same geometry (circular) but differing in the 3 sizes (2, 5, 10 microns) could be stained with 3 different fluorescent markers, while cells would be stained a

fourth color. The rate of phagocytosis for different sizes at the same geometry could then be compared. The same experiment would be repeated for 3 sizes of another geometry (square) and compared to the circular data. Both could be compared against another experiment using spherical particles, or even particles with much higher surface energies (e.g. “spiny” particles). Experiments where particle size is kept constant (comparable volume) but different geometries are employed would indicate a “geometrical phagocytic preference”. Further experiments where all sizes and shapes are incorporated would address how size and geometry are interrelated in RES clearance. The information gathered from these experiments could then be used to design more effective vaccines (deliberate passive targeting) or improve efficacy of the drug delivery systems by RES evasion.

2.7.7 Conclusions

Summary of Accomplishments and Problems Solved

- Enhanced protocols for production of microfabricated particles of specific geometries and sizes down to 2 microns including circular and square particles
- Created standardized laboratory set-up for continued optimization of MTM process parameters
- Significantly increased MTM protocol production yields
- Improved safety of particles by use of biocompatible solvents (including investigations of solubility and observations of wetting behaviors)

- Investigated optimal polymer concentrations for production of particles for both nonbiodegradable (PMMA) and degradable particles (PCL, PLGA)
- Implemented method of producing PDMS molds from etched silicon wafers using silane vapor phase deposition

As discussed above, targeted controlled drug delivery for the treatment of disease continues an attractive area of research. The selective delivery of agents to specific tissues without concomitant effects to other tissues continues to be a lofty goal. Perhaps most notable in this regard is the selective killing of cancer cells without subsequent damage to healthy tissues (toxicity). For some time now, microencapsulation of agents has been advanced to try to meet this goal of selective delivery. Microencapsulating research thus far has been limited to the use of self-assembled particulates that result in particles of fixed spherical geometries. Microfabrication of polymeric particles offers an attractive alternative for microencapsulating particles research. This work advances a method to produce microencapsulating particles of customizable geometry, with potential both as a general delivery platform and in specified applications (artificial NK cells, vaccines, etc.). The work reported demonstrates that production of particles of a specific geometry by this method is indeed feasible; yet, there are significant obstacles to be overcome. Problems encountered in fabrication, both thus far and foreseen, and potential means of addressing them are discussed. Plans to obtain vectored release and biodegradation of particles will ameliorate safety concerns for use of these particles in biological environments, as well as amplify the potential for further applications. Also outlined are further experiments to address and maximize the utility of microfabricated

microparticles for applications involving intravenous injection. The advantages offered by microfabrication technology such as precise control of geometry and spatial chemistry, industrial scalability, and adaptability to a wide variety of polymers and therapeutic agents, are vast. This research advances a universal microfabricated particle platform that includes: 1) control of geometric shape, 2) the ability to attach targeting moieties in a spatially specific manner, 3) vectored release of agents, 4) eventual complete biodegradation of the particle. The planned experiments outlined could serve as initial evaluation and validation for such particles. When successfully developed, these particles could have far-reaching medical implications via targeted controlled drug delivery as well as distinctive applications for self-assembly of various other chemical reactions.

The need for efficient and controlled delivery of drugs has created strong demand for novel drug delivery systems. Particulate drug delivery systems, such as polymer microparticles and liposomes, are under intense study and some products have reached market. However, due to the surface driven manufacturing process of these systems, the shape of the particulates produced is mostly limited to sphere; the size distribution of the particulates is usually wide; and the structural complexity of the particulates is relatively low. For certain envisioned features of novel drug delivery vehicles, such as targeting and highly controlled release, these may be limiting factors. Microfabrication, traditionally used to produce integrated circuits, is the production of micrometer and nanometer-scale structures by the selective placement and/or removal of materials through deposition, etching, photolithography, and recently developed soft lithography. Compared to conventional polymer microparticle fabrication methods,

microfabrication offers much more control of the particle geometries, contents and structures. Attempts are being made as discussed to produce silicon-based micro-devices for oral and intravenous drug delivery with microfabrication technology. This strategy, however, suffers from the obvious problem that the silicon is not biodegradable.

To take advantage of modern microfabrication technology and the huge pool of polymeric materials used in biomedical and pharmaceutical industry, simple methods based on MicroTransfer Molding (MTM), were used to fabricate polymer microparticles with a variety of polymers including biodegradable polymers. Microfabrication of microparticles by MTM is a promising method for producing particles in highly controlled sizes and geometries for numerous biomedical applications. Degradation rate, size, and shape and spatial functionality of microparticles can be manipulated in conjunction with this method.

The ability to control the precise shape and size of microparticles has distinct advantage. The disc-like shape of the microparticles renders them different aerodynamic and fluidic dynamic properties than conventional spherical microparticles, which may be beneficial to certain delivery strategies, such as pulmonary and intravenous routes. The high surface area/volume ratio of the microparticles may also be desired for targeting applications. The fabrication techniques are simple and have potential for scaled-up manufacturing. Research to further advance this technology will undoubtedly yield exciting results.

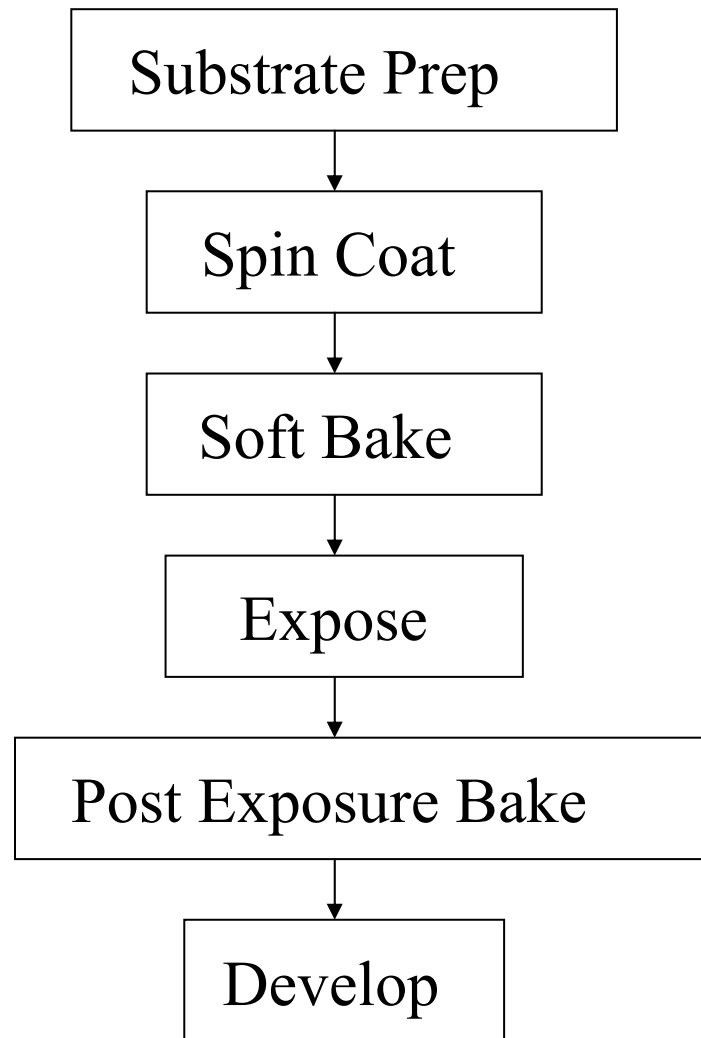
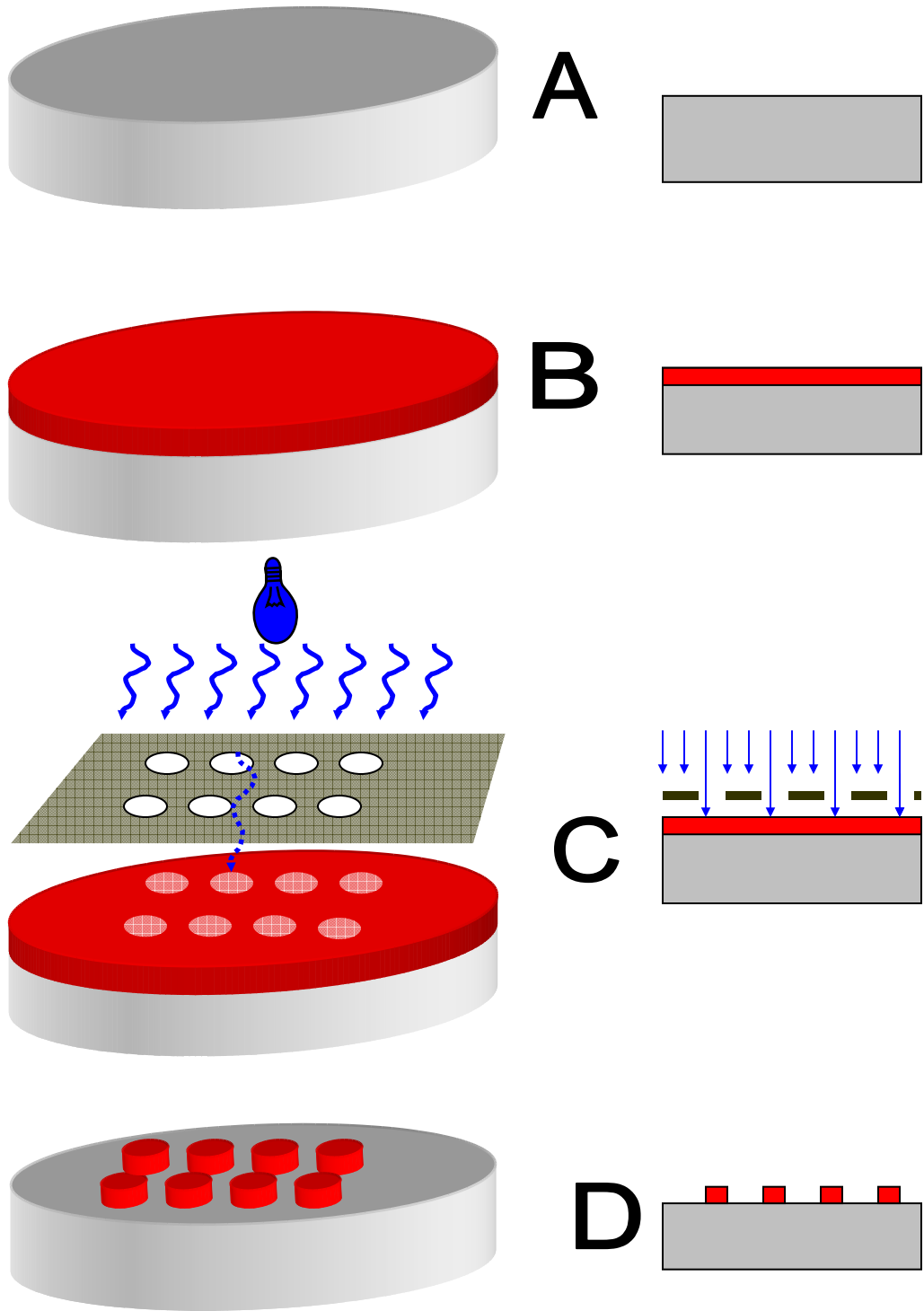


Figure 2.15 : Steps in the photolithography process for production of a mold master.

Figure 2.16 (left) and 2.17 (right): Schematic of photolithography process in 3-D (figure 2.16) and 2-D (figure 2.17). (A) Silicon wafer is prepped by cleansing. (B) A photosensitive polymer (SU-8)—the positive photoresist—is applied using a spin coater. Charts from the supplier dictate what spin coater speed to use for the desired photoresist thickness. The thickness of the photoresist determines the depth of the features that will be produced in the mold (pillar height in this case). (C) A photolithography mask (shown in grey) is employed to selectively expose the photoresist to light. The unshadowed features of the mask will be transferred to the photoresist (circles). The coated wafer and the photolithography mask are brought into line and an aligner (TYPE) exposes the “unmasked” region with a 405 nanometer wavelength lamp (TYPE). This exposure induces selective cross-linking of the photoresist in only the desired regions, predefined in the mask. A post-exposure bake in the oven finalizes the cross-linking of the selected regions, after which the nonexposed regions are dissolved using a chemical developer specific for the photoresist.



Figures 2.17 and 2.18: Schematic of photolithography process in 3-D (2.17) and 2-D (2.18).

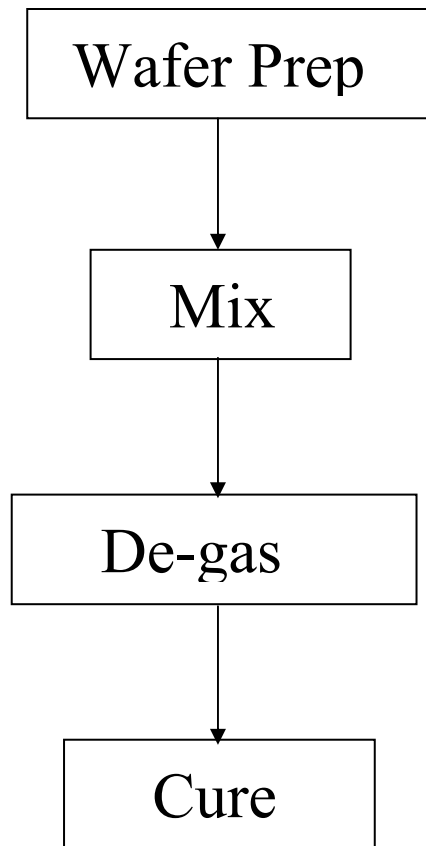


Figure 2.18: Steps for production of PDMS mold. The wafer (mold master) with the desired features is prepped; the PDMS epoxy is mixed and applied over the wafer; the mixture is degassed under vacuum and allowed to cure either in an oven or overnight at room temperature.

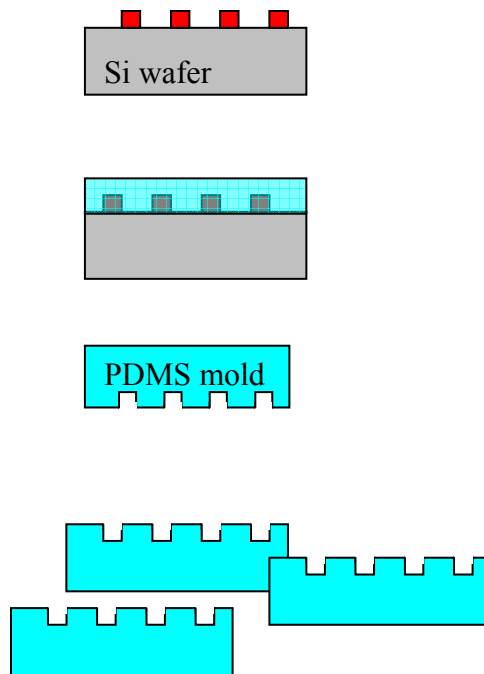


Figure 2.19: Mold (stamp) production using soft lithography (schematic). The photoresist on the wafer is then coated using a silastic epoxy (PDMS--polydimethylsiloxane). The epoxy and curing agent are mixed, poured onto the wafer, and placed under vacuum to remove trapped gas (from stirring epoxy) and to enhance penetration of the PDMS into the photoresist features. The epoxy hardens forming a mold from the photoresist features. The wafer is then separated from the PDMS leaving an elastic mold with the negative of the desired features. The same wafer (master) can be used to produce many molds.

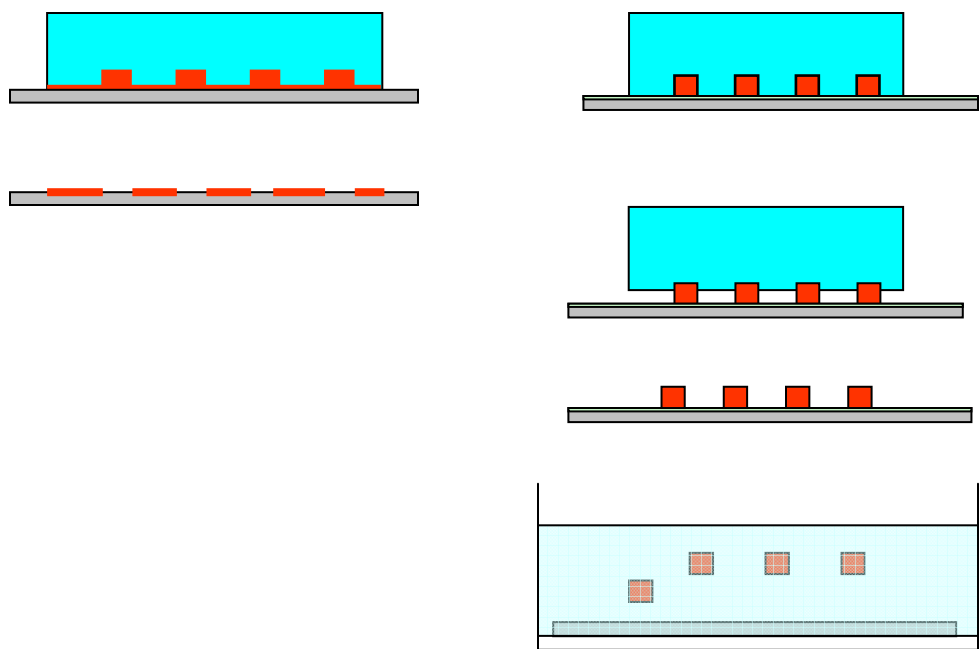


Figure 2.20: Schematic of the two-stamp MTM process. An initial sacrificial stamp (left) on heated glass removes the polymer from the raised portions of the mold. A second stamp (production stamp) on the pre-coated, heated glass substrate removes the particles from the mold. Immersion in water dissolves the water-soluble pre-coating to release the particles.

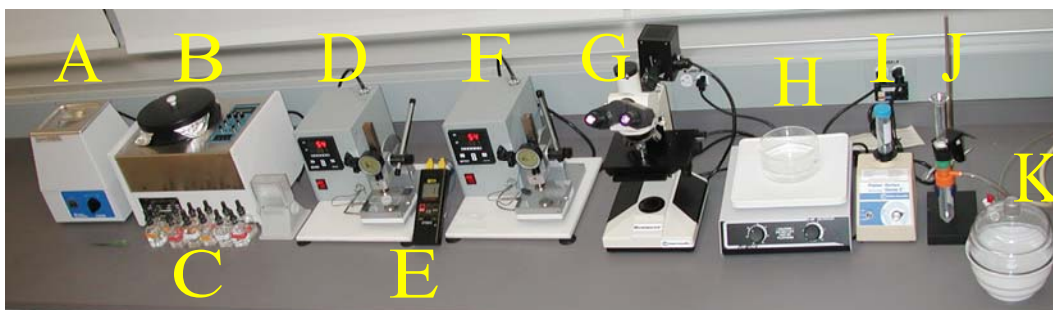


Figure 2.21: Experimental set-up for optimizing the Micro Transfer Molding (MTM) process. This set-up was designed for the investigation of specific process parameters and scaled-up microfabrication of polymer microparticles. (From left to right) (A) A sonicator was used to clean molds before and after use. The spin coater (B) was used to apply varying polymer solutions (C) evenly and at consistent thicknesses. The two heat-presses (D and F) were equipped with digital microprocessor-controlled heating stages for heating of stamping substrates. The anvils were 1" in diameter but the presses were designed to accommodate a switch to a full wafer size of 3" (note: 1" section of 10 μm squares contains over 3 million particles). Manual force is used to apply pressure for both presses, and the analog gauges report the force. The presses were designed with a locking feature to allow sustained pressures. A 2-channel thermocouple (E) is attached to the surface of both heated stages to ensure accurate reporting of surface (stamping) temperatures. Press D was specifically designed for the temperatures and lighter pressures required for a sacrificial stamp; press E was employed for the "production" stamp. The light microscope (F) allowed inspection of trials for quality control. Particles were then released in the water bath (H), or in directly in centrifuge tubes (I). Particles could be left in suspension or collected by filtration (J) and dried under vacuum (K).

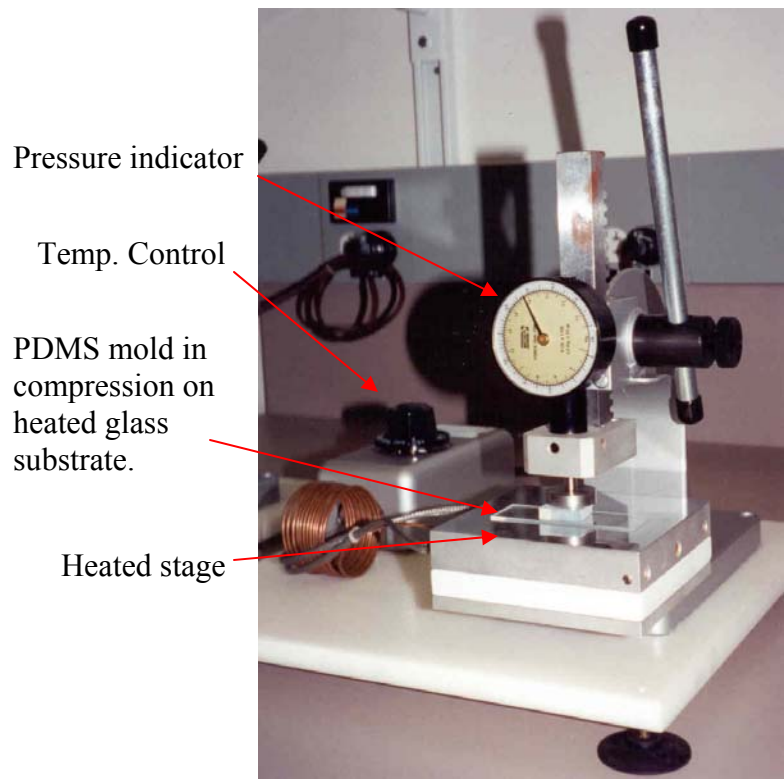


Figure 2.22: Detail of heat-press. The heat-presses were designed to allow precise control over both pressure and temperature in order to optimize the MTM process.

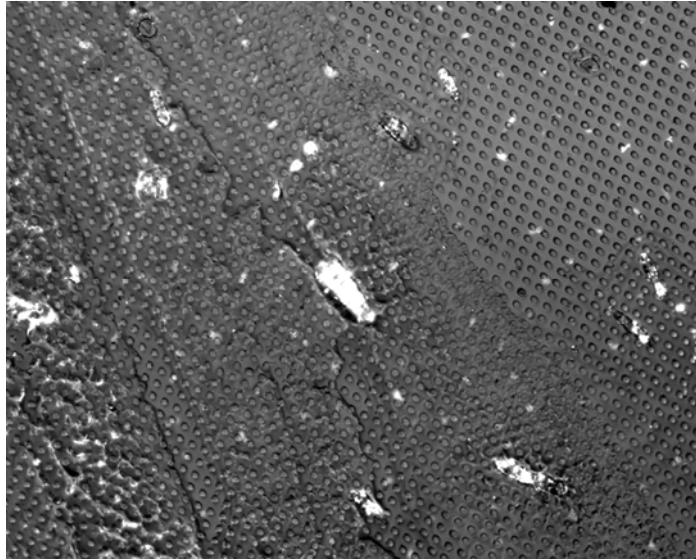


Figure 2.23. Sacrificial stamp from early MTM efforts (PPMA, 5-micron circles). This light micrograph (50x magnification) show poor separation of the polymer lattice and particles; varied, uneven thickness of polymer film; and melting of some features (left) due to uneven heating.

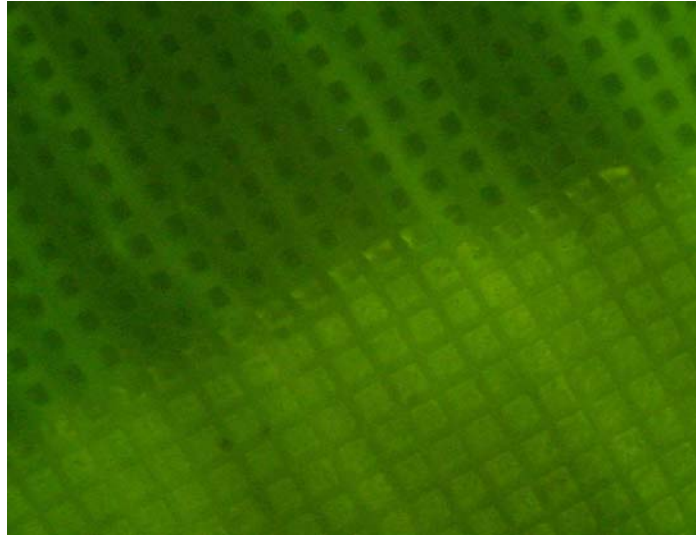


Figure 2.24: Fluorescence micrograph showing embedded PLGA particles (40x magnification). Poor separation of these 10 micron fluorescein-loaded particles resulted from improper heating of the glass substrate during the sacrificial stamp.

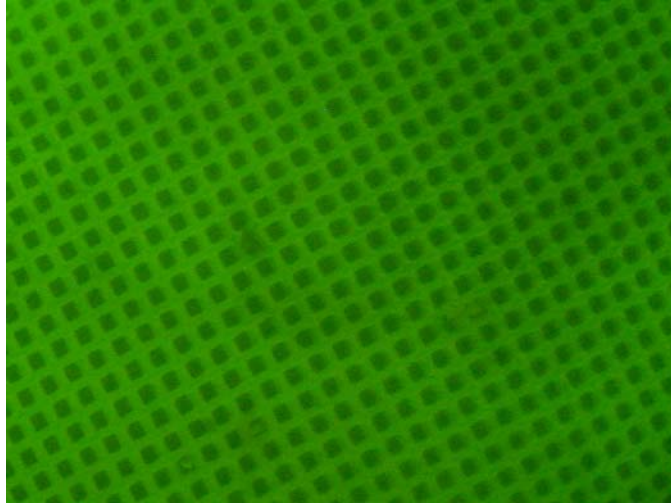


Figure 2.25: Fluorescence micrograph of properly transferred sacrificial stamp. (25x magnification, PCL).

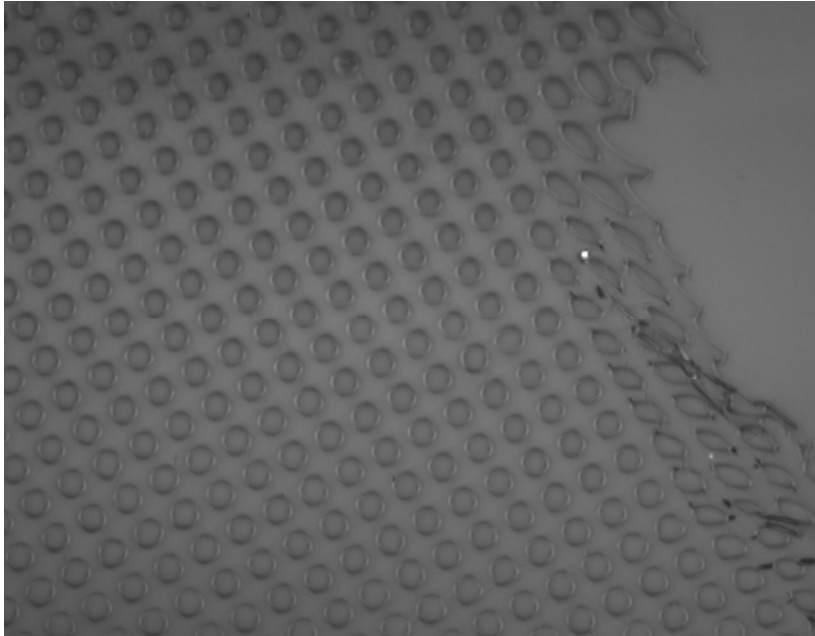


Figure 2.26 Light micrograph of sacrificial stamp. Polymer lattice (PPMA) resulting from first stamp in the two-stamp MTM process for 5 μm circles. (50x magnification,)

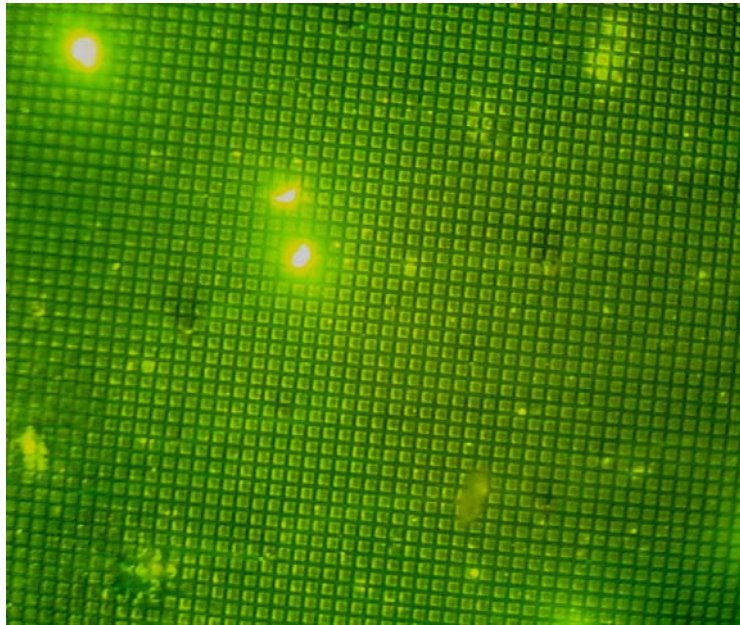


Figure 2.27: Fluorescence micrograph of large area of 10 micron square PCL particles before release (10x magnification). Fluorescein was included in particles to demonstrate particle loading with a model drug.

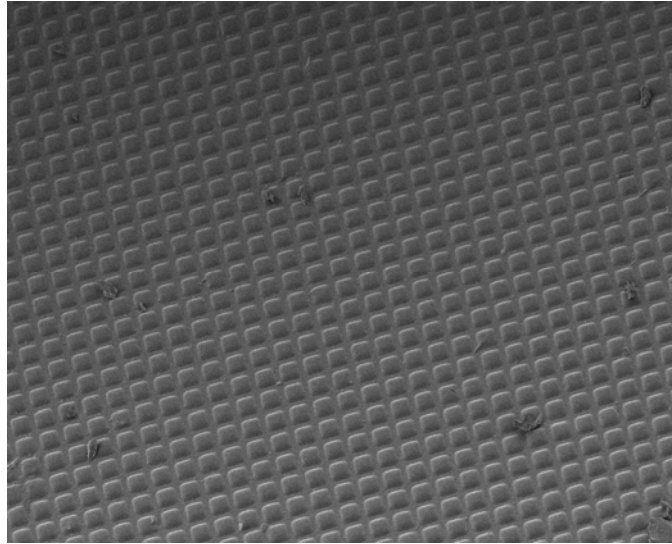


Figure 2.28: Scanning electron micrograph of 10 micron PCL squares on sacrificial layer. (35 x magnification)

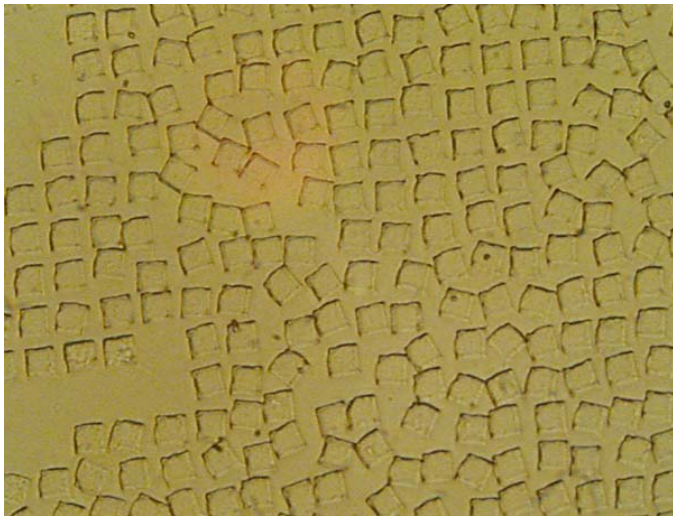
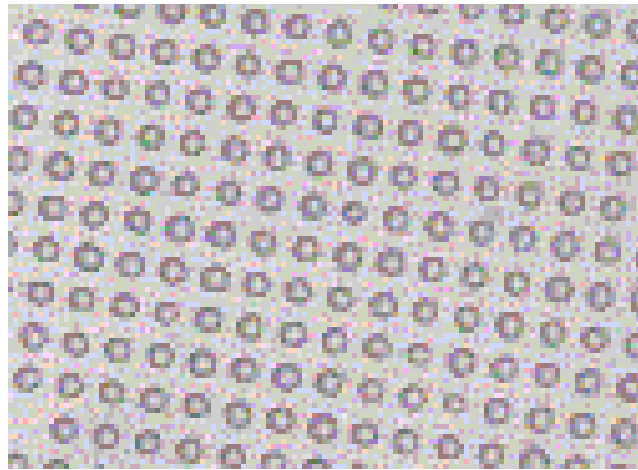
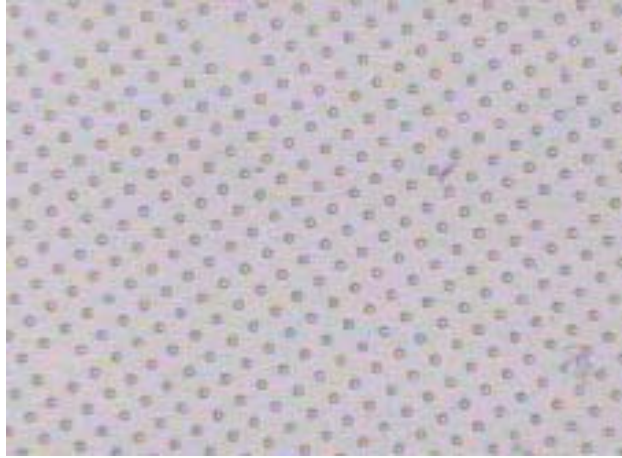


Figure 2.29 and 2.30: Release of microparticles by immersion in water. Above, 20x magnification) 5 micron PCL circles. (Below, 40x magnification) 10 micron PLGA squares.



Figures 2.31 and 2.32: Light micrographs of circular particles. (Top) 2 μm PLGA circles, 50x magnification; (Bottom) 5 μm PCL circles, stamped on sacrificial layers, 50x magnification.

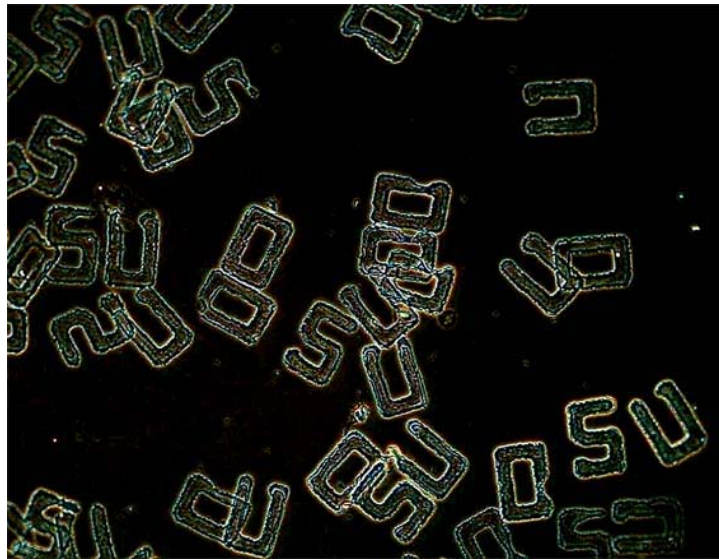


Figure 2.33: OSU particles produced by MTM process in our lab. This image demonstrates the complex geometries possible using the MTM microfabrication technique (Image courtesy of J. Guan).

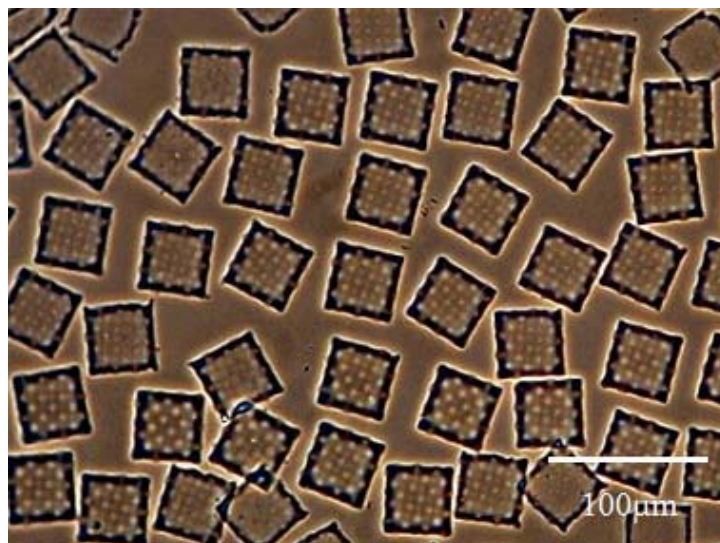


Figure 2.34: Particles with model functional groups attached. These particles were produced by first stamping out 40 micron square PPMA particles on the sacrificial layer. While these particles were still on the glass handling substrate a 5 micron circular stamp was then used to deposit a layer on top of them. This method demonstrates how particles with functional groups (ligands, etc.) might be produced. (Image courtesy of J. Guan).

REFERENCES

1. Nanomedicine: grounds for optimism, and a call for papers. *Lancet* 2003;362(9385):673.
2. Andersson H, van den Berg A. Microfabrication and microfluidics for tissue engineering: state of the art and future opportunities. *Lab Chip* 2004;4(2):98-103. Epub 2004 Mar 10.
3. Becker H, Gartner C. Polymer microfabrication methods for microfluidic analytical applications. *Electrophoresis* 2000;21(1):12-26.
4. Dass CR. Oligonucleotide delivery to tumours using macromolecular carriers. *Biotechnol Appl Biochem* 2004;40(Pt 2):113-22.
5. Emerich DF, Thanos CG. Nanotechnology and medicine. *Expert Opin Biol Ther* 2003;3(4):655-63.
6. Emerich DF. Nanomedicine--prospective therapeutic and diagnostic applications. *Expert Opin Biol Ther* 2005;5(1):1-5.
7. Eyles JE, Carpenter ZC, Alpar HO, Williamson ED. Immunological aspects of polymer microsphere vaccine delivery systems. *J Drug Target* 2003;11(8-10):509-14.
8. Hombreiro Perez M, Zinutti C, Lamprecht A, Ubrich N, Astier A, Hoffman M, et al. The preparation and evaluation of poly(epsilon-caprolactone) microparticles containing both a lipophilic and a hydrophilic drug. *J Control Release* 2000;65(3):429-38.
9. Jain RA. The manufacturing techniques of various drug loaded biodegradable poly(lactide-co-glycolide) (PLGA) devices. *Biomaterials* 2000;21(23):2475-90.
10. Jeong JC, Lee J, Cho K. Effects of crystalline microstructure on drug release behavior of poly(epsilon-caprolactone) microspheres. *J Control Release* 2003;92(3):249-58.
11. Jiang W, Gupta RK, Deshpande MC, Schwendeman SP. Biodegradable poly(lactic-co-glycolic acid) microparticles for injectable delivery of vaccine antigens. *Adv Drug Deliv Rev* 2005;57(3):391-410.

12. Jilek S, Merkle HP, Walter E. DNA-loaded biodegradable microparticles as vaccine delivery systems and their interaction with dendritic cells. *Adv Drug Deliv Rev* 2005;57(3):377-90.
13. Kalb C. The war on disease goes miniature. *Nanomedicine: drugs and cancer tests, cell by cell*. *Newsweek* 2000;134(26):89.
14. Lengsfeld CS, Manning MC, Randolph TW. Encapsulating DNA within biodegradable polymeric microparticles. *Curr Pharm Biotechnol* 2002;3(3):227-35.
15. Li KC, Pandit SD, Guccione S, Bednarski MD. Molecular imaging applications in nanomedicine. *Biomed Microdevices* 2004;6(2):113-6.
16. Lin WJ, Huang LI. Fabrication of porous poly(epsilon-caprolactone) microparticles for protein release. *J Microencapsul* 2001;18(5):577-84.
17. Mainardes RM, Silva LP. Drug delivery systems: past, present, and future. *Curr Drug Targets* 2004;5(5):449-55.
18. Menei P, Benoit JP, Boisdron-Celle M, Fournier D, Mercier P, Guy G. Drug targeting into the central nervous system by stereotactic implantation of biodegradable microspheres. *Neurosurgery* 1994;34(6):1058-64; discussion 1064.
19. Moghimi SM, Hunter AC, Murray JC. Nanomedicine: current status and future prospects. *Faseb J* 2005;19(3):311-30.
20. Piskin E, Dincer S, Turk M. Gene delivery: intelligent but just at the beginning. *J Biomater Sci Polym Ed* 2004;15(9):1181-202.
21. Ravi Kumar MN. Nano and microparticles as controlled drug delivery devices. *J Pharm Pharm Sci* 2000;3(2):234-58.
22. Reed ML, Wu C, Kneller J, Watkins S, Vorp DA, Nadeem A, et al. Micromechanical devices for intravascular drug delivery. *J Pharm Sci* 1998;87(11):1387-94.
23. Tao SL, Desai TA. Microfabricated drug delivery systems: from particles to pores. *Adv Drug Deliv Rev* 2003;55(3):315-28.
24. Voldman J, Gray ML, Schmidt MA. Microfabrication in biology and medicine. *Annu Rev Biomed Eng* 1999;1:401-25.
25. Weber DO. Nanomedicine. *Health Forum J* 1999;42(4):32, 36-7.

26. Whitesides GM, Ostuni E, Takayama S, Jiang X, Ingber DE. Soft lithography in biology and biochemistry. *Annu Rev Biomed Eng* 2001;3:335-73.
27. Youan BB, Benoit MA, Baras B, Gillard J. Protein-loaded poly(epsilon-caprolactone) microparticles. I. Optimization of the preparation by (water-in-oil)-in water emulsion solvent evaporation. *J Microencapsul* 1999;16(5):587-99.
28. Ziaie B, Baldi A, Lei M, Gu Y, Siegel RA. Hard and soft micromachining for BioMEMS: review of techniques and examples of applications in microfluidics and drug delivery. *Adv Drug Deliv Rev* 2004;56(2):145-72

CHAPTER 3

QUANTITATIVE DIAGNOSTICS USING NONINVASIVE CONTROLLED VENTILATION COMPUTED TOMOGRAPHY OVERVIEW

Respiratory diseases represent nearly 20% of all hospitalizations of children under 15 and account for nearly half of all deaths of American children less than one year of age. Significant morbidity and mortality is attributed to chronic respiratory diseases that have their onset in infancy or early childhood such as cystic fibrosis (CF), bronchopulmonary dysplasia (BPD), and asthma(1). Improving outcome of these diseases depends on innovations in evaluation. A non-invasive method for early and accurate diagnosis and disease assessment is needed.

High resolution computed tomography (HRCT) shows great promise in this regard, particularly when coupled with advances in computational ability (hardware and software) that allow for unprecedented analysis and description of lung structure in normal and disease states (2) (3) (4). For infants and young children, however, the full potential of HRCT has yet to be realized. High quality images obtained under the full range of respiratory volumes in a standardized, reproducible manner are required.

Similarly, techniques that minimize radiation dose to children during CT are imperative (5).

Controlled ventilation high resolution computed tomography (CV-HRCT) is an established noninvasive method of acquiring motion-free images of the lung at a desired lung volume. CV technique is now being used at several major pediatric centers in the U.S. and abroad. During controlled ventilation, children are sedated and breathe spontaneously. After providing a short series of synchronous augmented breaths via a positive pressure facemask (pressure =25 cm H₂O), a transient respiratory pause is induced. Imaging ensues during the pause at selected pressures, typically one for full inflation (25 cm H₂O) and one for expiration (0 cm H₂O) (6). Because respiration is transiently suspended, exams can be performed at much lower radiation doses and remain clinically useful (7, 8). Also, use of a standardized technique minimizes measurement variability resulting from changes in the respiratory pattern of an infant due to respiratory disease.

CV-HRCT imaging at full inflation and exhalation pressures allows unprecedented analysis opportunities for the lung. In addition to characterization of normal HRCT values for infants and young children, a standardized examination of the structure and dynamic response of the lungs and airways to known pressure changes is now possible, including spatially specific lung compliance, airway compliance, and air trapping measures. Such measurements of respiratory function coupled with the additional anatomical information could rival or even supplant pulmonary function testing (9).

Over the past four years, we have performed CV-HRCT in approximately 200 children between 0-6 years of age, which includes over 70 volumetric inspiratory and expiratory scans using an 8 slice multi-detector CT, without any known complications. Of these scans there are normal controls (n=40), cystic fibrosis (n=100), BPD (n=10), asthma (n=10), and interstitial lung disease (n=15) cases. In many instances, a full range of PFT measures were also obtained.

Initial results from image analysis of CV-HRCT exams have been promising. By examining cross-sectional area change of the trachea with pressure change (0-25cm H₂O), infants with tracheomalacia were clearly differentiated from normal children (see Figure 1). Using CV-HRCT, significant airway wall thickness differences were shown between clinically well infants with CF and normal controls using manual measurements (see Figure 2). To fully realize the potential of CV-HRCT technique as a clinical and research tool, the ability to apply computer-generated quantitative analyses referenced to normative data is required (3).

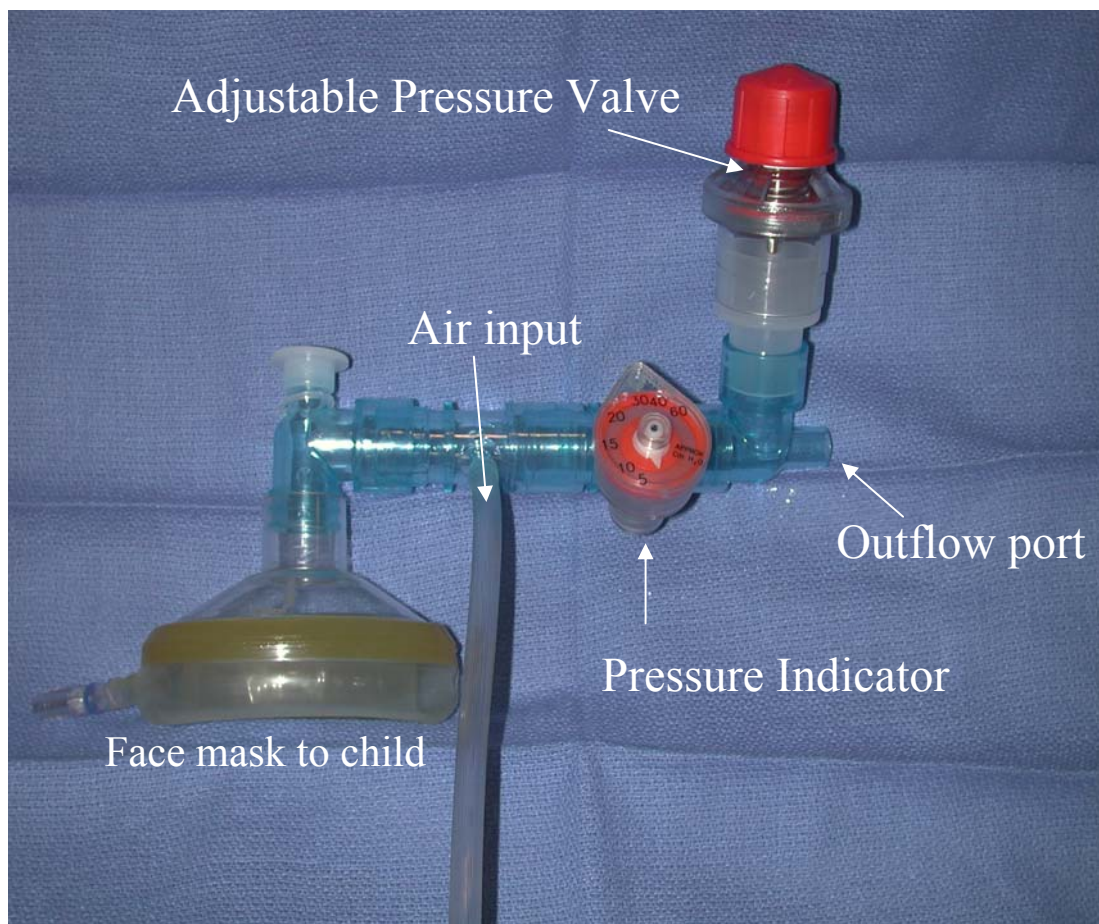


Figure 3.1: Apparatus for non-invasive induction of transient apnea for motion-free, pressure controlled images of the chest. The mask is held in place manually over the sedated child's nose and mouth. Oxygenated air flows continuously through the device by way of the air input. The child breathes freely until the outflow port is occluded. Once this port is occluded the mask delivers whatever pressure set by the adjustable pressure (pop-off) valve (6).



Figure.3.2: Controlled ventilation computed tomography (CVCT) being performed on a child. The technique requires the coordinated effort of two individuals (nurse and respiratory therapist) and the CT scanner technician.



Figure 3.3: Infant pulmonary function test (IPFT) device. Measurements from in controlled ventilation computed tomography (CVCT) were compared to those from IPFTs. Both techniques allow quantitative determinations of lung and airway disease in infants and young children unable to cooperate with breathing maneuvers.

REFERENCES

1. Larsen GL. Asthma in children. *N Engl J Med* 1992;326(23):1540-5.
2. Webb WR, Muller NL, Naidich DP. *High -Resolution CT of the Lung*. 2nd ed. Philadelphia: Lippincott-Raven; 1996.
3. Nakano Y, Muller NL, King GG, Niimi A, Kalloger SE, Mishima M, et al. Quantitative assessment of airway remodeling using high-resolution CT. *Chest* 2002;122(6 Suppl):271S-275S.
4. Jensen SP, Lynch DA, Brown KK, Wenzel SE, Newell JD. High-resolution CT features of severe asthma and bronchiolitis obliterans. *Clin Radiol* 2002;57(12):1078-85.
5. Hollingsworth C, Frush DP, Cross M, Lucaya J. Helical CT of the body: a survey of techniques used for pediatric patients. *AJR Am J Roentgenol* 2003;180(2):401-6.
6. Long FR, Castile RG. Technique and clinical applications of full-inflation and end-exhalation controlled-ventilation chest CT in infants and young children. *Pediatr Radiol* 2001;31(6):413-22.
7. Short RF, Long FR, Adler BH, O'Donovan JC. Ultra-Low Dose Imaging of Pediatric Lungs Using Controlled Ventilation High Resolution Computed Tomography (CV-HRCT). In: *The Society for Pediatric Radiology*; 2003 May 7-10, 2003; San Francisco; 2003.
8. Lucaya J, Piqueras J, Garcia-Pena P, Enriquez G, Garcia-Macias M, Sotil J. Low-dose high-resolution CT of the chest in children and young adults: dose, cooperation, artifact incidence, and image quality. *AJR Am J Roentgenol* 2000;175(4):985-92.
9. Kauczor HU, Hast J, Heussel CP, Schlegel J, Mildemberger P, Thelen M. CT attenuation of paired HRCT scans obtained at full inspiratory/expiratory position: comparison with pulmonary function tests. *Eur Radiol* 2002;12(11):2757-63.

CHAPTER 4

NONINVASIVE METHOD OF QUANTIFYING OF TRACHEAL DISTENSION OBJECTIVELY IDENTIFIES TRACHEOMALACIA IN INFANTS

ABSTRACT

Background Tracheomalacia (TM) is becoming increasingly established as a significant cause of morbidity and mortality in infants and young children and a potentially under recognized etiology of Sudden Infant Death Syndrome (SIDS). Objective evaluation of TM is compromised by the inability of children to cooperate with breathing maneuvers and nonstandard airway pressures during evaluation. A standardized, reproducible method for screening for and quantifying TM is desired. *Purpose* In TM the airway collapses due to its abnormally increased compliance. We hypothesized that TM could be noninvasively distinguished on the inspiratory portion of the pressure/area curve. *Methods* We examined 89 sedated infants and children under 3 years of age for differences in shape and distension of the trachea using a novel method, controlled ventilation computed tomography (CVCT). 33 patients had normal major airways (NL); 48 had cystic fibrosis (CF) but normal PFTs; and 8 patients had TM documented by bronchoscopy. Children were not intubated nor under general anesthesia for any of the

studies: CVCT technique was used to induce two respiratory pauses in each child. During the pauses two CT scans were obtained, one before and one during a step increase in pressure delivered to the airway ($\Delta P = 25 \text{ cm H}_2\text{O}$). Quantitative image analysis of trachea area, sagittal (AP) and coronal (RL) diameters, and perimeter followed. *Results* No significant differences were observed between the CF and NL groups. TM was significantly different in several static measurements such as A_i (area at full inflation, mask pressure $25 \text{ cm H}_2\text{O}$), A_e (area at resting expiration, $0 \text{ cm H}_2\text{O}$) and the corresponding AP diameters as well as calculations of geometric shape. A cutoff of $>50\%$ in distension defined as $((A_i - A_e) / A_i) \times 100\%$ was most reliable for distinguishing TM (100% sensitivity; 100% specificity). *Conclusion* CVCT is a promising noninvasive, objective method for identifying TM.

Introduction

Tracheomalacia (TM) is a potentially life-threatening condition resulting from an abnormal weakness of the trachea. The clinical features of tracheomalacia in children depend on the etiology and include stridor, wheezing, chronic cough, feeding difficulties (*i.e.* apnea with feeds), difficulties breathing, frequent respiratory infections, difficulty clearing secretions and, in more serious cases, attacks of apnea or “dying spells” and even death¹. The latter has implicated TM as a potential unrecognized cause of SIDS^{2, 3}. Because of the overlap of many of these symptoms with other respiratory diseases (*e.g.* asthma) the diagnosis of TM often is delayed and children treated with unnecessary medications⁴. Once thought to be rare, several authors point out that TM may be underdiagnosed because of the failure to suspect it⁴⁻⁶.

The normal trachea is composed of an anterior portion of 16-20 horseshoe-shaped cartilaginous rings and a posterior membranous portion (*pars membranacea*) containing longitudinal and transverse elastic fibers^{7, 8}. Defects in either the anterior cartilage or the posterior membranous portion can cause tracheomalacia. Cartilage defects can be congenital (primary TM) or acquired (secondary TM) as in from prolonged intubation. The former tends to produce a diffuse form of tracheomalacia while the latter is generally focal. Compromise of the structural integrity of the posterior portion of the trachea is seen in TM associated with tracheoesophageal fistulas (TEFs)^{4, 6, 7}. The severity of symptoms dictates the treatment regimen either surgical (aortopexy, reanastomosis) or

stenting. In the diffuse congenital form of TM the disease is thought to be self-limiting with most children outgrowing the disease by age 2 years¹.

During respiration the airway lumen area at any given time is determined by its inherent rigidity (compliance) and the deforming force to which the wall is subjected. As a result of transmural pressures (the difference between intraluminal and intrathoracic) on the trachea wall during inspiration, the trachea normally collapses somewhat with expiration and expands with inspiration⁹ The increased pliability or compliance of the airway wall in TM results in abnormal collapse of the major airway lumen during respiration producing obstruction¹⁰.

We hypothesized that TM can be identified noninvasively in sedated children by quantifying changes in the trachea in relation to a fixed *increase* in intraluminal pressure. This retrospective study takes advantage of a noninvasive facemask ventilation technique known as controlled-ventilation computed tomography (CVCT) to quantify tracheal parameters in children with normal airways (N), children with cystic fibrosis (CF), and children with tracheomalacia (TM). CF distension was studied as well since some authors have suggested abnormal airway compliance in CF^{11, 12} while others disagree¹³.

Methods

Subjects

As part of a separate IRB approved protocol, 89 patients selected for this investigation were retrospectively selected from a pool of previously performed

controlled-ventilation CT (CVCT) studies. The CVCT studies had been performed after informed consent in agreement with prior IRB approval. Individuals comprising the normal group (21 males, 12 females, ages 0.1 – 5 years, length range 55.3-155.4 cm) were selected from the pool of prior CVCT studies in patients with diagnoses not involving the trachea (Table 1). CF patients (confirmed by sweat chloride test) selected (25 males, 23 females, ages 0.2-5.4 years, length 55 – 108.9 cm) had normal or near normal PFTs¹⁴. Tracheomalacia patients (6 males, 2 females, age 0.1-2.7 years, length 48.5-102 cm) were diagnosed either by bronchoscopy, fluoroscopy or both and had been referred for a CVCT for various reasons (Table 2). Retrospective chart review of admission history and physicals for clinical information was conducted. The comorbidities within the TM group included one child with cystic fibrosis, one with Down's syndrome, 2 children with innominate artery syndrome, and 2 children with tracheoesophageal fistulas.

CVCT Imaging

Images selected for review were obtained by the CVCT technique described previously¹⁵. Neither intubation nor general anesthesia are required for CVCT. CVCT involves inducing a transient apnea such that motion free images at known inflation pressures during respiratory pauses. Children are sedated and monitored according to standard imaging protocols (74-100mg/kg oral chloral hydrate or 2-6 mg/kg intravenous pentobarbital). A facemask device (Figure 1) attached to oxygenated air at positive pressure is held over the nose and mouth. Two individuals work to perform the controlled-ventilation technique at the scanner. One operator controls the positive-pressure facemask while the other applies gentle pressure over the cricoid cartilage to

ensure that air does not pass into the esophagus and signals the CT technician to initiate scans. The child breathes spontaneously through the mask at atmospheric pressure when the outflow port is open. When the outflow port is occluded (by the respiratory therapist's thumb) the pressure set by the pop off valve is delivered to the facemask. A series of augmented breaths (generally 3-10) at 25 cm H₂O pressure is given to coincide with the child's own inspiration efforts. The resultant combination of the effects of the Hering-Breuer reflex and a transient hypocarbia produces a pause in respiratory effort of the child sufficient for motion-free imaging. Two pauses were employed for the CVCT scans in this study: one for full inflation of the airway/lungs at 25 cm H₂O pressure and one at 0 cm H₂O pressure (passive expiration). These two pressures provide a standardized change in intraluminal pressure for the quantitative assessment of tracheal distension.

CVCT images of the lungs and airways were obtained using 100-120 kVp, 20-100mAs, 0.5-1 second scan time, bone algorithm, and 1 mm slice thickness using a HiSpeed Advantage scanner (GE Medical Systems, Milwaukee, Wis.). All patients had both full inflation and expiration motion free CT scans as described above. In some cases patients had spiral CT scans (pitch of 1 or 1.5). To minimize radiation dose, in some cases patients had 4-6 anatomical levels scanned. For the purpose of this study only the matched images of the trachea at the level of just above the aortic arch were employed to determine distension (full inflation and expiration).

Image Analysis

Image analysis was performed using Analyze 4.0 software (Biomedical Imaging Resource, Mayo, MN). A_i (area at full inflation) and A_e (area at expiration) were measured along with P_i (perimeter at full inflation) and P_e (perimeter at expiration). Diameter measurements were performed as well. All measurements were made for matched images at the two known pressures (25 and 0 cm water), corresponding to full inflation and expiration. A semi-automated thresholding technique using the full-width half maximum principle was employed to measure the cross sectional area (CSA) of the trachea. The corresponding trachea circumference was measured and recorded as the trachea perimeter. Tracheal diameters were measured from one point to the other side of the computer generated perimeter curve in both the coronal (right to left, RL) and the sagittal (anterior to posterior, AP) planes. Percent (%) distension was calculated as $((A_i - A_e)/A_i) \times 100\%$ and similarly using diameters, ($\% \text{ diameter distension} = ((D_i - D_e)/D_i) \times 100\%$)).

Indices of the geometry/shape of the trachea were calculated and examined for differences at two pressures for the three patient groups (N, CF, TM). A tracheal index¹⁶ (TI) was calculated as the ratio of the coronal (RL) diameter to the sagittal (AP) diameter (RL/AP) and examined for differences among the groups at inspiration and expiration. A second more global index of shape, normalized “circularity”, was examined as well at inspiration and expiration and their difference. The circularity measurement relies on geometry of trachea as it relates to a circle. For a perfect circle, the relationship of the perimeter to the area is such that if the perimeter is squared and divided by the area the result is 4π ($(2\pi r)^2/\pi r^2 = 4\pi$). Dividing this calculation by 4π provides a normalized value.

Though the trachea is not a perfect circle, its geometric relationship to a circle is a specific value at both expiration and inspiration.

Statistical Analysis

Statistical analysis was conducted using the SAS computing package (Cary, North Carolina). Data were expressed as means and SD. Using the general linear model procedure analyses of variance (and analysis of covariance with child length) were conducted according to the Student Neuman Keuls (SNK) method. Post tests comparing parameters between the normal, CF, and TM groups were conducted by the Tukey-Kramer method to adjust for multiple comparisons. Regression analysis (general linear model, least squares method) followed. An alpha < 0.05 was considered to be statistically significant.

Results

Table 3 shows the results of the comparisons between the groups. There were no significant differences between the normal and CF groups for the parameters examined. Significant differences for TM were observed Ai and Ae, but for the 8 patients studied the trachea was not always smaller at expiration or even larger at inspiration when compared to children of the same size (see Figures 2 and 3). However, if a cutoff of >50% is employed for distension then all cases of of TM are clearly distinguished (sensitivity %100, specificity 100%) (Figure 4). The values (mean \pm SD, range) for

distension based on areas ($(A_i - A_e / A_i) * 100\%$) were: N (21 ± 8 , 7-39%); CF (20 ± 9 , 4-37%); TM (64 ± 10 , 51-80%). Distension values based similarly on AP diameter changes were N (21 ± 10 , 3-38%); CF (16 ± 8 , -3-32%) TM (52 ± 10 , 41-67%). Measurements of sagittal (AP) diameters were also significantly different at full inflation and expiration. However, the distinction of TM is much less clear when examining the changes in sagittal diameter as shown in Figure 5. When considering AP diameters the threshold of a change $> 50\%$ does not identify TM reliably (50% sensitivity with 100% specificity). Measurements of distension did not vary significantly with age or length for any of the groups

Measurements of perimeter at expiration and the percent change between full inflation and expiration were significantly different for TM compared to the other groups but not at full inflation (see Table 3). Calculations of geometrical shape of the trachea produced interesting results. The TI (AP/RL diameter) at inflation differed significantly only between the normal and the TM groups but with notably less power ($p = 0.0473$) whereas the same comparison between the CF and TM group was not significant ($p = 0.187$). The TI at expiration and the change with inflation differed more significantly between the groups ($p < 0.0001$). Differences in geometric shape for TM as measured by circularity were more pronounced at full inflation ($p \geq 0.0543$) but lacked statistical significance, (TM = 0.985 ± 0.63 ; CF = 1.275 ± 0.071 ; N = 1.282 ± 0.11). Differences were not apparent at expiration for circularity among the groups ($p > 0.9$; TM = 0.977 ± 0.62 ; CF = 1.264 ± 0.099 ; N = 1.301 ± 0.071); however, the change in circularity from inflation to expiration was significantly different for the TM group ($p < 0.01$).

Discussion

The abnormal collapse of the trachea in TM with changes in pressure was described nearly forty years ago⁵. The diagnosis of TM, though, was until recently thought to be rare likely for two reasons: 1) the lack of clinical suspicion and 2) the lack of an objective, noninvasive means of testing for it. The former has been ameliorated recently due to increased attention in the literature^{3, 6, 8, 17}, likely due in part to advances in both airway imaging and treatment options. The latter has been addressed by advances in imaging, but the inability to cooperate with breathing maneuvers hinders their application to infants and young children⁶. Thus, the diagnosis of TM has remained the most difficult to make in the population in which it is the most common and the most often life-threatening.

In this study we demonstrate in infants and young children that a simple, noninvasive technique (CVCT) can be used to obtain measurements of the trachea in relation to a known increase in intraluminal pressure. This method allows identification of tracheomalacia because of the increased compliance of the airway in tracheomalacia. The static measurements obtained provide a standardized, reproducible means to objectively determine tracheal dynamics in infants and small children (who are unable to cooperate with breathing maneuvers). While TM was most evident by pressure/area changes (distension), dynamic changes in the geometry of the trachea also distinguished tracheomalacia. For the children with cystic fibrosis there were differences in the size, shape or distensibility compared to children of the same size with normal tracheas.

While characteristic changes in AP diameter and distension were expected for TM, some of our results merit further discussion. In CVCT the expiratory phase is not an active one. Instead the mask pressure is at zero and the pressure within the airway is assumed to be ambient and the lungs are at functional residual capacity (FRC)¹⁵. Interestingly, even at this passive state of expiration the airway in TM exhibited significant differences in shape as indicated by the TI. Examination of shape through the circularity index, though, did not distinguish TM with either static measurement (inflation or expiration). Only in evaluation of the dynamic change in circularity did TM significantly differ. Also noteworthy is that the perimeter for TM was significantly different in expiration but not inflation. This result seems counterintuitive but might be explained as follows. The 25 cm H₂O of inflation pressure employed in CVCT to approximate the pressure of a fully inspired breath¹⁵. While the change in intraluminal pressure ($\Delta P = 25 \text{ cm H}_2\text{O}$) is sufficient to cause movement of the airway, the inflation pressure (stress) is not so substantial to cause appreciable stretch (strain) of the airway tissues. The apparent situation is desirable in that the dynamics of the airway are elicited while the risk of barotraumas to the airway is minimized. The observation of significantly smaller perimeters at expiration was most likely influenced by measurement methodology. Automated perimeter measurements are made along the line approximating the 50% Hounsfield unit (HU) value between air and tissue outlining the trachea. When the trachea is in a more collapsed state, as seen in TM, the airway walls are brought into closer approximation and in some cases touching especially near corners. This “cornering effect” produces a slight reduction in the perimeter measurement at expiration by reduction in the length of the computer-generated outline. Given that

diameters were measured from point to point on the perimeter curves, this may also explain the negative measurement (-3%) seen for AP diameter distension in a 3-year-old CF patient. Another plausible explanation is that this result reflects the tolerance of our measurement system.

Study limitations

Limitations of this study included the small number of tracheomalacia patients studied (n = 8). The etiology of the TM and other comorbidities may have impact on the quantitative assessment of airway distension. Whether or not diffuse pulmonary fibrosis or airtrapping can affect CVCT measurements of airway distensibility is not yet clear. Also, in this study we examined only one level of the intrathoracic trachea. Because TM most often affects the distal third of the trachea⁸, we choose the level at the superior border of the aortic arch. We studied only an intrathoracic portion of the airway. Extathoracic tracheomalacia or laryngomalacia traditionally behaves differently than the intrathoracic variant. Airway collapse tends to occur with inspiration instead of expiration as in the intrathoracic variant. It seems unlikely that assessing airway compliance by CVCT, though, would be affected by this phenomenon. Our more recent investigations of the entire tracheobronchial tree with spiral CVCT scans have shown distension of the airway does vary along the length of the trachea but normally still less than %50. Whether this cutoffThough we observed no difference for the tracheas of CF patients, the group studied had normal or near normal PFTs. Our study does not adequately address whether more severely affected CF patients develop more distensible airways later in life but does seem to imply they are not born with tracheal differences.

Drawbacks of the CVCT technique itself include the ionizing radiation associated with CT. An inherent advantage of CVCT, though, is the elimination of motion unsharpness. The high intrinsic contrast of the airways and elimination of motion allow scans be conducted with settings corresponding to ultra-low CT radiation doses (100-120 kVp, ≤ 20 mAs). Sedation of children for CVCT is not without risk and therefore CVCT is not recommended for in situations where sedation is contraindicated. Overall, CVCT is very safe and > 400 studies have now been performed at our institution without incident.

Other diagnostic methods for identifying airway malacia

In addition to physical exam and a thorough review of the patient's history, several modalities can be employed for the diagnosis of TM. PFT flow-volume loops can show characteristic changes for TM but do not pinpoint disease. Plain radiographs, including inspiratory and expiratory views, do not reliably identify TM¹⁸. Airway fluoroscopy has been used as a cost-effective screening tool to subjectively evaluate airway dynamics and can identify other involved structures¹⁹. Endoscopy has traditionally been revered as the gold standard for evaluation of TM. However, for both fluoroscopy and endoscopy, the diagnosis of TM is subjective in that the pressures acting on the airway are unknown¹⁷. Endoscopy is further hindered by the presence of the endotracheal tube and fiberoptic scope, which may alter flow dynamics within the airway lumen. The procedure also requires anesthesia and can be costly and time-consuming. The advantages of endoscopy, though, are the simultaneous evaluation for laryngomalacia as well as the potential for intervention (stenting).

Cross-sectional imaging modalities have been increasingly used to identify TM and quantify airway collapse by imaging during respiration or during special breathing maneuvers²⁰⁻²⁴. These modalities visualize the airway lumen and also allow illustration of other involved structures. Of these quantitative studies, only a study with cinetomography focused on TM in infants presumably, due to the limitations of radiographic imaging of the airways in young children. Other studies have used endoscopy and image analysis to quantify airway collapse in infants and young children with TM and TBM^{17, 25}. Only the study by Okazaki *et al* attempted to control airway pressures when demonstrating airway collapse in TM¹⁷.

Though recent advances in central airway imaging have provided additional means of diagnosing tracheomalacia, they are limited by reliance on breathing maneuvers (*e.g.* coughing, breathholding) to demonstrate airway collapse. The forces generated by these maneuvers vary from individual to individual or even within the same individual. The variance in forces compromises the ability to make standardized assessment of tracheomalacia¹⁷. Children are unable to cooperate with breathing instructions and the diagnosis must be made while quietly breathing or by eliciting collapse of the airway by agitating the child. Clinically, TM symptoms generally are not present while quietly breathing and cases of TM can be missed when assessing the unstressed airway^{6, 17, 22}. Some degree of agitation (crying) must be employed to demonstrate collapse. As pointed out in a footnote by Wittenborg *et al* in 1967, even in the normal infant the trachea may collapse when the infant struggles⁹. The increased central airway wall motion is not because there is increased tracheal compliance but

rather because the transmural pressure swings are large²⁶. This can lead to overestimation of tracheal collapse. The ability to elicit such a response can be variable in an anesthetized child⁶. Also, anesthetic agents are known to decrease airway smooth muscle tone, potentially decreasing airway compliance leading to an overestimation of collapse¹⁷. Also, the introduction of a foreign body into the airway lumen upstream of the point observed influences airway dynamics such that collapsibility can be overestimated.

Missing from the equation in these determinations is the degree of transmural pressure changes. The recent study by Okazaki *et al* recognized this shortcoming and quantified by tracheal collapsibility by endoscopy in intubated, anesthetized, paralyzed children. Their study quantified tracheal collapse to identify TM based on a step decreases in airway pressure¹⁷. Our study similarly quantifies the pressure/area (compliance) relationship of the trachea, but instead employs a step increase in airway pressure (without intubation or general anesthesia). Quantitative CVCT thus allows a standardized objective examination of the airway dynamics on the inflation limb of the pressure-area curve.

Study Implications

Improved Diagnosis and Management of Disease

This body of work may be of interest to anesthesiologists, otolaryngologists, cardiothoracic surgeons, pulmonologists, pediatricians, and radiologists alike. As many as a third of infants and young children referred for bronchoscopy for respiratory symptoms

are found to have some component of tracheomalacia. Often these children are referred after being treated for prolonged periods with antibiotics for presumed respiratory infections or having failed treatment for severe asthma with steroids⁸. Diagnosis and management of major airway disorders can be greatly enhanced with CVCT. Given the tendency of congenital TM to resolve with time, CVCT allows the ability to quantify and follow the disease for resolution. When combined with helical scanning, quantitative analysis of the entire tracheobronchial tree is possible. CVCT studies are easily combined with intravenous contrast to identify vasculature structures, such as innominate artery or aberrant aortic arch. The ability to control breathing status allows the application of many other CT based advents to be applied to infants such as quantitative analysis of lung parenchyma, airtrapping, bronchiectasis, and visualization of cardiopulmonary anomalies. We have had success with CVCT clinically in assessing TBM, IAS, and airway stenosis. Further quantitative studies in these conditions and others with CVCT are underway.

Pretreatment Planning

In cases requiring intervention, CVCT is of great value in treatment planning. Response to therapy and interventions can be objectively and noninvasively assessed. Full discussion of the management of TM and TBM is reviewed elsewhere^{3, 6, 8}. Because CVCT evaluates tracheal dynamics on the inspiratory portion of the pressure-area curve, the main airways are fully distended at a physiologic full inflation pressure. The airway lumen area at this point is of greatest interest for selecting stent sizes. Stents too large can cause pressure necrosis; stents too small may fail due to migration. One

recent study with silicone stents showed that the majority of failures were due to stent migration that could have been avoided by use of a larger stent²⁷. Indeed, we have observed that for a series of infants and young children (n=15) who underwent both CVCT and CT during respiration (during the same sedation), automated CT measurements of the tracheal lumen during respiration are $23 \pm 9\%$ smaller than those obtained at CVCT full inflation. The ability to measure a fully inflated airway by CVCT before stent placement may be of great value given that stent failure can be lethal.

Airway malacia and SIDS

The difficulty of the diagnosis and potential mortality of TM support the theory that primary TM and/or tracheobronchomalacia (TBM) may be an under recognized cause of sudden infant death syndrome (SIDS)³. The theory for TM as one potential etiology of SIDS is substantiated clinical course of the disease: Both SIDS and congenital TM present at a similar time, from one month to one year of life. Primary TM generally presents only after symptom-free interval (weeks to months) early in life and (in nonlethal cases) often resolves within the first one or two years of life⁶. Both are more common in males, premature infants, children with reflux and seem to have strikingly similar incidence. Though the incidence of primary TM is difficult to estimate, one recent study²⁸ estimated it to be 1/1445 or 0.69 per 1000 live births. The data for 2001 showed the SIDS incidence to be 0.67 per 1000 live births (1/1493). In their 2005 report, Malloy and MacDorman show that the overall postneonatal rate of death has not declined with the decline in SIDS incidence. The multidisciplinary increase in focus in the

literature relating to the diagnosis of TM has coincided with the apparent success of the “back to sleep” campaign and perhaps shifts in classification of SIDS deaths²⁹.

Another possible explanation for success of the SIDS “back to sleep” campaign might be due in part to the changes in forces on the trachea between the prone and supine positions. The prone position may increase compression by extraluminal posterior structures or cause changes in pressures generated within the chest (presumably increased while prone) leading to increased tracheal collapse. Autopsy studies have shown that SIDS victims show definitive signs of having suffered chronic hypoxia prior to death³⁰, as might occur with chronic airway collapse. Studies in animals exposed to hypoxia chronically demonstrate decreased chemoresponses and arousals from sleep with airway obstructions^{31, 32}. Frequent obstruction, as with primary malacia, thus may lead to death from lack of response to a severe obstruction while sleeping. At autopsy, airway malacia may not be evident due to the lack of dynamic airway information.

Though speculative, the association between airway malacia and SIDS is worth investigating. The association of TM and SIDS has been reported elsewhere in the literature but has received little focus recently. Airway malacia was identified as the etiology of SIDS in multiple children in a 1988 report³³, and in 1983 TM was reported as the cause of near miss SIDS in four of 58 cases studied². Of interest both of these reports predate more sophisticated diagnostic means for identifying TM. It seems likely, therefore, that airway malacia likely represents a significant and underidentified etiology of SIDS, underscoring the need for an objective, noninvasive means to reliably screen for

airway malacia in infants. Quantitative airway evaluation with CVCT appears to be promising in this regard.

Conclusion

CVCT is a simple, noninvasive method to assess airway dynamics in infants and young children in an objective, in a standardized reproducible manner using the inspiratory limb of the pressure/area curve. Compared to children of the same age with normal major airways, children with tracheomalacia show distinct changes in distension and shape while children with asymptomatic cystic fibrosis do not. At 100% sensitivity and 100% specificity in the 8 TM patients studied, a threshold of >50% distension by cross-sectional area is more reliable for distinguishing TM than are changes in sagittal (AP) diameters. CVCT measurements of the lumen of major airways based at full inflation may improve stent performance by minimizing stent migration. CVCT may be a valuable research tool to screen for and investigate tracheomalacia, a potentially under recognized cause of SIDS. Further study is required to fully evaluate the potential of quantitative CVCT for screening of disorders of the major airways including tracheomalacia.

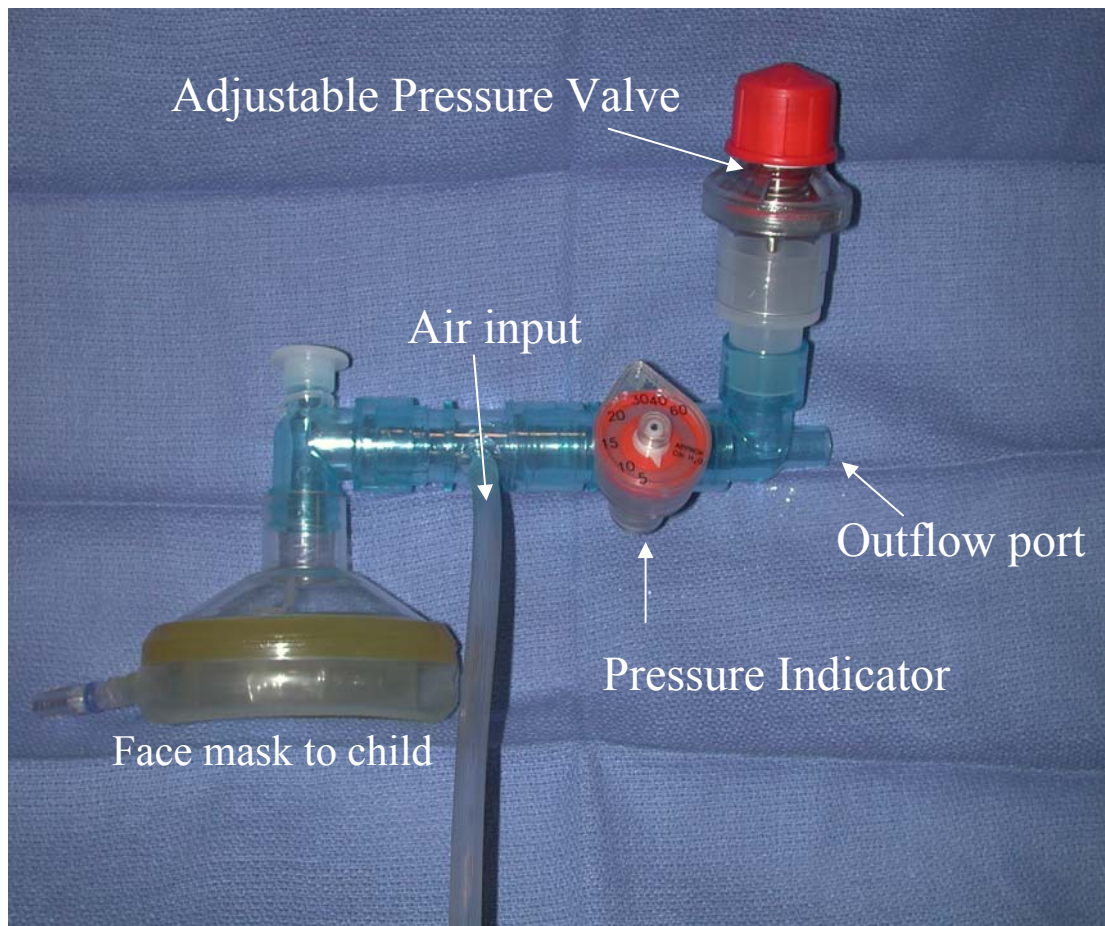


Figure 4.1: Apparatus used in CVCT for non-invasive induction of transient allowing for motion-free, pressure controlled images of the chest. The mask is held in place manually over the sedated child's nose and mouth. Oxygenated air flows continuously through the device by way of the air input. The child breathes freely until the outflow port is occluded. Once this port is occluded the mask delivers whatever pressure set by the adjustable pressure (pop-off) valve. The components of the system are common to most pediatric pulmonology units.

Sex	Length (cm)	Age (weeks)	Diagnosis	Reason for Chest CT
M	55	6	Transient tachypnea newborn	R/o abnormality
F	57	7	Silent aspiration	R/o airways disease
F	59	6	Transient tachypnea newborn	R/o abnormality
F	66	20	Liver hemangiomas	Staging
F	69	32	Hepatoblastoma	Staging
M	70	52	Wilms tumor	Staging
F	71	47	Leg hemangioma	Staging
M	72	44	Gastroesophageal reflux	Silent aspiration
M	72	42	Testicular tumor	Staging
M	73	78	Ocular myasthenia gravis	R/o thymoma
F	74	41	Orbital rhabdomyosarcoma	Staging
M	75	53	Aspirated bean	Fever
M	75	45	Neuroblastoma	Staging
F	76	112	Wilms tumor	Staging
M	76	54	Wilms tumor	Staging
F	78	72	Asthma	R/o airways disease
M	80	61	Neuroblastoma	Staging
M	82	97	Dysphagia	R/o mediastinal mass
M	83	92	Fever unknown origin	Fever
F	84	89	Ovarian teratoma	Staging
M	86	144	Recurrent pneumonia	R/o sequestration
M	89	100	Chronic cough	R/o foreign body
F	89	121	Intestinal duplication cyst	IRB protocol

Continued

Table 4.1. Patient characteristics of normal reference group. Mean \pm standard deviation for length, 82.1+14.6 cm; age, 97.3+/-67.9 weeks.

Table 4.1 Continued

M	90	119	Recurrent pneumonia	R/o bronchiectasis
M	94	156	Silent aspiration	R/0 airways disease
F	95	155	Recurrent pneumonia	R/o bronchiectasis
M	97	187	Leukemia	Pre-BMT evaluation
M	98	166	Mediastinal mass	Post therapy follow-up
M	98	148	Ventricular arrhythmia	R/o amiodorone toxicity R/o small esophageal foreign body
M	101	173	Dysphagia	
F	103	200	Recurrent pneumonia	R/o bronchiectasis
M	106	260	Idiopathic hemosiderosis	R/o interstitial disease
M	115	232	Recurrent hepatoblastoma	Staging

Sex	Age (Weeks)	Length (Cm)	Diagnosis	Reason Chest CT	Distension* (%)	Clinical Info
M	8.0	64.0	Bronch, IPFTs	R/o Innominate artery syndrome	59.2	Noisey breathing since birth; apnea with feeding
F	16.0	48.5	Bronchoscopy	R/o metastatic lung disease	79.9	Feeding intolerance; tracheoesophageal fistula; neuroblastoma Noisey breathing: low-pitched croaking sound with both inspiration and expiration; spells of sudden cough and distress while sleeping
M	20.0	62.0	Fluoro & Bronch	R/o airway obstruction	50.8	Stridor and course breathing since birth. Innominate artery compressing the trachea. Aortoplexy performed. Expiratory wheeze and respiratory distress, decreased when sleeping. Albuterol not helpful, potentially exacerbates problem.
F	96.0	82.5	Bronchoscopy	R/o innominate artery syndrome	58.5	
M	18.0	57.4	Bronchoscopy	CF follow-up	54.7	

Continued

Table 4.2: Characteristics and clinical chart information of study patients with diagnosed with tracheomalacia.. Distension (%) was calculated as $100\% * ((A_i - A_e) / A_i)$ where A_i = area at paused inspiration (25 cm H₂O mask pressure); A_e = area at paused expiration ($A_e = 0$ cm H₂O mask pressure). R/O = rule out; Fluoro = fluoroscopy; bronch = bronchoscopy.

Table 4.2 Continued

M	36.0	76.0	Fluoro & Bronch	R/o airway obstruction	73.8	Chronic noisy breathing. Awakenings with cough, rattling, wheezing appreciable since birth. Albuterol not helpful. Worse when excited, eating, or hot.
M	7.4	55.4	Bronchoscopy	R/o airway obstruction	64.0	Noisy breathing since birth; choking with feeds; H-type tracheoesophageal fistula
M	141.0	102.0	Bronchoscopy	R/o airway Obstruction	67.8	Down's syndrome; aspiration; coarse rhonchi heard bilaterally

	NL vs CF	NL vs TM	CF vs TM
Areas			
Ai	0.2976	0.0056	0.0003
Ae	0.2183	0.0007	0.0138
(Ai-Ae)/Ai	0.8994	<0.0001	<0.0001
Sagittal (AP) Diameter			
Di (AP)	0.8673	<0.0001	0.0001
De (AP)	0.7545	<0.0001	<0.0001
(Di-De)/Di	0.0756	<0.0001	<0.0001
Perimeter			
Pi	0.9634	0.8393	0.9038
Pe	0.9759	<0.0001	<0.0001
(Pi-Pe)/Pi	0.9112	<0.0001	<0.0001
Shape, TI = RL/AP			
Inflation	0.4489	0.0473	0.187
Expiration	0.9068	<0.0001	<0.0001
(Inf-Exp)/Inf	0.6402	<0.0001	<0.0001
Shape—Circularity			
Inspiration	0.9984	0.0599	0.0543
Expiration	0.9938	0.9967	0.9888
(Inf-Exp)/Inf	0.9938	0.0095	0.0086

Table 4.3 P values from comparisons of static and dynamic (%changes) measurements of tracheal dimensions, distension and indicators of shape for NL, CF, TM groups.

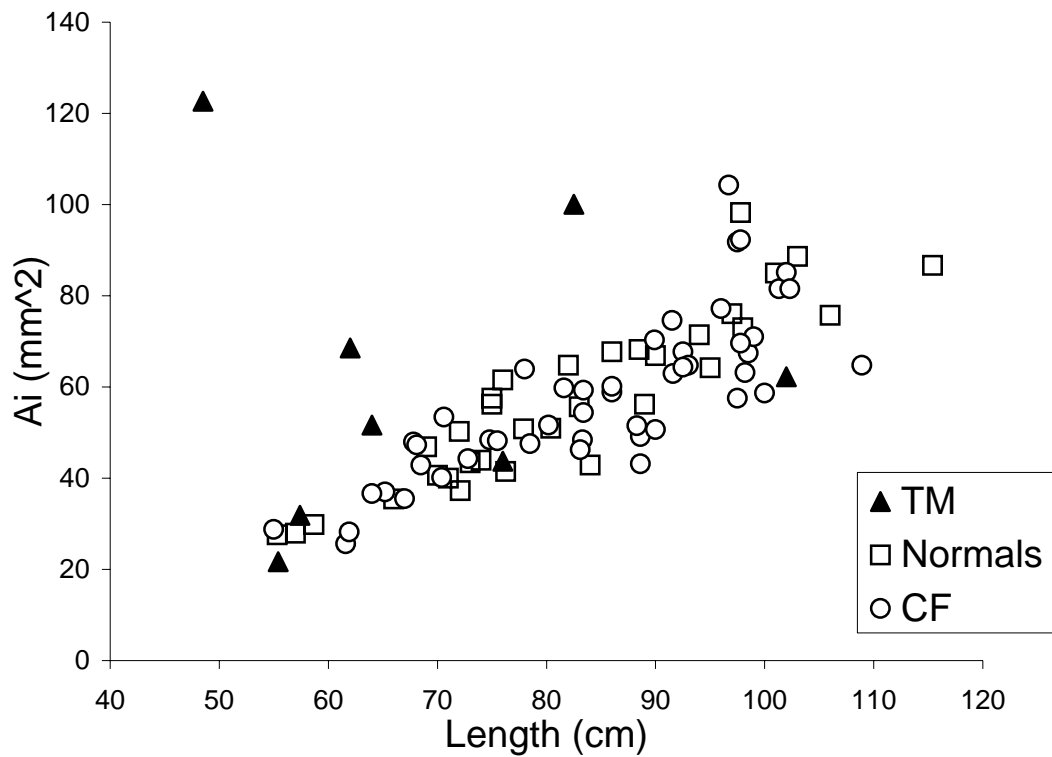


Figure 4.2. Graph showing trachea area at full inflation (A_i) with 25 cm H_2O mask pressure for children with normal tracheas (NL), cystic fibrosis (CF), and tracheomalacia (TM). The length-adjusted mean of A_i for TM patients was significantly different than those of NL and CF patients of the same length ($p < 0.006$), but A_i does not itself reliably distinguish TM. Length-adjusted A_i for CF and NL patients did not differ significantly.

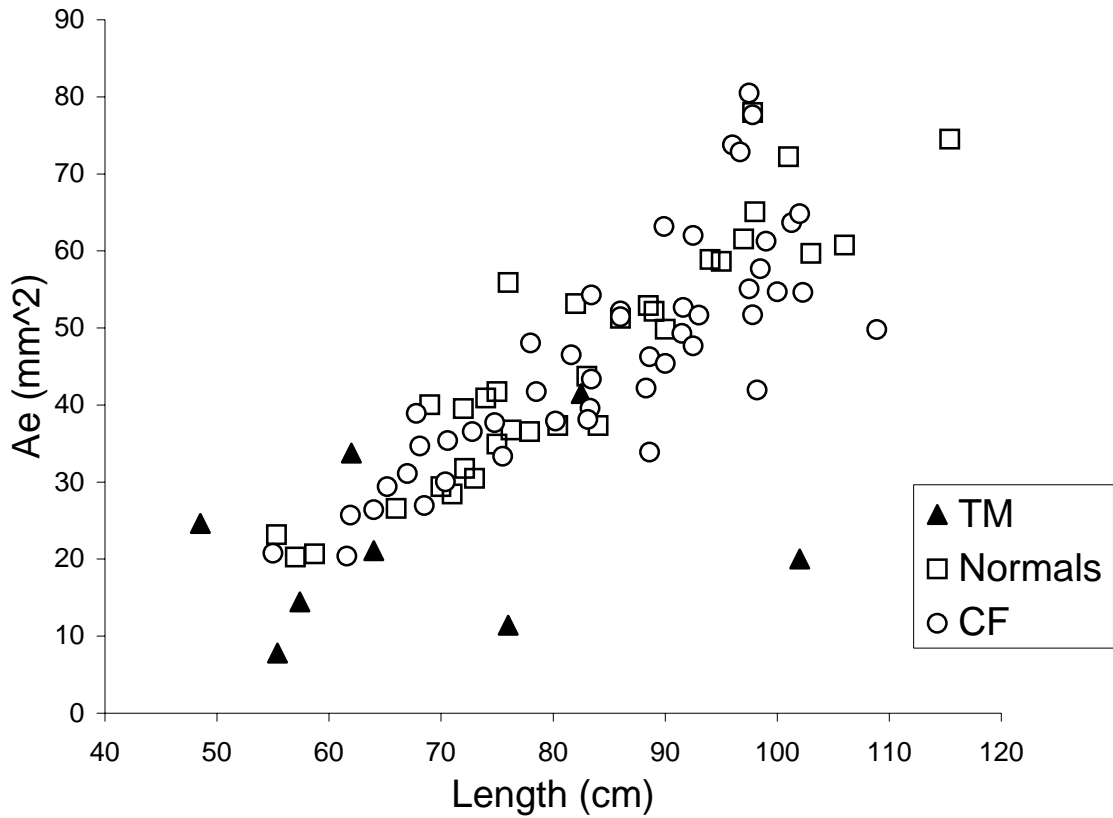


Figure 4.3. Graph showing trachea area at paused expiration (A_e) with 0 cm H_2O mask pressure for NL, CF, and TM groups. The length-adjusted average A_e for TM patients was significantly smaller than those of NL and CF ($p < 0.0138$), but A_e does not itself reliably distinguish TM. Length-adjusted A_e for CF and NL patients did not differ significantly ($p = 0.2183$).

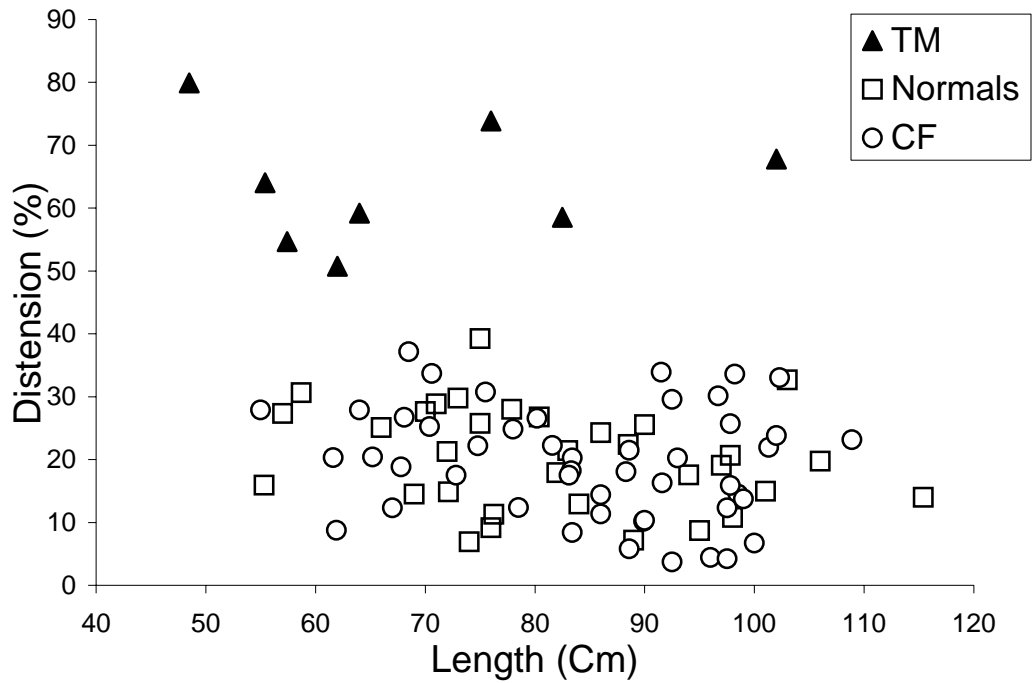


Figure 4.4. Graph shows tracheal distension (%) as a function of length for NL, CF, and TM groups. Distension (%) was defined as $((A_i - A_e / A_i) / A_i) \times 100\%$, where A_i and A_e are areas measured at 25 cm and 0 cm H_2O mask pressure, respectively ($\Delta P = 25$ cm H_2O). Distension for TM was significantly different than both CF and NL ($p < 0.0001$), whereas NL and CF did not significantly differ.

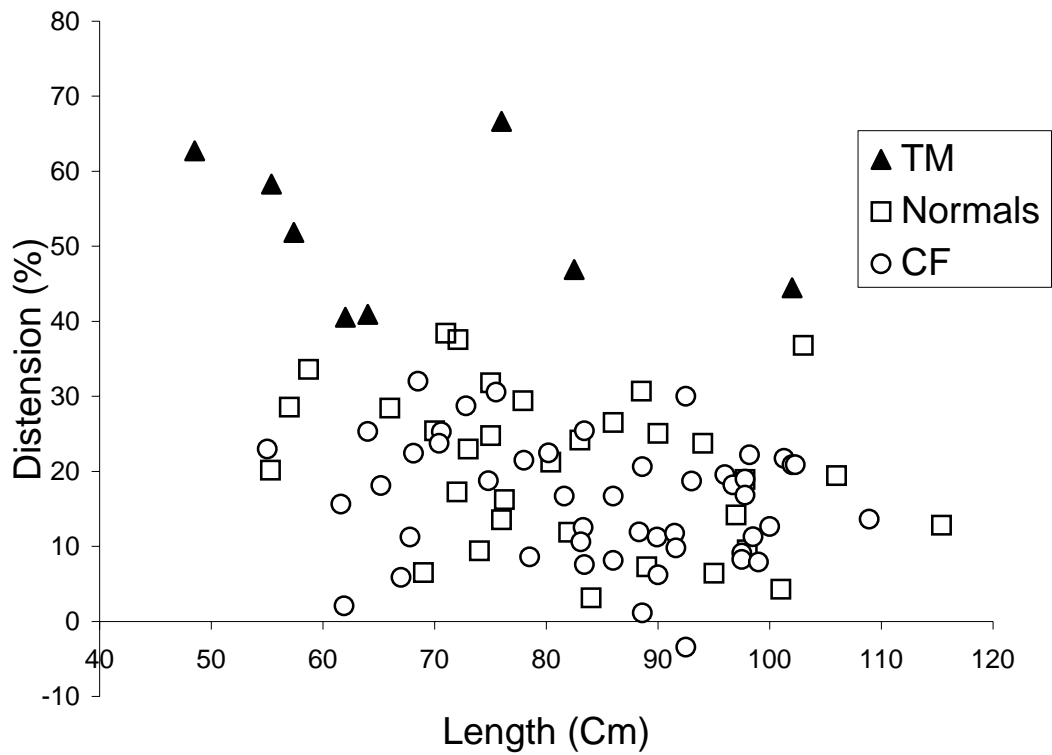
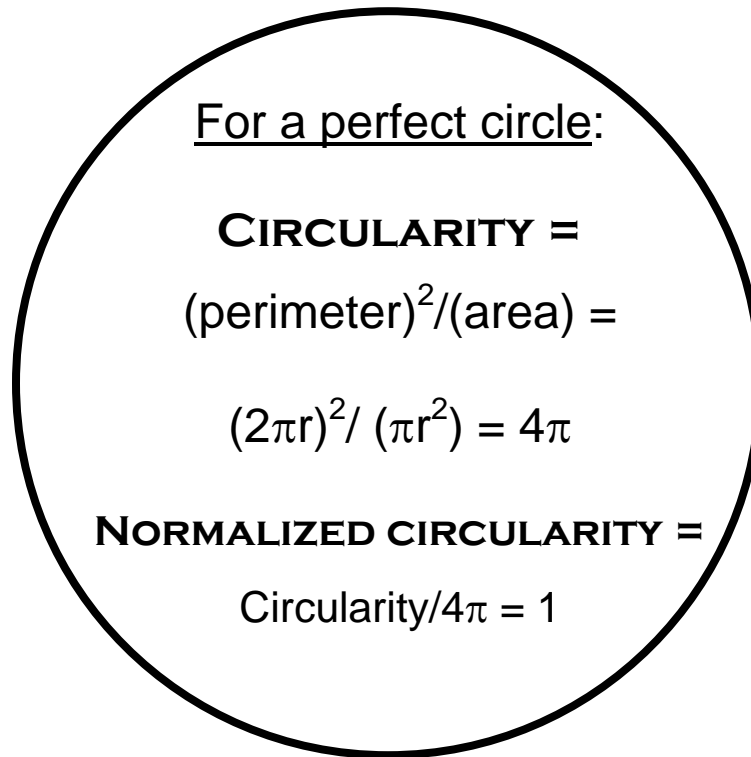


Figure 4.5. Graph shows changes in anterior-posterior (AP) diameters between inspiration and expiration for CF, NL, and TM patients by length. Though the average TM is significantly different ($P < 0.001$), only four (4) of the 8 studied TM patients had changes in the AP diameter greater than 50% between measurements. No significant difference exists between CF and NL patients.



For a perfect circle:

CIRCULARITY =
 $(\text{perimeter})^2 / (\text{area}) =$
 $(2\pi r)^2 / (\pi r^2) = 4\pi$

NORMALIZED CIRCULARITY =
 $\text{Circularity} / 4\pi = 1$

Figure 4.6: Method for quantifying the geometry of the trachea using perimeter and area measurements. Bronchoscopic diagnosis of tracheomalacia relies on subjective determination the appearance and behavior of the trachea during bronchoscopy. This calculation of circularity allows the geometry of the trachea to be quantified.

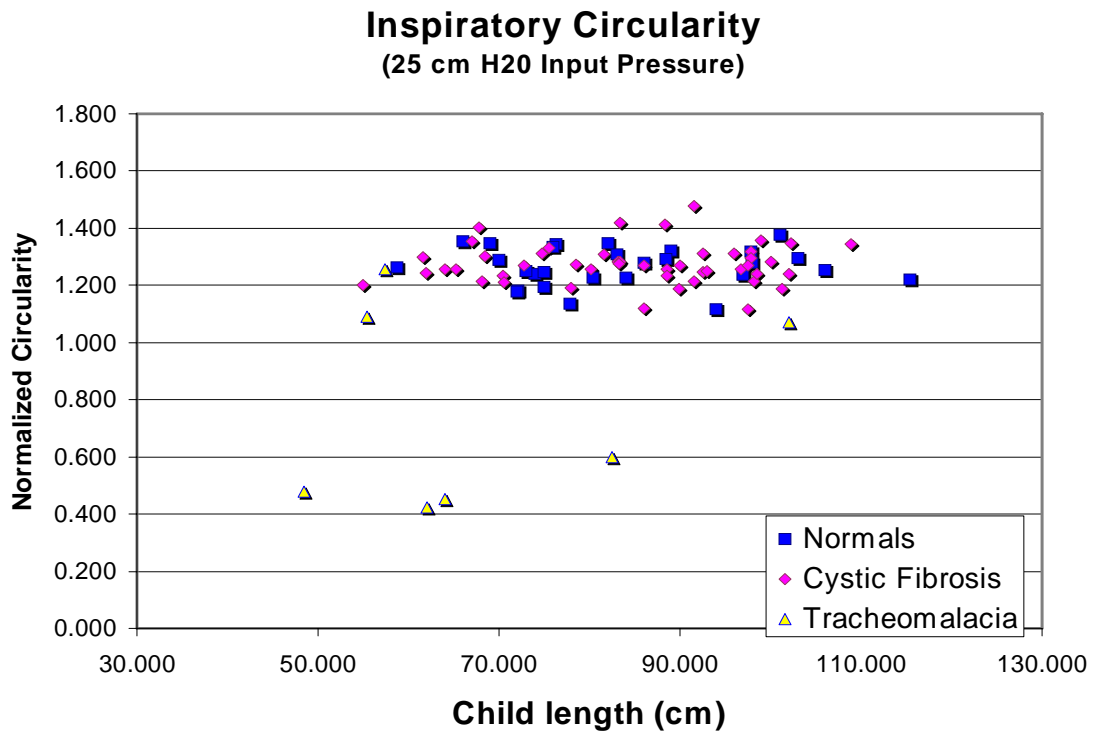


Figure 4.7: Normalized circularity of the trachea by length during paused inspiration (25 cm H₂O mask pressure). Normalized circularity is calculated as $[P^2/A]/4\pi$; where P = perimeter and A = area. One TM outlier is omitted. TM patients were significantly different than normal and CF patients; there is no significant difference between normal and CF patients.

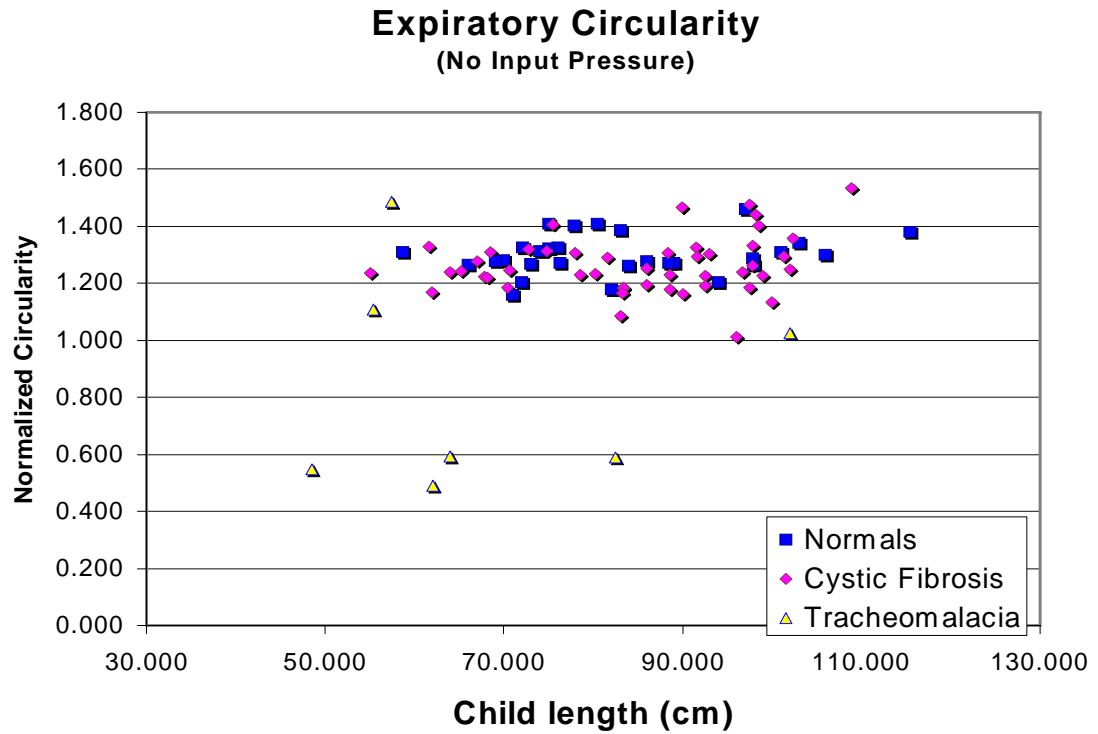


Figure 4.8: Normalized circularity of the trachea by length during paused expiration (0 cm H₂O mask pressure). Normalized circularity is calculated as $[P^2/A]/4\pi$; where P = perimeter and A = area. One TM outlier is omitted for display. TM patients were significantly different than normal and CF patients; there is no significant difference between normal and CF patients.

Figure 4.9: Quantitative analysis curves of a normal trachea using CVCT. The top curve shows areas at inspiration and expiration with the corresponding percent difference (distension). Note that the values increase only slightly from inspiration to expiration and the shapes of the curves are almost identical for both circularity and perimeter.

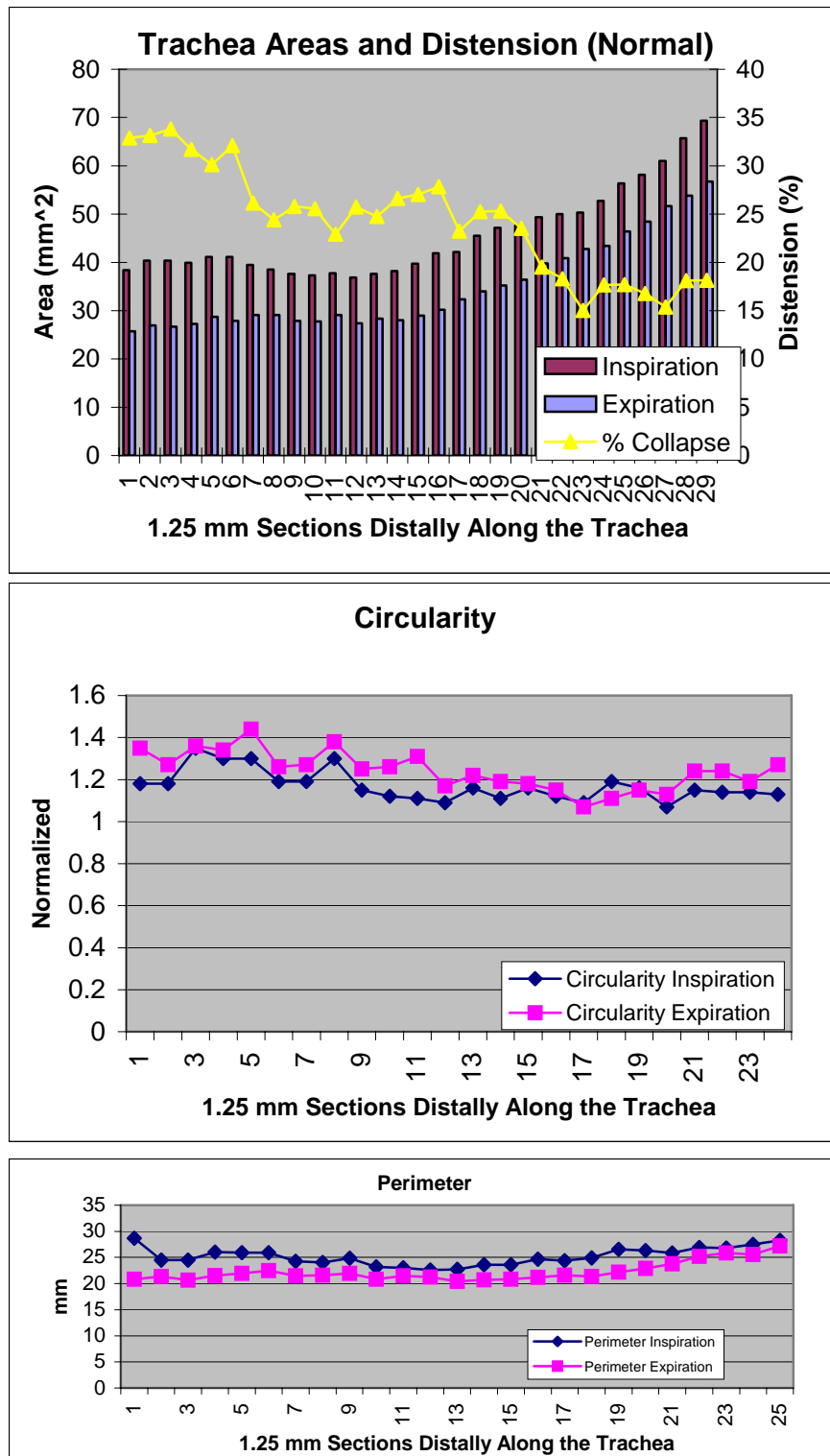


Figure 4.9. Quantitative analysis curves of a normal trachea using CVCT.

Figure 4.10: Quantitative analysis curves of a trachea in a patient with cystic fibrosis.

The shape and values of these curves is similar to that of a normal child. There is little or no change in circularity and the perimeter difference is relatively constant.

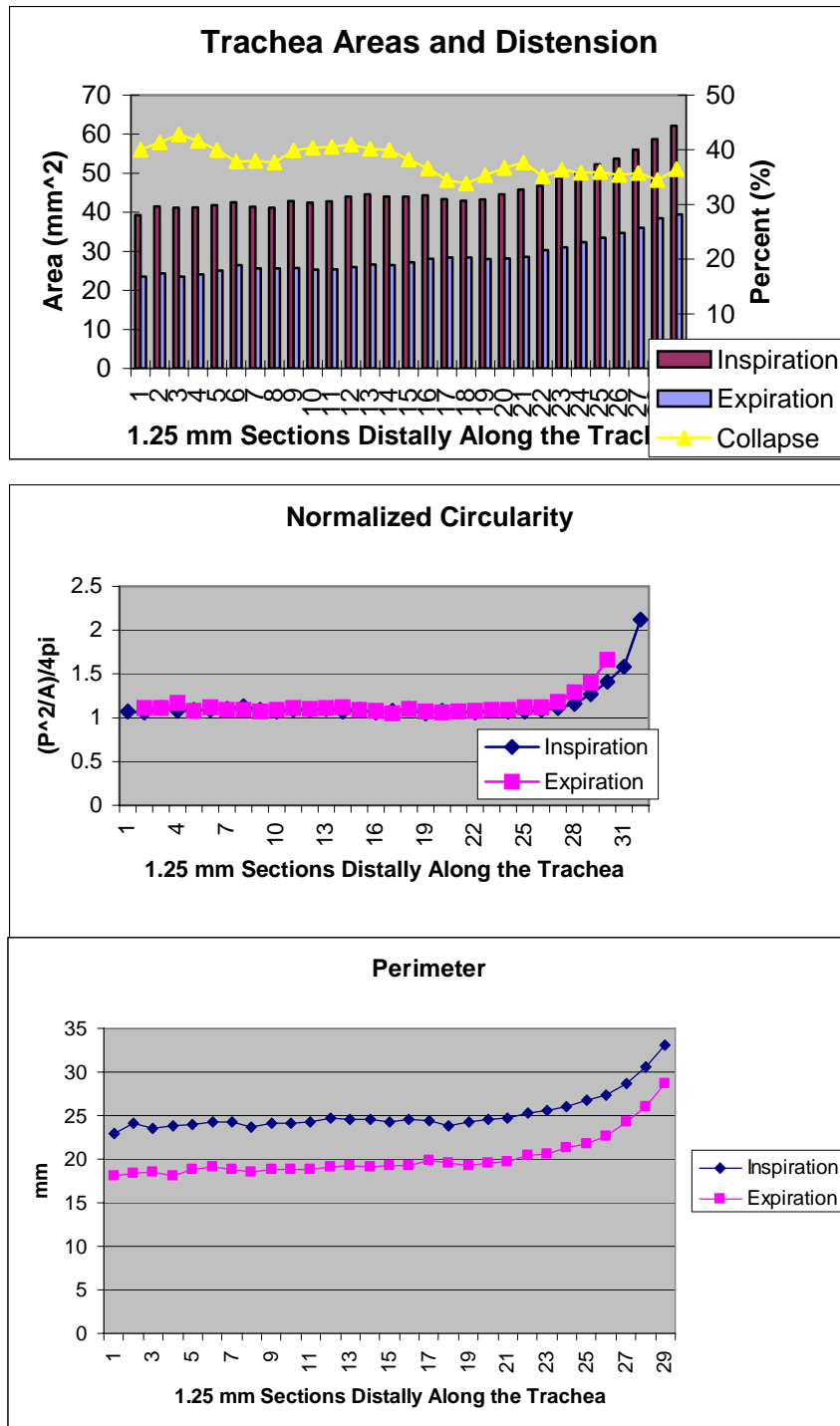


Figure 4.10: Quantitative analysis curves of a trachea in a patient with cystic fibrosis.

Figure 4.11: Quantitative analysis curves of the trachea using CVCT in a patient with innominate artery syndrome. In the area of the innominate artery (slices ~8-18) the trachea shows a localized region (~1.5 cm) of softening, though the geometry as indicated by circularity is relatively unchanged. There is also a corresponding widening of the space between the two perimeter curves. The right side of the curve represents the trachea transition into the bronchi (the carina) and the curves are less meaningful.

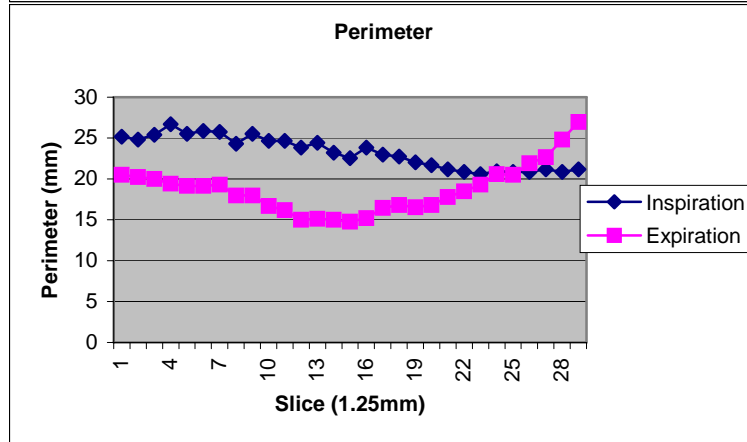
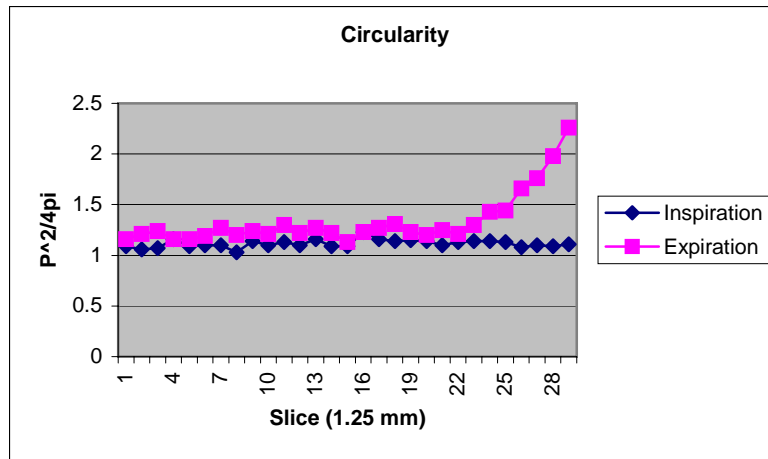
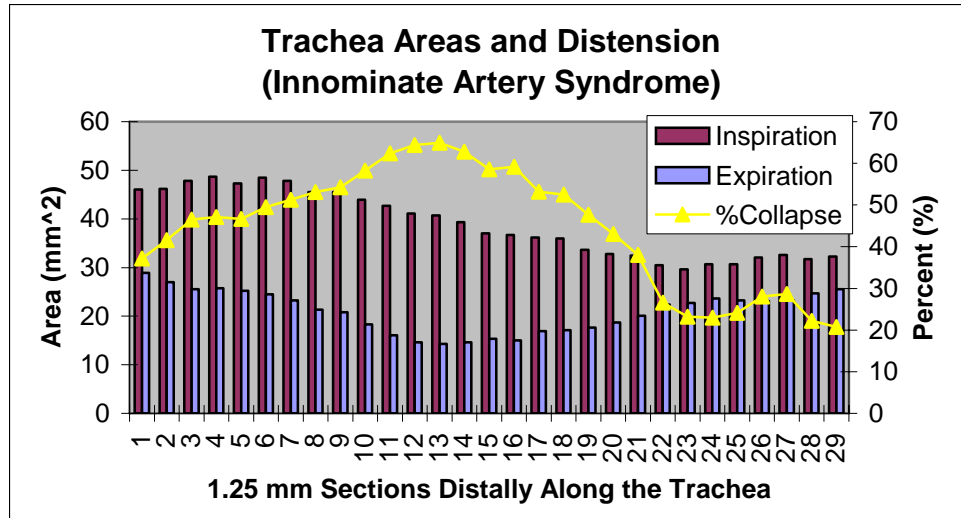


Figure 4.11: Quantitative analysis curves of the trachea using CVCT in a patient with innominate artery syndrome.

Figure 4.12: Quantitative analysis curves of the trachea using CVCT in a patient with a right-sided aortic arch. The elasticity of the trachea does not appear to be affected but in slices 12-15 a disruption of the normal relationship of circularity between inspiration and expiration is seen. This disruption is also noted for the perimeter curves in the same area as might be expected.

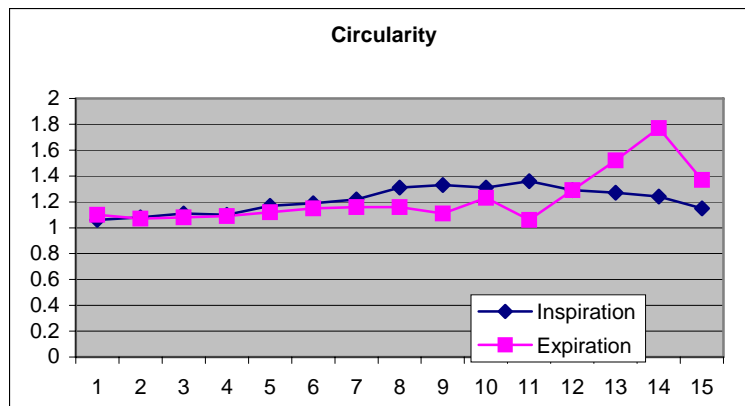
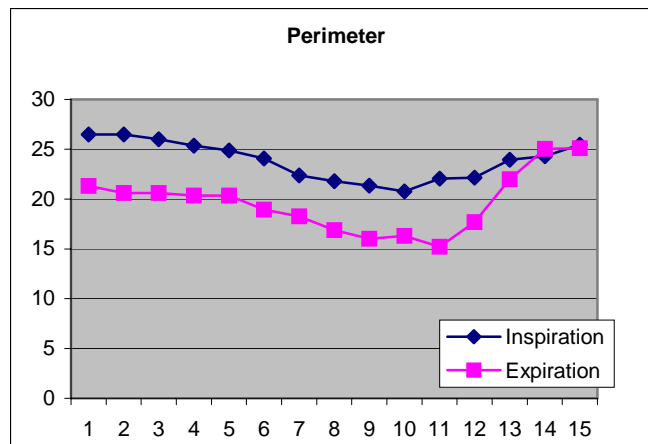
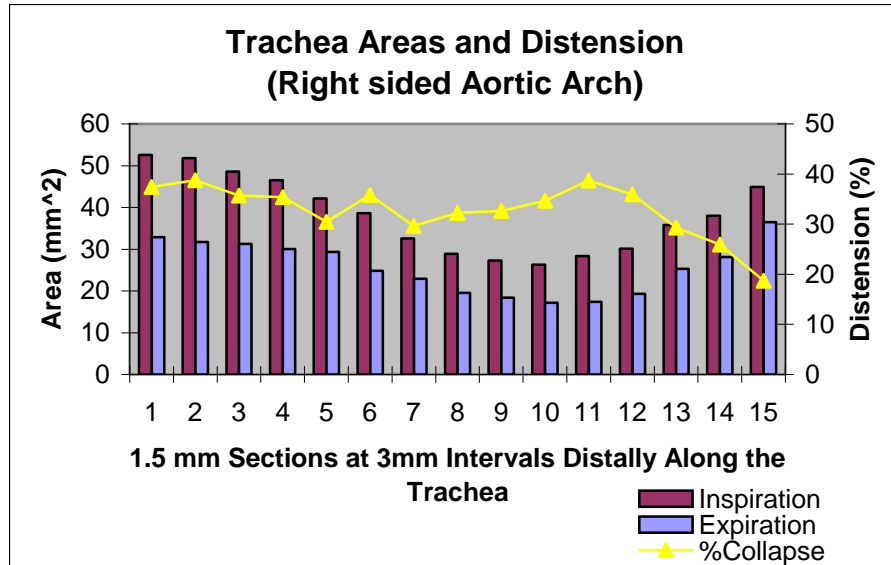


Figure 4.12: Quantitative analysis curves of the trachea using CVCT in a patient with a right-sided aortic arch

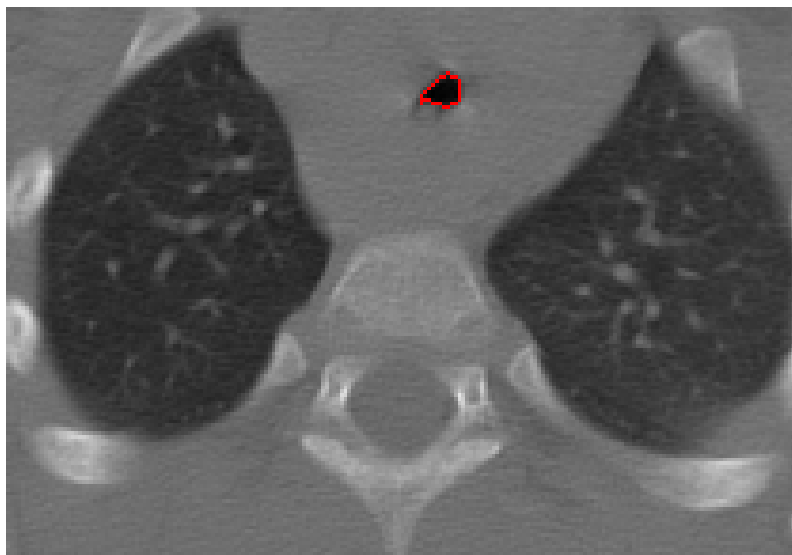


Figure 4.13: CVCT images of the patient with the right-sided aortic arch. (Above) Image at full inflation (25 cm H₂O mask pressure) with IV contrast. (Below) Image at expiration (0 cm H₂O). The red outlines the perimeter measurement generated during image analysis.

Figure 4.14: Quantitative analysis curves of the trachea using CVCT in a patient with focal tracheal stenosis. Note the decrease in distension in the area of stenosis (~ slices 9-17). Also note for this ~ 1cm region a characteristic lack of change in perimeter between the two measurements. The overall shape of the entire trachea is highly circular as evident from a circularity of close to unity throughout.

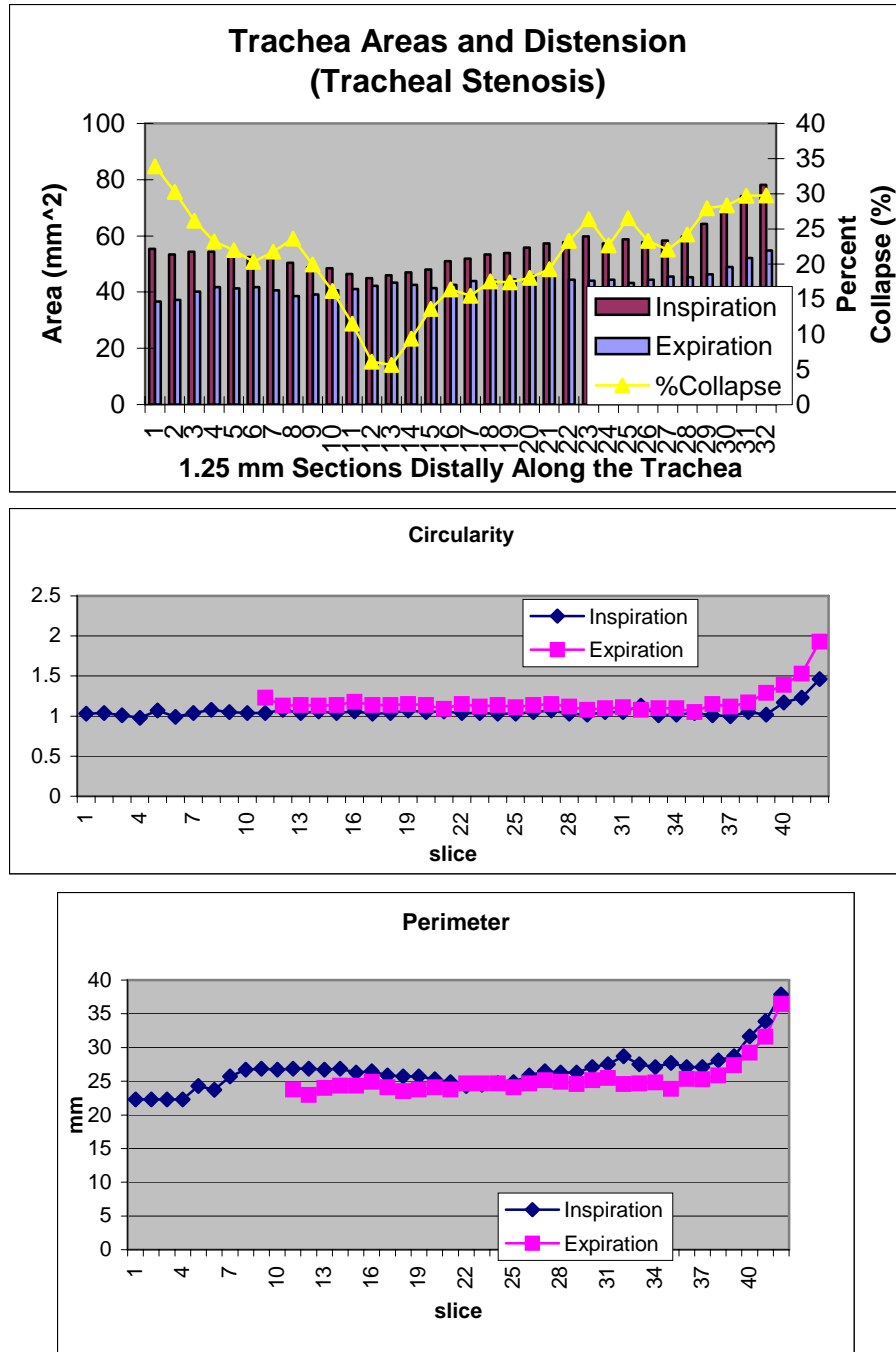


Figure 4.14: Quantitative analysis curves of the trachea using CV-CT in a patient with focal tracheal stenosis

Figure 4.15: Quantitative analysis curves of the trachea using CV-CT in a patient with diffuse tracheomalacia. The trachea distends well over 50% throughout, there is wide spacing between the two perimeter curves, and disruption of circularity especially on expiration.

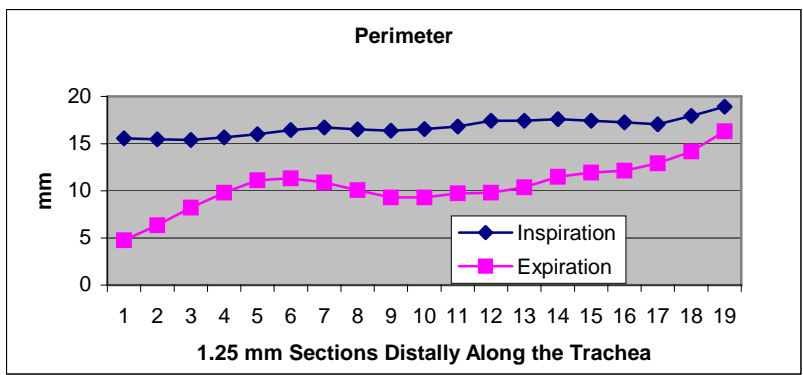
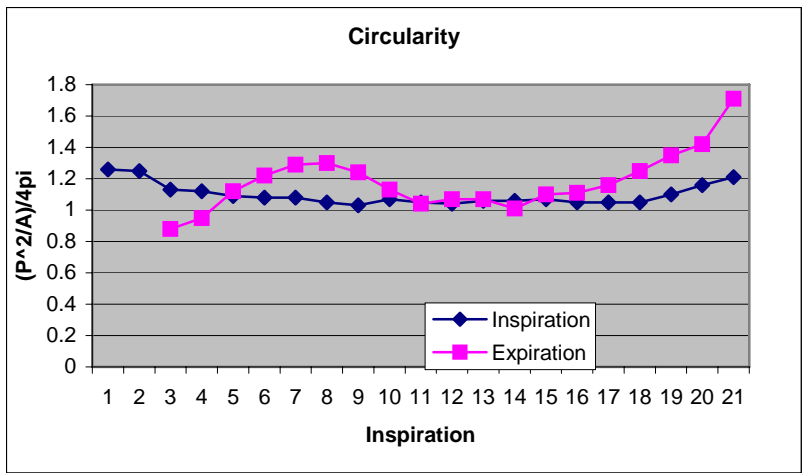
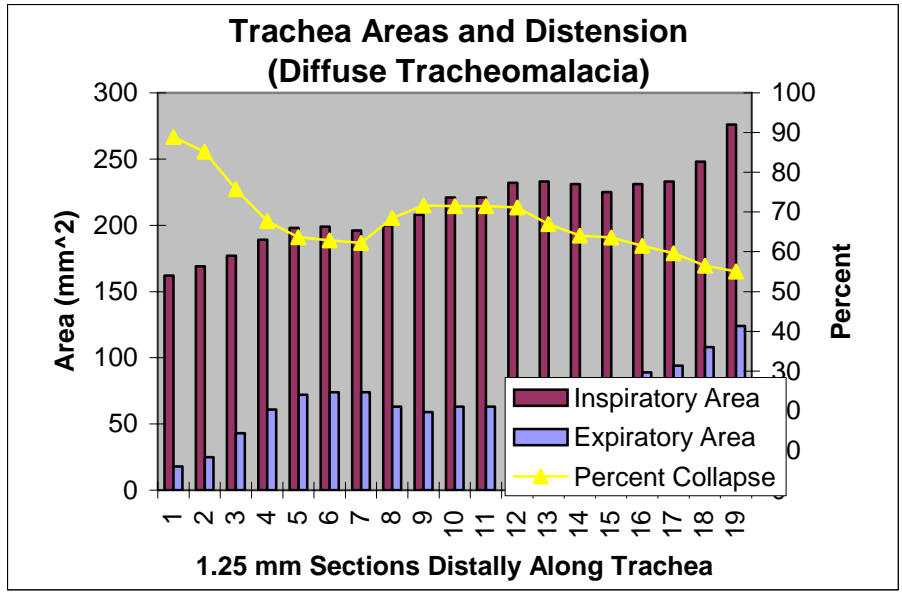


Figure 4.15: Quantitative analysis curves of the trachea using CV-CT in a patient with diffuse tracheomalacia.

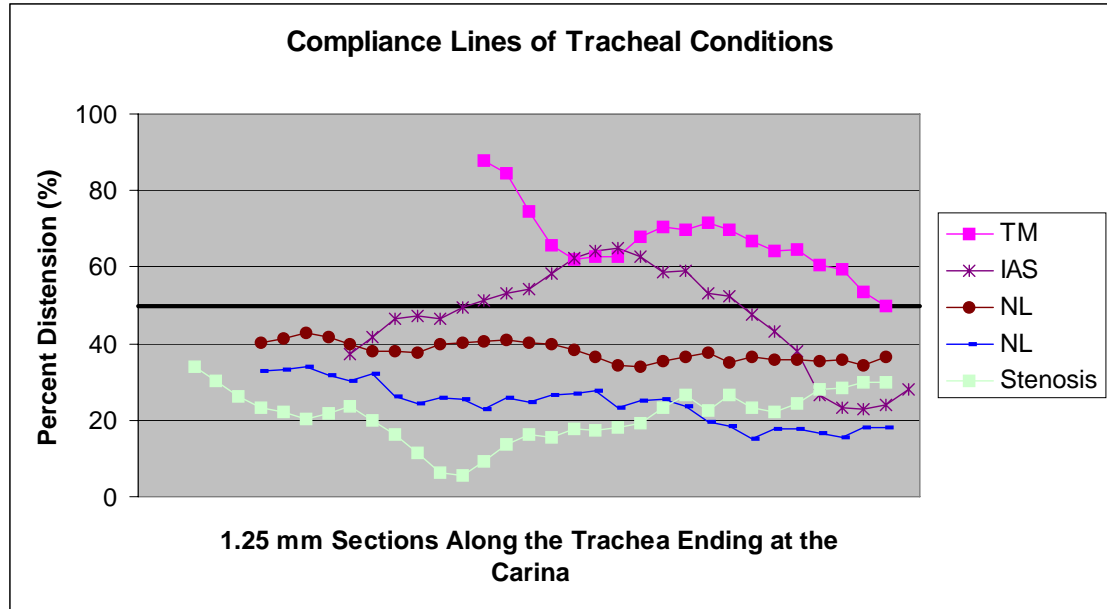


Figure 4.16: Compliance lines of the trachea comparing different conditions. The percent distension (approximating compliance) is defined as $((A_i - A_e)/A_i) \times 100\%$, where A_i is the area at full inflation (25 cm H₂O mask pressure) and A_e is the area at expiration (0 cm H₂O mask pressure). The bold line at 50% denotes the normal cutoff value. NL = normal, TM = tracheomalacia; IAS = innominate artery syndrome; stenosis = tracheal stenosis.

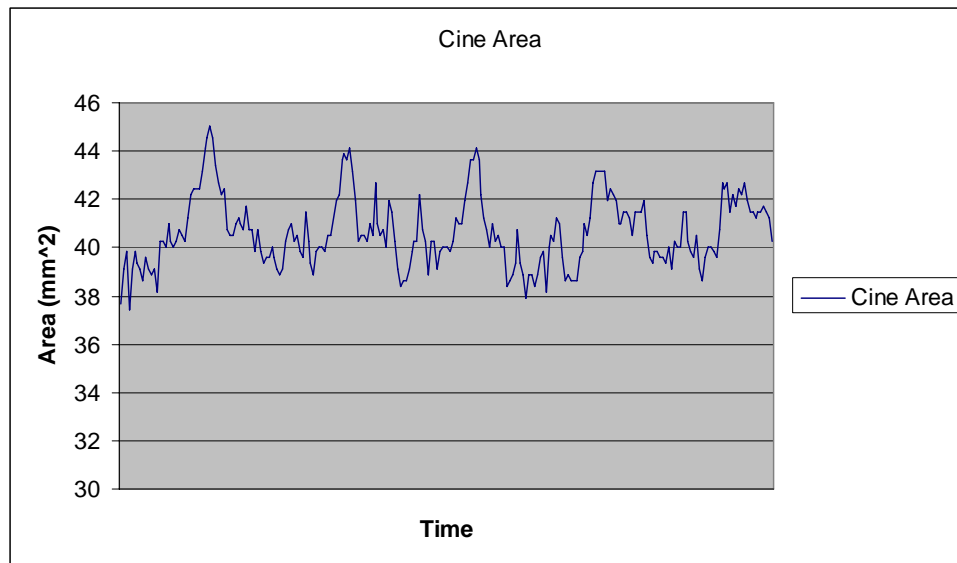


Figure 4.17: Analysis of the trachea using cine CT. The curve shows the trachea areas measured cross sections (shown above) taken at that level continuously during breathing. Using this technique the difference in the maximum and minimum areas (distension) is 17% for this specific anatomic level. With cine CT only the specified anatomic level is measured and subject to prolonged radiation dose.

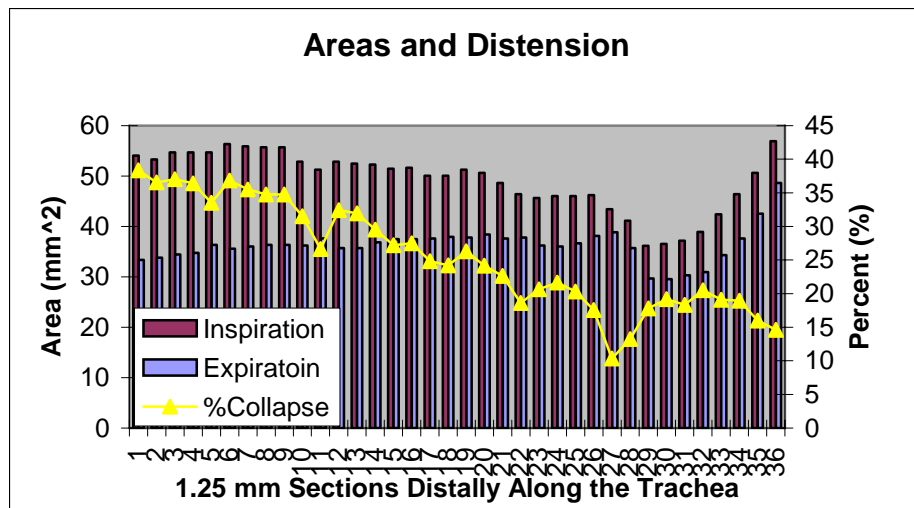
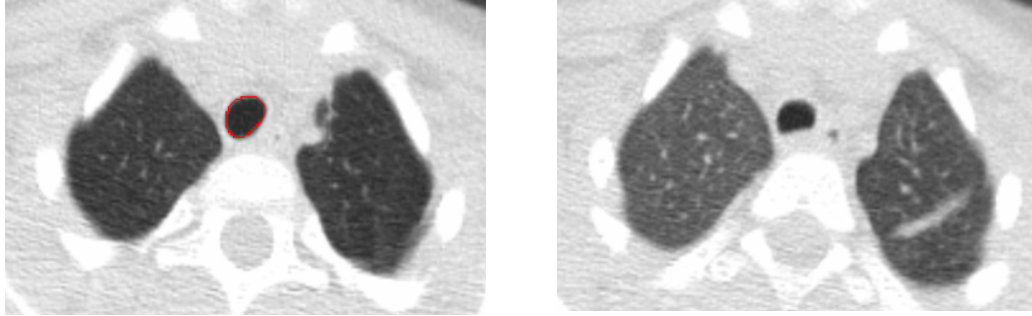


Figure 4.18: CVCT analysis of the matched level from figure 4.18. Using CVCT and quantitative image analysis the percent distension for the same anatomic level is 29% and the patient’s entire trachea can be analyzed.

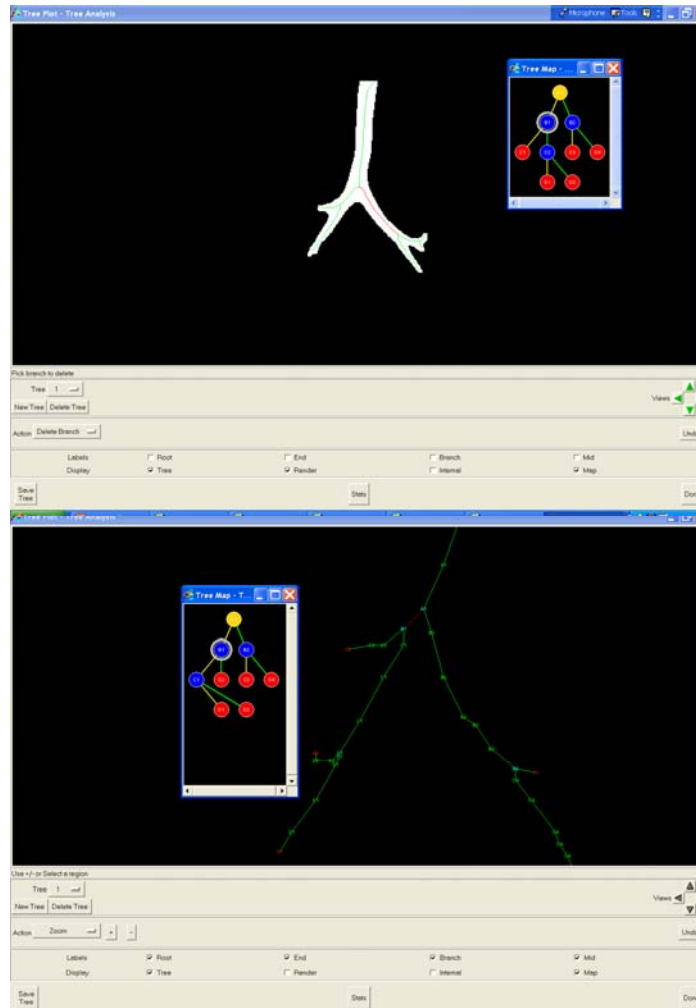


Figure 4.19: Extension of the CVCT technique to tracheobronchomalacia. Map of the airways in an infant using the Tree Analysis function generated with the Analyze™ software package. A map of the airways is generated including labels of each segment. Using this function an output of each branch segment areas and angle are mapped and can be exported for analysis. By comparing the maps of inspiration with expiration detailed maps of airway compliance can be generated.

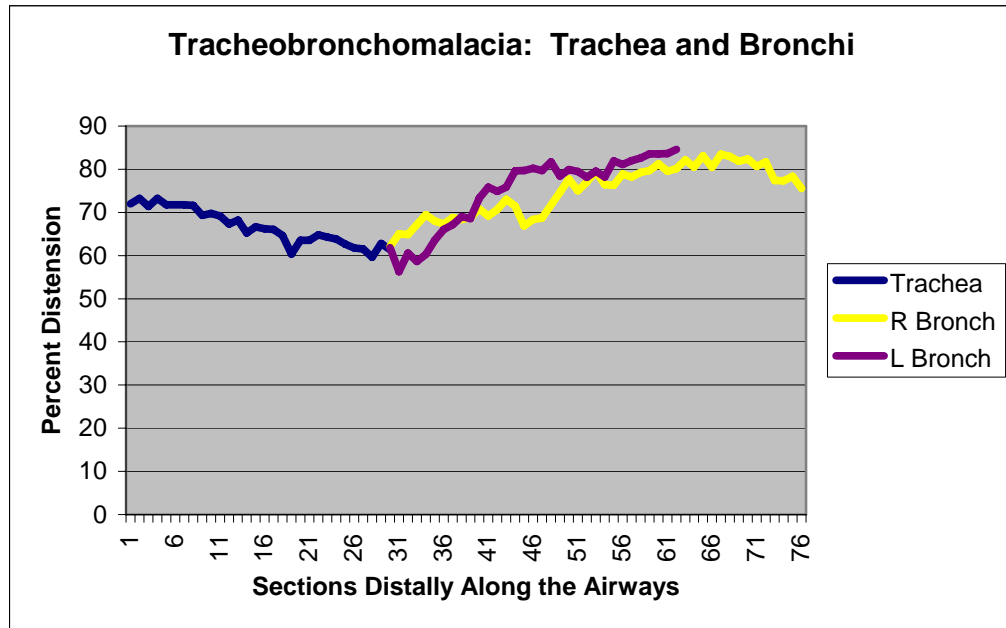


Figure 4.20: Graph showing airways distension in diffuse tracheobronchomalacia. This child had extensive disease as evidenced by the near complete collapse of both bronchi.

REFERENCES

1. Benjamin B. Tracheomalacia in infants and children. *Ann Otol Rhinol Laryngol* 1984; 93:438-42.
2. Jeffery HE, Rahilly P, Read DJ. Multiple causes of asphyxia in infants at high risk for sudden infant death. *Arch Dis Child* 1983; 58:92-100.
3. Austin J, Ali T. Tracheomalacia and bronchomalacia in children: pathophysiology, assessment, treatment and anaesthesia management. *Paediatr Anaesth* 2003; 13:3-11.
4. Mair EA, Parsons DS. Pediatric tracheobronchomalacia and major airway collapse. *Ann Otol Rhinol Laryngol* 1992; 101:300-9.
5. Gupta TG, Goldberg SJ, Lewis E, Fonkalsrud EW. Congenital bronchomalacia. *Am J Dis Child* 1968; 115:88-9.
6. Carden KA, Boiselle PM, Waltz DA, Ernst A. Tracheomalacia and tracheobronchomalacia in children and adults: an in-depth review. *Chest* 2005; 127:984-1005.
7. Wailoo MP, Emery JL. The trachea in children with tracheo-oesophageal fistula. *Histopathology* 1979; 3:329-38.
8. McNamara VM, Crabbe DC. Tracheomalacia. *Paediatr Respir Rev* 2004; 5:147-54.
9. Wittenborg MH, Gyepes MT, Crocker D. Tracheal dynamics in infants with respiratory distress, stridor, and collapsing trachea. *Radiology* 1967; 88:653-62.
10. Baxter JD, Dunbar JS. Tracheomalacia. *Ann Otol Rhinol Laryngol* 1963; 72:1013-23.
11. Griscom NT, Vawter GF, Stigol LC. Radiologic and pathologic abnormalities of the trachea in older patients with cystic fibrosis. *AJR Am J Roentgenol* 1987; 148:691-3.

12. Brooks LJ. Tracheal size and distensibility in patients with cystic fibrosis. *Am Rev Respir Dis* 1990; 141:513-6.
13. Lebecque P, Liistro G, Veriter C, Stanescu D. Tracheal distensibility in cystic fibrosis. *Eur Respir J* 1996; 9:770-2.
14. Castile R, Filbrun D, Flucke R, Franklin W, McCoy K. Adult-type pulmonary function tests in infants without respiratory disease. *Pediatr Pulmonol* 2000; 30:215-27.
15. Long FR, Castile RG. Technique and clinical applications of full-inflation and end-exhalation controlled-ventilation chest CT in infants and young children. *Pediatr Radiol* 2001; 31:413-22.
16. Muro S, Nakano Y, Sakai H, et al. Distorted trachea in patients with chronic obstructive pulmonary disease. *Respiration* 2000; 67:638-44.
17. Okazaki J, Isono S, Hasegawa H, Sakai M, Nagase Y, Nishino T. Quantitative assessment of tracheal collapsibility in infants with tracheomalacia. *Am J Respir Crit Care Med* 2004; 170:780-5. Epub 2004 Jul 8.
18. Walner DL, Ouanounou S, Donnelly LF, Cotton RT. Utility of radiographs in the evaluation of pediatric upper airway obstruction. *Ann Otol Rhinol Laryngol* 1999; 108:378-83.
19. Rudman DT, Elmaraghy CA, Shiels WE, Wiet GJ. The role of airway fluoroscopy in the evaluation of stridor in children. *Arch Otolaryngol Head Neck Surg* 2003; 129:305-9.
20. Newth CJ, Lipton MJ, Gould RG, Stretton M. Varying tracheal cross-sectional area during respiration in infants and children with suspected upper airway obstruction by computed cinetomography scanning. *Pediatr Pulmonol* 1990; 9:224-32.
21. Hein E, Rogalla P, Hentschel C, Taupitz M, Hamm B. Dynamic and quantitative assessment of tracheomalacia by electron beam tomography: correlation with clinical symptoms and bronchoscopy. *J Comput Assist Tomogr* 2000; 24:247-52.
22. Aquino SL, Shepard JA, Ginns LC, et al. Acquired tracheomalacia: detection by expiratory CT scan. *J Comput Assist Tomogr* 2001; 25:394-9.
23. Gilkeson RC, Ciancibello LM, Hejal RB, Montenegro HD, Lange P. Tracheobronchomalacia: dynamic airway evaluation with multidetector CT. *AJR Am J Roentgenol* 2001; 176:205-10.

24. Hasegawa I, Boiselle PM, Raptopoulos V, Hatabu H. Tracheomalacia incidentally detected on CT pulmonary angiography of patients with suspected pulmonary embolism. *AJR Am J Roentgenol* 2003; 181:1505-9.
25. Rozycki HJ, Van Houten ML, Elliott GR. Quantitative assessment of intrathoracic airway collapse in infants and children with tracheobronchomalacia. *Pediatr Pulmonol* 1996; 21:241-5.
26. Pedersen OF, Castile RG, Drazen JM, Ingram RH, Jr. Density dependence of maximum expiratory flow in the dog. *J Appl Physiol* 1982; 53:397-404.
27. Fayon M, Donato L, de Blic J, et al. French experience of silicone tracheobronchial stenting in children. *Pediatr Pulmonol* 2005; 39:21-7.
28. Callahan CW. Primary tracheomalacia and gastroesophageal reflux in infants with cough. *Clin Pediatr (Phila)* 1998; 37:725-31.
29. Malloy MH, MacDorman M. Changes in the classification of sudden unexpected infant deaths: United States, 1992-2001. *Pediatrics* 2005; 115:1247-53.
30. Prandota J. Possible pathomechanisms of sudden infant death syndrome: key role of chronic hypoxia, infection/inflammation states, cytokine irregularities, and metabolic trauma in genetically predisposed infants. *Am J Ther* 2004; 11:517-46.
31. Cummings KJ, Pendlebury JD, Jirik FR, Sherwood NM, Wilson RJ. A SIDS-like phenotype is associated with reduced respiratory chemoresponses in PACAP deficient neonatal mice. *Adv Exp Med Biol* 2004; 551:77-83.
32. Voss LJ, Bolton DP, Galland BC, Taylor BJ. Effects of Prior Hypoxia Exposure, Endotoxin and Sleep State on Arousal Ability to Airway Obstruction in Piglets: Implications for Sudden Infant Death Syndrome. *Biol Neonate* 2005; 88:145-155.
33. Beal SM, Blundell HK. Recurrence incidence of sudden infant death syndrome. *Arch Dis Child* 1988; 63:924-30.

CHAPTER 5

AIR TRAPPING AS EARLY INDICATOR OF OBSTRUCTIVE LUNG DISEASE IN INFANTS AND YOUNG CHILDREN WITH CYSTIC FIBROSIS: COMPARISON OF QUANTITATIVE THIN-SECTION CT AND PULMONARY FUNCTION TESTS

Overview

This section details efforts to quantify air trapping in using the controlled ventilation computed tomography technique and quantitative image analysis algorithms. Air trapping occurs in the lungs when there is impaired gas exchange and is a marker of disease. This study attempts to quantify the extent of the air trapping and correlate this to observed structural abnormalities as well as pulmonary function tests (PFTs). Frederick R. Long, M.D. was primary author with this author being second having performed the quantitative image analysis in the study.

ABSTRACT

Purpose: To assess quantitatively air trapping as an early indicator of obstructive pathology in the lungs of infants and young children with cystic fibrosis (CF) using thin-section CT.

Methods and Materials: Motion free inspiratory (insp, at full inflation) and expiratory (exp, at functional residual capacity) thin-section CT images of the lungs were obtained in 50 infants (mean age 2.3 ± 1.4 years) with CF at 4 matched levels using a non-invasive controlled ventilation technique. The percent exp visual air trapping (visual AT), the percent shift of exp pixels below -700 , -750 , -800 , -850 Hounsfield units (HU), the mean exp and mean (insp-exp) lung density were compared to percent bronchial abnormalities (wall thickening or bronchiectasis) and pulmonary function tests (PFTs). PFTs included mid-expiratory phase of forced exp flow ($FEF_{25-75\%}$) and ratio of residual volume to total lung capacity (RV/TLC).

Results: Visual AT (mean area involved = 17 %) was seen in 33 of 50 (66%) infants and occurred in 6/28 (21%) of children without bronchial abnormalities. Visual AT and percent pixels < -800 HU, respectively, had overall the highest correlations ($p < 0.001$) with bronchial abnormalities ($r = 0.71, 0.36$), $FEF_{25-75\%}$ ($r = 0.62, 0.53$), and RV/TLC ($r = 0.74, 0.61$). In 15 of 17 infants (88%) with no visual AT, PFTs were in the normal range and no bronchial abnormalities were seen.

Conclusion: Functionally significant air trapping can be quantified on expiratory thin-section CT using controlled ventilation and is a sensitive early indicator of obstructive lung disease in infants with CF.

INTRODUCTION

Inflammatory airway damage resulting in obstructive lung disease is now recognized as beginning early in life in the lungs of children with CF (1, 2). Because of this, there is increasing interest in applying high resolution or thin-section CT in the detection and follow-up of this early disease with the hope of arresting its progression (3, 4). PFTs are known to be relatively insensitive to detecting early or isolated disease (1).

There is little described regarding the nature and extent of obstructive pathology in infants and young children with CF (3). There is reason to believe that disease begins in the peripheral airways with the earliest manifestation at thin-section CT being air trapping, followed by visible airway wall thickening and bronchiectasis (1). As an indicator of early obstructive disease, air trapping has advantages over other CT signs such as airway wall thickening, which is difficult to define and measure (5), particularly in infants. In contrast, air trapping is easier to delineate and has been quantified using various methods in studies performed in adults (6).

The purpose of this study is to evaluate air trapping using thin-section CT as an indicator of early obstructive lung disease in infants and young children with subclinical CF. To do this, the extent of expiratory air trapping visible will be correlated with the extent of structural abnormalities as well as airflow limitation and gas trapping by pulmonary function tests (PFTs). A secondary aim will be to explore the feasibility of applying objective quantitative lung density analysis to the assessment of air trapping in infants.

MATERIALS AND METHODS:

Subjects

Thin-section CT studies were performed in 50 infants and young children with CF, who were undergoing sedation for “adult-type” infant pulmonary function testing (7) according to an institutional review board approved protocol. Informed consent was obtained from the parents prior to the study. As part of the research protocol, PFTs were performed routinely every six-months or following a two-week course of intravenous antibiotics given because of an exacerbation of respiratory symptoms. All children were considered to be clinically well at the time of testing.

Thin-section CT imaging

CT imaging was performed using the controlled-ventilation (CV) technique described by Long et al. (8). Because the CT and PFT studies require sedation (oral chloral hydrate, 50-100mg/kg, or intravenous Pentobarbital, 2-7mg/kg, Wyeth Laboratories), both studies were performed the same day so that the child only needed to be sedated once. While the child was sedated, oxygen saturation, heart rate, and respiratory rate were monitored continuously.

Controlled ventilation is a method of inducing transient apnea in a sedated child by augmenting normal spontaneous respiration with positive pressure applied via a facemask. In this study, a short series of augmented breaths were given timed to the child’s spontaneous breathing at a positive pressure of 25cm of water. This resulted in a transient period of hypocarbia-induced apnea, during which the CT images were

acquired. For inspiratory scanning at full inflation, positive pressure of 25cm of water was maintained during the respiratory pause and then released once the CT scan completed. At 25 cm of water pressure, the lungs are inflated to a volume near total lung capacity (9). For expiratory imaging, no mask pressure was applied after the series of positive pressure breaths. The lungs were thus imaged at resting end exhalation (the CT equivalent of functional residual capacity).

CT scans were acquired using a GE Hi Speed Advantage CT scanner (GE Medical Systems, Milwaukee, WI, USA). Thin-sections of 1mm slice thickness were obtained at 120 kvp, 80mA using a 1 second scan time, bone algorithm, 512x 512 matrix, and the smallest field of view possible, depending on the size of the child (13 -25cm). Inspiratory and expiratory thin-section CT images were acquired at the same four anatomic levels: 1) at the top of the aortic arch, 2) at the carina, 3) at the inferior edge of the right hilum, and 4) one to two centimeters above the top of the diaphragms.

Image analysis: visual assessment

All inspiratory images were enlarged (x2) and displayed at a window width of +1500 and window level of -600 Hounsfield units (HU) on a GE Medical Systems PACS workstation. Two experienced pediatric radiologists, who had no knowledge of the clinical or PFT findings, evaluated inspiratory images for the presence of a mosaic pattern of attenuation and bronchial abnormalities. Mosaic attenuation was defined as the presence of variable areas of abnormal low lung attenuation on inspiratory images. Bronchial abnormalities included wall thickening, which was subjectively determined,

and bronchiectasis, defined as the internal diameter of the bronchus greater than the accompanying pulmonary artery diameter, or lack of normal smooth tapering of the bronchial lumen. The number of normal and abnormal bronchi at each of the four levels was tabulated to derive the percent of bronchi with structural abnormalities, defined as the percentage of bronchi with either wall thickening or bronchiectasis.

All expiratory images were filmed on laser hard copy at a window width of +1500 and window level of - 450 HU. The reviewers outlined with a wax marker, by consensus, all areas of the lung involved by air trapping. Air trapping was defined as areas of abnormally low lung attenuation on expiratory images. If there were only a solitary focus of abnormal low attenuation that was the estimated size of a subsegment or sub-subsegment, the child was considered not to have air trapping.

Image analysis: quantitative lung density measurements

All inspiratory and expiratory images were downloaded in DICOM format into an image analysis program, Analyze 3.0 (Analyze, Direct. Mayo Clinic, MN). Each lung at each level was separated from the surrounding soft tissues and vessels using a thresholding technique (10, 11) to create object maps containing pixels in the range of -1000 to -200 HU. The program calculates the mean lung density and area for each object map and the percentage of pixels within selected density ranges. In this manner, we obtained the mean inspiratory (I), mean expiratory (E), and difference in mean inspiratory and expiratory (Δ I-E) lung density of all four levels for both right and left lungs. The areas of lung at

expiration involved by air trapping determined visually (visual AT) were quantified by recreating those areas on digital images using the analysis program. This was done by creating additional object maps corresponding to each air trapping area using a “seeding and density thresholding” technique so that the resulting individual air trapping object maps visually matched as best as possible the hard copy images. Similarly, pixel indexes, defined as the percentage of pixels on expiratory images less than a low-density index threshold were calculated by creating additional object maps of the whole lung that were limited by the chosen density threshold. We evaluated pixel index (PI) density thresholds (HU) of -700 (PI₋₇₀₀), -750 (PI₋₇₅₀), -800 (PI₋₈₀₀), and -850 (PI₋₈₅₀).

Pulmonary function tests:

Using the rapid chest compression method, maximum flow volume curves were obtained and the forced vital capacity (FVC), the forced expiratory volume at 0.5sec (FEV_{0.5}), and the forced expiratory flows between 25-75% of expired vital capacity (FEF_{25-75%}) were measured (7). Using whole body plethysmography, fractional lung volumes, including residual volume (RV), functional residual capacity (FRC), and total lung capacity (TLC) were obtained; the FRC/TLC and RV/TLC ratios were derived. PFTs are reported as percent predicted (7, 12).

Statistics

Descriptive statistics (mean, median, and standard deviation) were calculated for each of the variables. Relationships between the variables were assessed using Spearman's correlations (due to the skewness of some of the variables), and linear regression

modeling. Some the variables (bronchial abnormalities, mosaic attenuation, and expiratory air trapping) were categorized as present or absent. Average differences between the other continuous variables and the presence or absence of characteristics were assessed using non-parametric Wilcoxon Rank Sum tests. Relationships between the categorized variables were assessed using Chi-Square tests. For all of the analyses, statistical significance was assessed at the 0.05 level. The analyses were conducted using SAS Version 8.1 (SAS Institute Inc., Cary, NC, 2001).

Standardized z-scores [$z_x = (X - \mu_x) / \sigma_x$] were derived for FEF_{25-75%} and RV/TLC based on published normative data (7, 12). A z-score of 1 represents one standard deviation from the mean. We classified an observation as ‘normal’ if their standardized z- score was within ± 2 , and ‘abnormal’ if their standardized score was less than -2 or greater than $+2$.

RESULTS:

Twenty-two boys and 28 girls with CF were studied (mean age 2.3 ± 1.4 years, range 10 weeks to 5.5 years). On inspiratory images, a mosaic attenuation pattern was seen in 13/50 (26%), and bronchial abnormalities in 22/50 (44%) of children. In the 22 children with bronchial abnormalities, the (mean \pm s.d.) percent of bronchi that were abnormal was $21 \pm 16\%$, range 1-66%. All bronchial abnormalities that were identified were mild (bronchial wall thickness ranged from 1-2mm, and the bronchial lumen diameter was no greater than 1.5 times the accompanying vessel diameter), and could be categorized as increased wall thickness without bronchiectasis (29%), bronchiectasis without wall thickening (46%), and both bronchiectasis and wall thickening (25%).

On expiratory images, 33/50 (66%) of children had air trapping. In the 33 children with visual air trapping, the (mean \pm s.d.) percent area of the lung involved was $17 \pm 15\%$, range 1-66%. The associations between the presence and absence of expiratory air trapping, bronchial abnormalities, and a mosaic attenuation pattern are illustrated in Figure 1. There was good correlation between percent of bronchial abnormalities and percent of expiratory air trapping, $r = 0.71$, $p < 0.001$. When no expiratory air trapping was seen, only 1/17 (6%) children had a bronchial abnormality. Expiratory air trapping in the absence of bronchial abnormalities was more frequent and occurred in 6/28 (21%) children. Although all children with a mosaic attenuation pattern at inspiration had expiratory air trapping, 20/37 (54%) of children without a mosaic attenuation pattern also had expiratory air trapping.

Quantitative thin-section CT density measures

The overall (n=50) mean (\pm s.d.) inspiratory lung density (HU) was -785 ± 37 ; expiratory lung density, -605 ± 55 ; and Δ (I-E) lung density, 180 ± 45 . The mean (\pm s.d.) percentage of pixels below density thresholds (HU) of -700 was $26 \pm 17\%$; -750 , $13 \pm 12\%$; -800 ; $5.5 \pm 6.4\%$, and -850 , $1.7 \pm 2.5\%$. The mean expiratory density correlated highly with the pixel indexes ($r = 0.86$ to 0.98).

The correlations between visual air trapping and quantitative density measures were all significant ($p < 0.001$). For visual AT and pixel indexes, correlation coefficients (PI $_{-700}$, $_{-750}$, $_{-800}$, and $_{-850}$) were 0.52 , 0.61 , 0.70 , and 0.73 , respectively. The correlations with visual AT were less for mean expiratory density ($r = -0.48$), and mean Δ (I-E) density, ($r = 0.49$). The correlations between percent bronchial abnormalities and visual AT was 0.72 (bronchial wall thickening 0.60 ; and bronchiectasis, 0.50). The correlations between percent bronchial abnormalities and quantitative density measures were significant only for PI $_{-750}$ ($r = 0.30$), PI $_{-800}$ ($r = 0.36$), and PI $_{-850}$ ($r = 0.38$).

Comparisons with PFTs

Visual AT correlated best with FEF $_{25-75\%}$ and RV/TLC. The strength of visual and quantitative thin-section CT - PFT correlations are represented by Spearman's correlation coefficients and shown in table 1 for both spirometry measures and fractional lung volumes. There was no significant effect when results were adjusted for differences in height and age. The relationship of visual AT with FEF $_{25-75\%}$ and RV/TLC, represented as z-scores, is graphically depicted in Figure 2 and 3. The association of degree of visual

expiratory air trapping with bronchial abnormalities, mosaic attenuation pattern, and FEF_{25-75%} and RV/TLC is shown in Table 2. Although visual AT had the highest correlation coefficients with FEF_{25-75%} and RV/TLC, there was no significant difference when compared with PI₋₈₀₀ ($p > 0.38$) and PI₋₈₅₀ ($p > 0.33$). The relationship of PI₋₈₀₀ to residual volume (RV) is shown in Fig 4.

The presence of mosaic attenuation on inspiratory thin-section CT correlated significantly with PFT and other thin-section CT measures (FEF_{25-75%}, $p < 0.001$, RV/TLC, $p < 0.001$, visual AT%, $p < 0.001$, %bronchial abnormalities, $p < 0.001$, and PI₋₈₅₀, $p < 0.004$).

DISCUSSION:

The results of this study indicate that air trapping is the most frequent finding of obstructive lung disease in infants with CF using thin-section CT. The air trapping seen appears to be significant as it is highly correlated with bronchial abnormalities and PFT measures of both gas trapping and airflow limitation. The fact that air trapping was almost always associated with bronchial abnormalities and occurred in 28% of children without bronchial abnormalities supports the hypothesis that air trapping is the earliest manifestation of obstructive lung disease in infants by CT. In addition, the absence of air trapping was highly predictive of normal bronchial morphology on thin-section CT and normal pulmonary function tests.

In infants, a mosaic pattern of attenuation at inspiration is not a useful CT sign because the absence of a mosaic pattern at inspiration was not a good predictor for the absence of expiratory air trapping. Visual AT was seen in 24/37 (54%) of children without a mosaic attenuation pattern (see figure 1).

We evaluated the feasibility of using in infants various quantitative CT lung density measurements to estimate air trapping that have been described in the adult literature, which includes expiratory mean lung density, the difference in mean lung density between inspiration and expiration (13, 14) and the expiratory “pixel index” (15). Air trapping results in a negative or leftward shift in the distribution of lung densities and thus a higher percentage of pixels below the threshold. The pixel index should increase

directly with residual volume, and this was observed in our study ($r=0.50$, $p < .001$ for PI_{-800}).

The feasibility of using quantitative density measurements to estimate air trapping in infants is supported by the good correlation between visual expiratory AT and the various quantitative CT lung density measures as well as the excellent correlation between both visual and quantitative thin-section CT measures and PFT measurements of airflow limitation and gas trapping. The quantitative measures most highly correlated with visual AT and PFTs were PI_{-800} and PI_{-850} . Although visual AT had the highest overall correlation coefficients with PFTs, it was not significantly better than PI of -800 and -850. We evaluated a range of pixel indexes from -700 to -850 HU due to the higher lung densities in children compared to adults and because lung densities change in infants and young children due to rapid lung growth. Our results indicate that pixel indexes of -800 and -850 represent the lowest 2 and 5%, respectively, of expiratory lung densities in the 0-5-year age group, which corresponds to the pixel index threshold of -900 HU that has been used in adults to assess air trapping (15) and emphysema (16).

The mean expiratory and $\Delta(I-E)$ lung density correlations with PFTs were also significant but the correlation coefficients were not as good as the pixel indexes. This is not surprising as a leftward shift in pixel density distribution would likely result in less of a change in the mean density than in the percent of pixels below an air trapping threshold density. Expiratory mean density correlated slightly better with air trapping measured by residual volume, whereas $\Delta(I-E)$ mean correlated slightly better with expiratory flows,

FEF_{25-75%}, which would be expected as $\Delta(I-E)$ density is more directly related to airflow.

In a study of mean expiratory and $\Delta(I-E)$ lung densities correlated with FEF_{50%} in adults, only the $\Delta(I-E)$ lung density differentiated subjects with minimal small airways disease from normal controls (13).

The value of quantitative lung density measures would be expected to improve once normative lung density data for full inflation and resting end exhalation lung volumes becomes available. Expiratory and I-E mean density measurements could then be expressed as percent predicted values and pixel indexes could be further tailored to specific ages.

Our results comparing visual AT and pixel indexes with PFTs are similar to the results reported in studies done in older children and adults. In a study of a combined group of healthy adult volunteers and patients with obstructive lung disease, (14)the visual air trapping score correlated strongly with FEV₁ and FEF_{25-75%} ($r= 0.89$ and 0.81 , respectively). These results are comparable to our correlations with FEV_{0.5} of 0.60 and FEF_{25-75%} of 0.62 in a young population with mild disease. The PI₋₈₀₀ correlations we found with FEV_{0.5} ($r= -0.60$) and RV($r= .50$) were similar to the correlations reported with FEV_{1.0} ($r= -0.62$) and RV ($r= 0.63$) in a study of “clinically well” adult asthmatics in which a pixel index of -900 HU was used (15).

There are differences in our study compared to those done in adults that should be discussed. We use controlled ventilation to obtain inspiratory and expiratory thin-section

CT images, which is comparable but not identical to inspiratory and expiratory voluntary breath holding. CV-thin-section CT is a non-invasive technique in that it does not require anesthesia and endotracheal intubation. The images are acquired without respiratory motion and at controlled physiological pressures. A positive pressure of 25 cm water applied to inflate the lungs to near total lung capacity, and expiratory scans are obtained at resting end exhalation or FRC. As the same pressures are applied in each case, the results are reproducible (17). We do not believe that differences between controlled ventilation and voluntary breath holding are significant for air trapping evaluation, which is supported by the similar correlation coefficients between the adult studies and our infant group.

The greater sensitivity of CT in comparison to PFTs in the evaluation of air trapping is suggested by the plots of visual AT versus standardized z-scores for PFTs. When visual AT is less than 20%, RV/TLC ratio z-scores remain within the normal range and FEF_{25-75%} z-scores are mixed between normal and abnormal. When visual AT exceeds 20% of the lung, both PFT measures become consistently abnormal. Air trapping in the range of 0-20% appears to be significant, as it is associated with bronchial abnormalities (see Table 2).

The role of thin-section CT at full inflation and resting end exhalation lung volumes in the management of infants with cystic fibrosis is yet to be determined but offers great promise. The high sensitivity of controlled ventilation thin-section CT suggests that it is an ideal tool to detect the earliest obstructive pathology and thus guide developing

treatment interventions to prevent progressive, irreversible disease. The advantages of CT over PFTs are its greater sensitivity to detecting early pathology and its greater availability and ease of use. Pulmonary function testing in infants requires specialized equipment that is currently available in only a few medical centers. A potential disadvantage of CT compared to PFTs is radiation exposure.

Due to the importance of keeping radiation exposure to the lowest levels possible, particularly in infants, the possibility of screening initially with a limited number of expiratory thin-section CT images, which this study suggests, is an attractive option to investigate. In this young age group, the absence of air trapping on expiratory images is highly predictive of normal bronchial morphology and PFTs, and thus an additional series of inspiratory image could be avoided. Inspiratory images could always be obtained if abnormalities were seen, or could be obtained at fixed intervals to assess for developing irreversible structural changes such as bronchiectasis.

An attractive feature of expiratory imaging as a screening tool is that expiratory air trapping can be objectively quantified. The use of objective measures such as pixel indexes should enhance reproducibility and make the technique more widely useable in the absence of expert readers. In addition, it is conceivable that with faster CT scanning techniques, adequate expiratory images could be obtained without sedation and controlled ventilation. It should be kept in mind however that radiation dose may need to be adjusted to compensate for the presence of respiratory motion. In a study by Lucaya et al (18), radiation exposures of less than 50mAs were diagnostically acceptable only for

thin-section images without respiratory motion. In addition, the effect of respiratory motion and low doses on quantitative CT lung density analysis is unknown and will need to be investigated.

In conclusion, expiratory thin-section CT using controlled-ventilation technique is an accurate and potentially low dose way of evaluating and quantifying air trapping in the lungs of infants and young children with CF. As air trapping is an early indicator of obstructive airway disease in these children, expiratory CT imaging shows promise as a screening tool.

	<u>Spirometry measures</u>			<u>Fractional lung volumes</u>		
	FVC	FEV 0.5	FEF _{25-75%}	RV	FRC	RV/TLC
<u>Visual CT</u>						
%Air trapping	-0.48	-0.60	-0.62	0.68	0.45	0.74
%Bronchial abnormalities	-0.19**	-0.32*	-0.35*	0.54	0.40	0.49
<u>Quantitative CT</u>						
pixel index -700	-0.42*	-0.52	-0.51	0.44	0.51	0.53
pixel index -750	-0.46	-0.56	-0.53	0.46	0.53	0.56
pixel index -800	-0.52	-0.60	-0.53	0.50	0.57	0.61
pixel index -850	-0.56	-0.60	-0.50	0.48	0.53	0.61
Expiratory (E)						
mean	0.42*	0.49	0.47	-0.46	-0.55	-0.54
Δ (I -E) mean	-0.26**	-0.41*	-0.50	0.40*	0.39*	0.43

Table 5.1 CT correlations with Pulmonary function tests. Values are Spearman's correlation coefficients. All correlations are significant to $p < 0.001$ (except ** = not significant; * = $p < 0.004$). Pixel index represent percent pixels less than given lung density threshold in Hounsfield units (HU).

	Number	Bronchi Abnormal	Mosaic Pattern	Abnormal FEF _{25-75%}	Abnormal RV/TLC
Visual AT% = 0	17	1/17 (6%)	0 (0%)	0 (0%)	2/17 (11%)
Visual AT% <20	22	18/22 (82%)	4/22 (18%)	6/22 (27%)	3/22 (14%)
Visual AT% >20	11	9/11 (82%)	9/11 (82%)	10/11 (90%)	5/11 (45%)

Table 5.2: Correlation of degree of visual air trapping with abnormal CT findings and PFT measures Visual AT = visual air trapping on expiratory images.

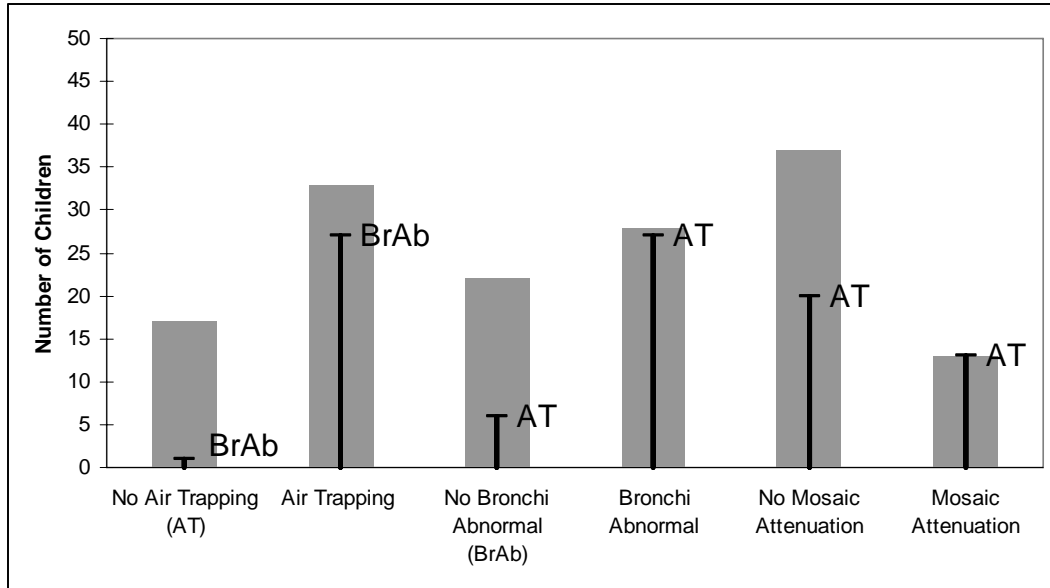


Figure 5.1: Bar graphs showing the associations of air trapping with bronchial abnormalities and mosaic attenuation pattern. The number of children in each category (gray bars) is shown along with the number with the associated abnormality (black bars). BrAb = bronchial abnormality, AT = air trapping.

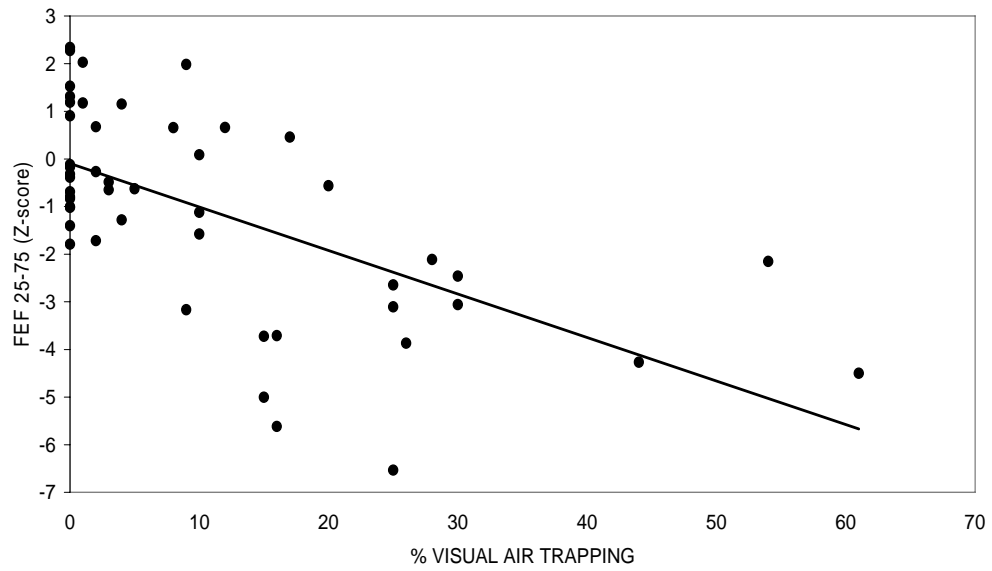


Figure 5.2: Scatterplot shows correlation of FEF_{25-75%} values reported as z-scores and percent visual air trapping with linear correlation ($r = 0.62$)

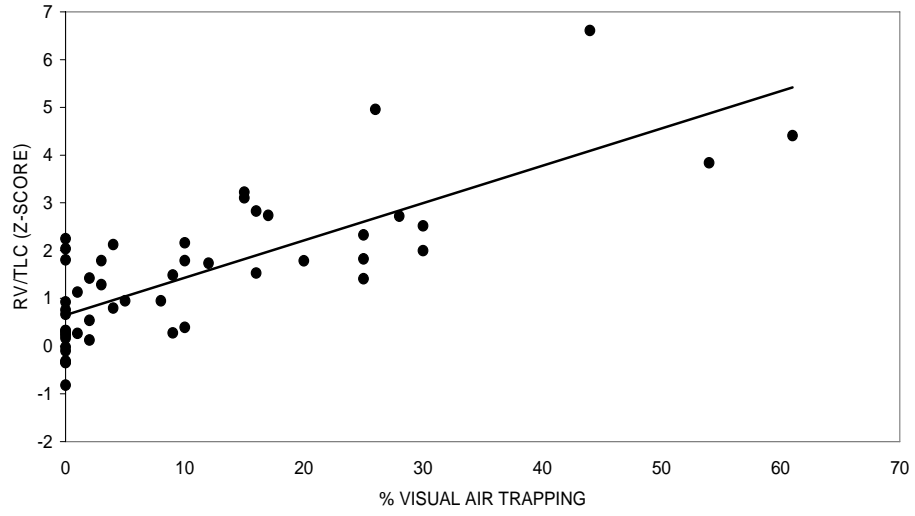


Figure 5.3: Scatterplot shows correlation of RV/TLC values reported as z-scores and percent visual air trapping with linear correlation ($r = 0.74$).

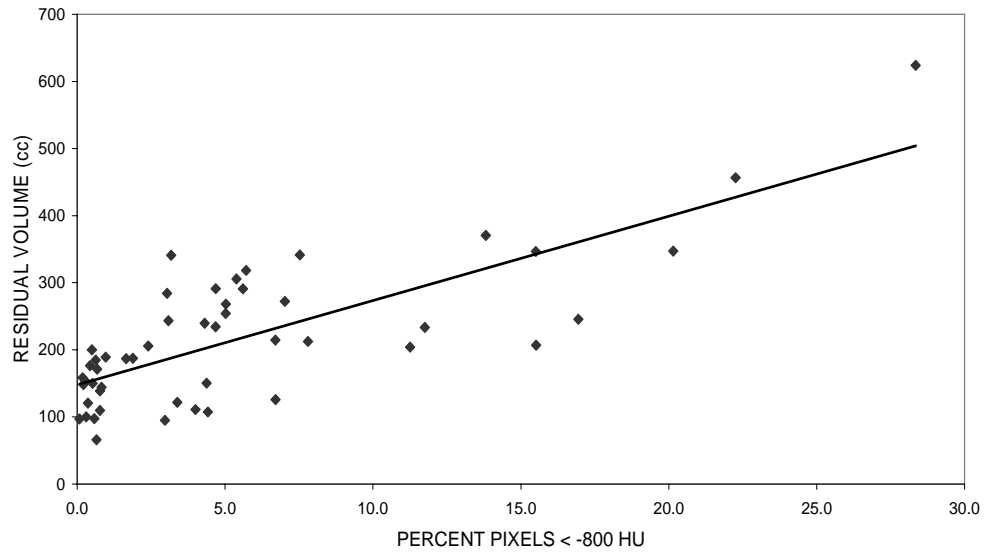


Figure 5.4: Scatter plot shows correlation of the percent pixels less than -800HU and the residual volume with linear correlation ($r= 0.50$).

REFERENCES

1. Tiddens HA. Detecting early structural lung damage in cystic fibrosis. *Pediatr Pulmonol* 2002;34:228-31.
2. Koch C. Early infection and progression of cystic fibrosis lung disease. *Pediatr Pulmonol* 2002;34:232-6.
3. Marchant JM, Masel JP, Dickinson FL, Masters IB, Chang AB. Application of chest high-resolution computer tomography in young children with cystic fibrosis. *Pediatr Pulmonol* 2001;31:24-29.
4. Nasr SZ, Kuhns LR, Brown RW, Hurwitz ME, Sanders GM, Strouse PJ. Use of computerized tomography and chest x-rays in evaluating efficacy of aerosolized recombinant human DNase in cystic fibrosis patients younger than age 5 years: a preliminary study. *Pediatr Pulmonol* 2001;31:377-382.
5. King GG, Muller NL, Pare PD. Evaluation of airways in obstructive pulmonary disease using high-resolution computed tomography. *Am J Resp Crit Care Med* 1999;159:992-1004.
6. Arakawa H, Webb WR. Expiratory high-resolution CT scan. *Radiol Clin North Am* 1998;36:189-209.
7. Castile R, Filbrun D, Flucke R, Franklin W, McCoy K. Adult-type pulmonary function tests in infants without respiratory disease. *Pediatr Pulmonol* 2000;30:215-227.
8. Long FR, Castile RG, Brody AS, Hogan MJ, Flucke RL, Filbrun DA, et al. Lungs in infants and young children: improved thin-section CT with a noninvasive controlled-ventilation technique--initial experience. *Radiology* 1999;212:588-93.
9. Turner JM, Mead J, Wohl ME. Elasticity of human lungs in relation to age. *J Appl Physiol* 1968;25:664-671.
10. Kauczor HU, Heussel CP, Fischer B, Klamm R, Mildemberger P, Thelen M. Assessment of lung volumes using helical CT at inspiration and expiration: comparison with pulmonary function tests. *Am J Roentgenol* 1998;171:1091-1095.

11. Rienmuller RK, Behr J, Kalender WA, Schatzl M, Altmann I, Merin M, et al. Standardized quantitative high resolution CT in lung diseases. *J Comput Assist Tomogr* 1991;15:742-9.
12. Jones M, Castile R, Davis S, Kisling J, Filbrun D, Flucke R, et al. Forced expiratory flows and volumes in infants. Normative data and lung growth. *Am J Respir Crit Care Med* 2000;161:353-9.
13. Tanaka N, Matsumoto T, Suda H, Miura G, Matsunaga N. Paired inspiratory-expiratory thin-section CT findings in patients with small airway disease. *Eur Radiol* 2001;11:393-401.
14. Chen D, Webb WR, Storto ML, Lee KN. Assessment of air trapping using postexpiratory high-resolution computed tomography. *J Thorac Imaging* 1998;13:135-143.
15. Newman KB, Lynch DA, Newman LS, Ellegood D, Newell JD, Jr. Quantitative computed tomography detects air trapping due to asthma. *Chest* 1994;106:105-109.
16. Arakawa A, Yamashita Y, Nakayama Y, Kadota M, Korogi H, Kawano O, et al. Assessment of lung volumes in pulmonary emphysema using multidetector helical CT: comparison with pulmonary function tests. *Comput Med Imaging Graph* 2001;25:399-404.
17. Long FR, Castile RG. Technique and clinical applications of full-inflation and end- exhalation controlled-ventilation chest CT in infants and young children. *Pediatr Radiol* 2001;31:413-422.
18. Lucaya J, Piqueras J, Garcia-Pena P, Enriquez G, Garcia-Macias M, Sotil J. Low-dose high-resolution CT of the chest in children and young adults: dose, cooperation, artifact incidence, and image quality. *Am J Roentgenol* 2000;175:985-992.

CHAPTER 6

SITE SPECIFIC INDUCTION OF LYMPHATIC MALFORMATIONS IN A RAT MODEL FOR LYMPHANGIOGENESIS AND IMAGE-GUIDED THERAPY

ABSTRACT

Introduction Lymphangiogenesis plays an important role in the development and metastatic spread of numerous cancers. Lymphatic malformation directly causes lymphangiomas, a common benign tumor in children. These tumors have high recurrence rates and frequent complications with surgery. Several sclerotherapy regimens have been developed clinically to treat lymphatic malformations, but no animal model has been developed that is adequate for study of image-guided intervention in lymphangiogenesis. *Methods* Male Harlan Sprague-Dawley rats (n=9) were injected under ultrasound (US) guidance with Incomplete Freund's Adjuvant (IFA) [85% Paraffin Oil and 15% Mannide Monooleate by volume] into the peritoneum (IP) twice, two-weeks apart. Three of these animals received additional US-guided injections of IFA into the neck. A control group (n=3) received IP injections of saline. Animals were monitored by US at two-week intervals for 100 days for the development of masses. Animals were then sacrificed and tissue specimens were fixed, sectioned, and stained with H&E and

CD31, an endothelial cell marker, and anti-sm1 for smooth muscle actin. Further immunohistochemical staining specific for lymphatic endothelium was conducted using flt-4 (VEGF-3R) and prox-1. *Results* Animals developed both microcystic and macrocystic masses by injection of IFA. Macrocystic malformations (~8 mm) were visible in the neck by ultrasound and grossly at necropsy. The 3 animals with two injection sites had both microcystic and macrocystic malformations. H&E stained sections showed cystic spaces surrounded by endothelium that were positive for CD31 stain. The 3 animals with two injection sites had both microcystic and macrocystic malformations. *Conclusion* This model represents a promising tool for the translational development of image-guided interventions for micro/macrocytic lymphangiomas. Additionally, this model may provide a means for the basic study of lymphangiogenesis and development anti-lymphangiogenic therapies.

Introduction

Lymphatic malformations (LMs) are common vascular malformations in infants and children accounting for about 5% of all benign tumors(1). Approximately 75% of LMs present in the face or neck causing significant cosmetic disfigurement(2). More than half are recognized at birth and 90% before 2 years of age(3, 4).

The cause of LMs remains unclear but it is thought to be attributable to a congenital failure of the lymphatics to connect with the venous system, abnormal budding of lymphatic structures, and/or abnormal appropriation of lymphatic tissue during embryonic development(4). Histologically, LMs consist of multiple dilated locules or sacs, lined with a single layer of endothelium supported by connective tissue stroma, and containing proteinaceous fluid (3, 4). Lesions can be classified as macrocystic (locules $> 2 \text{ cm}^3$), microcystic (locules $< 2 \text{ cm}^3$), or mixed. LMs generally present as slow-growing non-tender masses that are soft on palpation. Infection or trauma can cause pain in the tumors and induce swelling leading to complications including difficulty feeding or respiratory compromise by impingement of the airway.

Until recently, surgery had been the preferred method of treatment for LMs. However, complete removal of the tumors by surgery is often impossible given the involvement of vital nerves and vessels in the region of the tumor. The tumors have a high recurrence rate as well, especially if not completely removed ($>50\%$)(1). Significant complications including nerve paralysis associated with surgery are well-documented (10-33%) (4) and recurrence rates are high, in some studies greater than 50% (1).

Percutaneous treatment of the LMs is now generally the preferred method of treatment for LMs(5). Sclerotherapy has been employed for LMs with improved but varying degrees of success. Several studies in the literature report successful treatment of macrocystic lesions using a number of agents. There are numerous reports of varying success using multiple different sclerosing agents including OK-432, sodium tetradecyl sulfate, bleomycin sulfate, tetracycline, doxycycline, interferon alfa-2a and others. Ethibloc™, an ethanol/corn protein mixture, has been used as well with considerable success(6). These therapies have been tried both with and without aspiration of the cysts with mixed results. Others used fibrin glues (Tissucol™) to seal the tumors shut after aspiration(7). Macrocystic LMs treated with OK-432 (a lyophilized group A *Streptococcus pyogenes* protein) has shown “good” response following intralesional injection into LMs.(8-10). Most of these studies report a good response as one that results in >60% reduction in size of the tumor. Complete reduction of the LMs is achieved only about half the time(4). At our institution we have refined a sclerotherapy protocol that thus far has resulted in complete ablation of LMs in 95% of the macrocystic cases (n > 30). This protocol relies on time-limited contact of two sclerotherapy agents.

In order to compare the efficacy of this and other treatment regimens for sclerotherapy of LMs, an animal model is needed. Such a model might allow comparison of treatment regimens for microcystic malformations and succor development of treatments for microcystic and mixed LMs. A validated mouse model for LMs has been presented elsewhere in the literature; however, the tumors produced were confined to the peritoneum and too small for image guided interventions(11). We hypothesized that induction of lymphatic malformations would be possible in a large rodent model (rat);

and secondly, that these LMs could be induced in the soft tissues of the neck, the area where LMs most often occur in humans.

Methods:

The study was planned in consultation with our institution's attending veterinarian and approved by the Institutional Animal Care and Use. Twelve (n=12) healthy male immunocompetent Harlan Sprague-Dawley rats (wt. 300-325 grams) were used in this initial study. Under ultrasound (US) guidance experimental animals received one series of injections of incomplete Freund's adjuvant (IFA) (85% paraffin oil and 15% mannide monooleate by volume) (Sigma, St. Louis, Missouri) followed by a second US-guided series two weeks later. Nine (n=9) experimental animals received intraperitoneal injections of IFA. A subgroup (n=3) of these nine animals received additional IFA injections in a site in the neck (two injection sites total). Three (n=3) animals served as a control group and received saline IP injections

Following the injections animals were monitored by high-resolution ultrasound with a 15 MHZ Compact Linear Transducer (ATL) every two weeks for 100 days or more. Two animals were selected for imaging using a 4.7 MRI animal scanner (Bruker, Germany). Animals were sacrificed and identifiable lesions were dissected out. When possible cystic structures were removed without disrupting the cyst.

The tissue specimens were fixed in formalin and embedded in paraffin. Tissue staining and immunohistochemistry were performed through our institution's Core Laboratory. Tissues were serially sectioned and stained with H&E and Trichrome (BioGenex, San Ramon, CA) for collagen. Primary antibody stains for smooth muscle

actin ,anti-alpha-Sm-1 (Sigma, St. Louis, Missouri), and for endothelium, CD31 (Pharmingen) also known as PECAM-1 (Platelet Endothelial Cell Adhesion Molecule-1), and stains for lymphatic endothelium, Prox-1 (Abcam, Cambridge, MA)and flt-4 (VEGF-R3) (GeneTex, Sant Antonio) were employed according to basic immunohistochemical methods.

Results

All animals (n=9) receiving intraperitoneal injections developed microcystic malformations in the peritoneum. All of the animals (n=3) that received injections in the neck developed mixed malformations with both microcystic and macrocystic components. The macrocystic malformations were grossly palpable and visible by ultrasound. In animals that received neck injections, after 45 days fluid-filled cysts were visible with high-resolution ultrasound, the largest of which had grown to 9mm in its greatest dimension by sacrifice at 100 days post-injection. Intraperitoneal injections of IFA resulted in the development of white plaques within the peritoneum and along the superior margin of the liver with adhesive bands extending up to the diaphragm. Histologic analysis showed these regions to be consistent with microcystic lymphatic malformations. For both the microcystic and macrocystic malformations, histology demonstrated cystic spaces, a) lined with endothelium, b) supported by a connective tissue stroma, and c) filled with serous fluid. These malformations were found predominately along connective tissue planes but showed clear extension into muscles of the neck..

High resolution imaging of animals with 4.7 MRI at 100 days post-injection clearly demonstrated fluid-filled cysts with thickened walls. Additionally, the tissues surrounding the cysts showed increased signal on T-2 weighted imaging. Subsequent sacrifice of these animals and extraction of the imaged tissues showed tissue staining consistent with LMs.

Discussion

This study had a number of limitations, the first of which was the small sample size given that it was a pilot study. Furthermore, animals were sacrificed after only 100 days—a longer growth phase would likely have resulted in larger cysts. Though both macrocysts and microcysts were induced at specific areas in various tissues, the macrocysts are not quite large enough for evaluation of sclerotherapy regimens that utilize aspiration. The cysts are large enough for targeted delivery of therapeutics, though. More injections over time might cause increased growth of the cysts. In their original work Mancardi *et al* noted that two injections two weeks apart produced larger cysts than a single injection(11).

This study is just a beginning. In the future we will continue to define the model and expand upon our work to elucidate the mechanism of induction. More detailed immunohistochemistry will be performed to include recently identified stains specific for lymphatic endothelium (prox-1, podoplanin, flt-4). We will also examine the possibility of induction of LMs in additional sites and tissues. We will also begin to evaluate different sclerotherapy agents, with the eventual goal of developing the ideal therapy for

both microcystic and macrocystic LMs. This model will also allow us to investigate the mechanism of induction of these lymphatic malformations and look for ways to inhibit their formation. We will use this model to evaluate ultrasound guided sclerotherapy regimens. Once the model is validated, numerous treatment regimens by our group and others can be attempted in large numbers. Development of the model will allow the investigation of treatments for microcystic lesions, which have remained refractory to sclerotherapy treatment. The successes from the animal models can then be translated into clinical practice.

When we talk about induction of these lymphatic malformations, we are considering the formation and growth of lymphatic endothelium. The process induced then is lymphangiogenesis—site specific induction of lymphangiogenesis.

Lymphangiogenesis has recently become a very hot topic in the cancer literature given that the majority of human carcinomas metastasize initially via the lymphatics. Indeed, a great deal of recent study has been devoted to lymphangiogenesis and its inhibition.

Recent studies have confirmed that inhibition of lymphangiogenesis, mostly through blockage of VEGF-3 receptor activation, will block cancer metastasis. This model thus provides a means for *in vivo* testing of anti-lymphangiogenesis therapies. What is particularly exciting is that this model enables Interventional Radiology as a field to be involved in the study of anti-lymphangiogenesis therapies early on, whether it is by image-guided tumor ablation or by site-specific drug delivery or chemoembolization...

Lastly, one area where I find this model to be particularly exciting is as *in vivo* “micro”bioreactors for the evaluation of micro and nanotechnology derived devices such as those discussed in chapter 2. These cysts are tiny, self-contained fluid-filled spaces

lined with endothelium expressing a number of growth factors and specific receptors... devices designed to target such developing lymphatics could be evaluated in the cysts produced with this model(12)In conclusion, this study shows for the first time that lymphatic malformations are indeed inducible in a large rodent model in a site-specific manner. LMs can be produced in both the peritoneum and the neck and can involve multiple tissues. Both macrocystic and microcystic LMs can be produced with the methods described. The malformations can be followed with high-resolution ultrasound As such, this model is an excellent tool for sclerotherapy research.

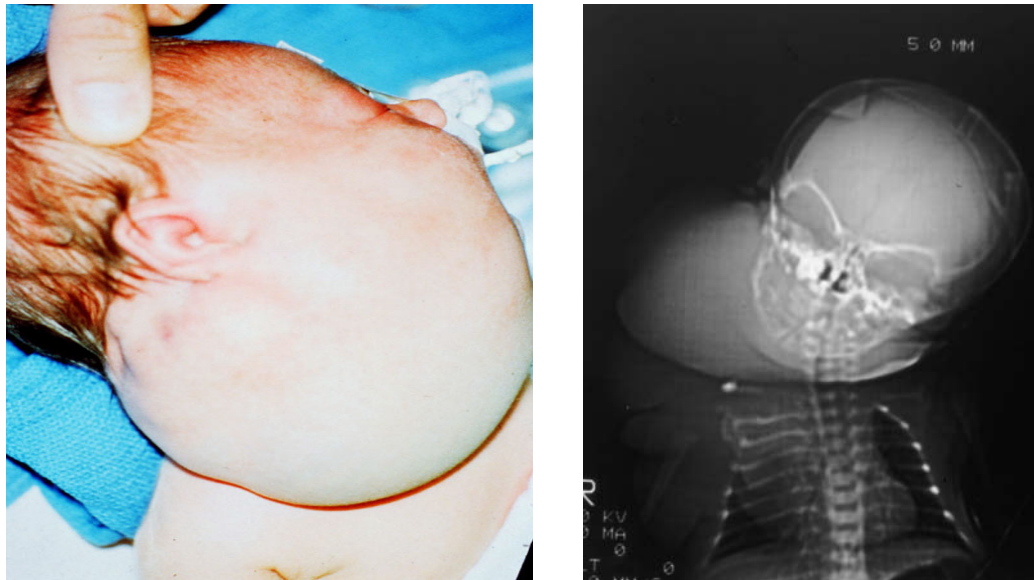


Figure 6.1: Example of a lymphatic malformation in an infant.

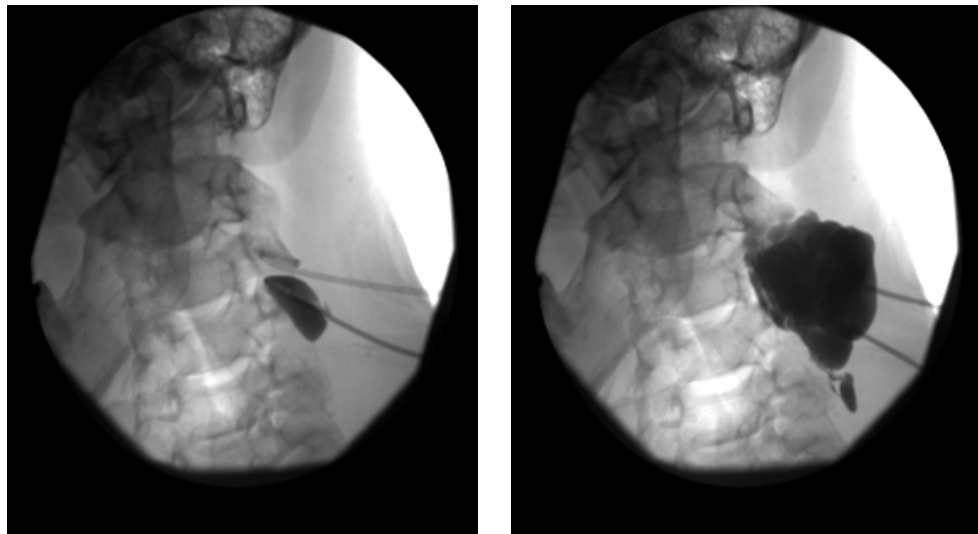


Figure 6.2: Treatment of lymphatic malformation by sclerotherapy. This contrast cystogram shows how drugs can be infused into the cysts percutaneously under image-guidance.

SCLEROTHERPAY AGENTS USED TO TREAT LYMPHATIC MALFORMATIONS

- Ethanol
 - Ethibloc
 - Fibrin glue
 - Bleomycin sulfate
 - OK-432
 - Sodium tetradecol sulfate
 - Interferon alfa-2a
 - Tetracycline
 - Doxycycline
 - Dual drug regimens
-

Table 6.1. Agents reported as useful for treatment of lymphatic malformations.

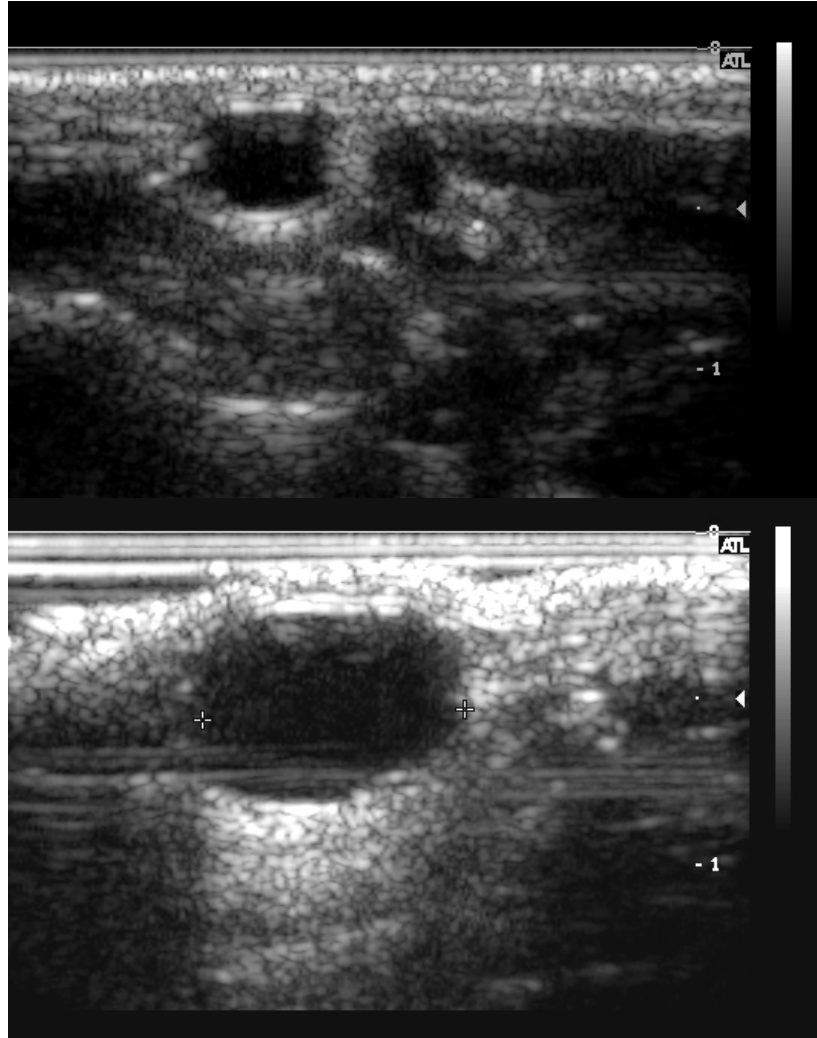


Figure 6.3: High resolution ultrasound images of cysts over time. Images show the same animal with growth of fluid-filled cysts 45 days (top) and 100 days (bottom).

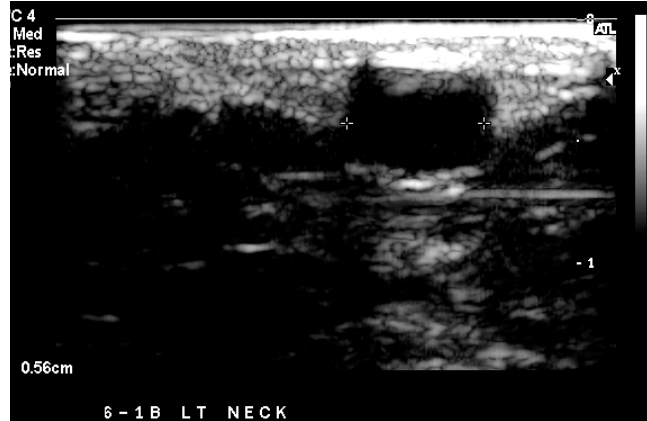


Figure 6.4: High resolution ultrasound image of lymphatic malformation. A large fluid-filled cyst, located in the axilla of the animal, measured 5.6 mm.

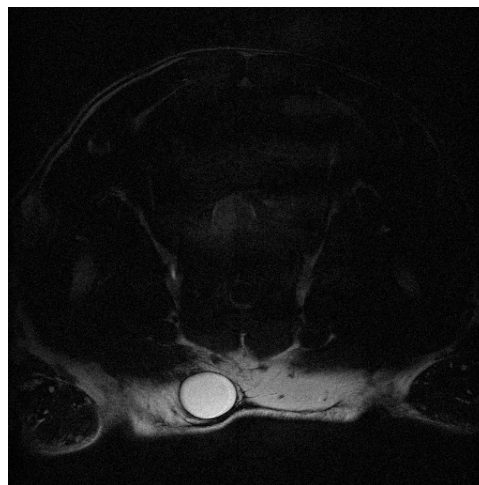
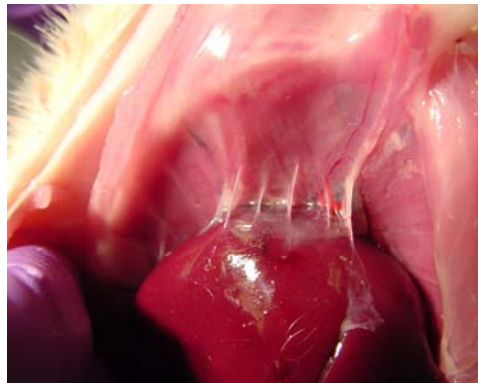


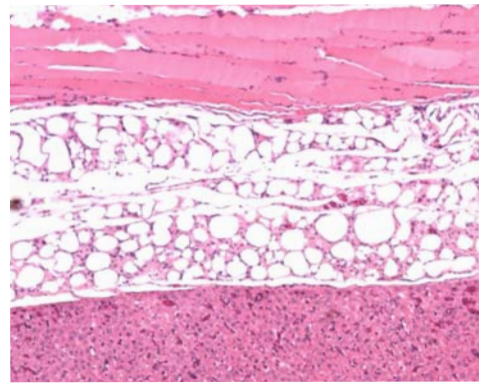
Figure 6.5: T-2 weighted 4.7 Tesla MRI image of the same animal and cyst as above. Enhancement in the surrounding musculature as well indicates of microcystic malformation, confirmed at necropsy.



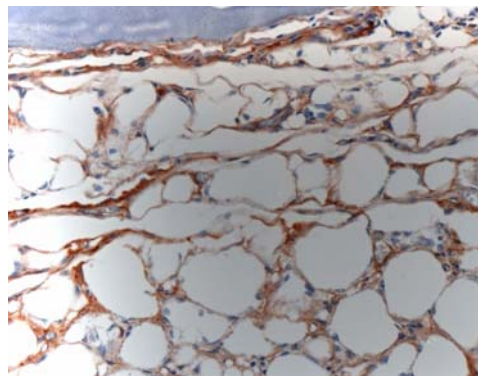
Figure 6.6: 4.7/40cm Tesla magnet MRI facility used for imaging of lymphatic malformations. The facility is part of the new Ohio Cellular and Molecular Imaging Consortium (OCMIC).



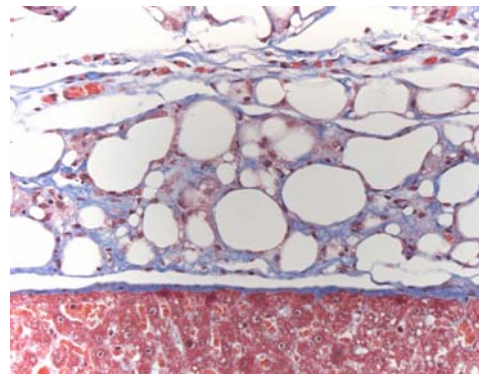
(A)



(B)

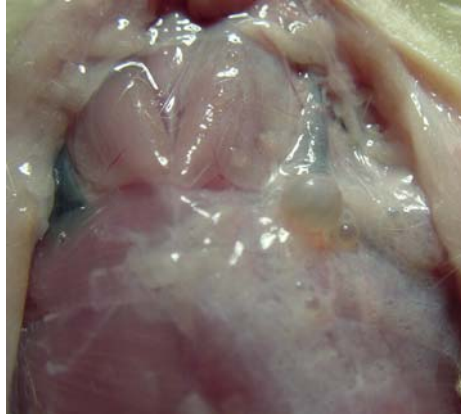


(C)

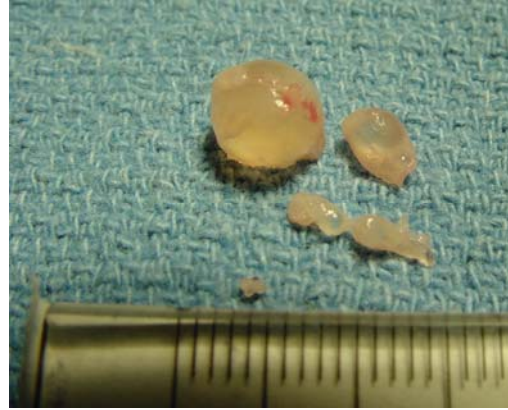


(D)

Figure 6.7: Pathological specimens from animal model intraperitoneal injections. (A) Gross picture of area of shows diaphragm and liver and abnormal adhesions between them; (B) H&E stained section of liver (bottom) and diaphragm (top) showing cystic malformations between; (C) CD31 stain (brown) of cystic spaces denoting endothelium; (D) Trichrome stain for collagen showing supporting connective tissue stroma and staining of liver (Glisson's) capsule



(A)



(B)

Figure 6.8: Gross specimens of lymphatic malformations from neck injections. (A) Macrocystic LMs *in vivo* and surrounding microcystic plaques. (B) Excised macrocysts demonstrated containment of serous fluid.

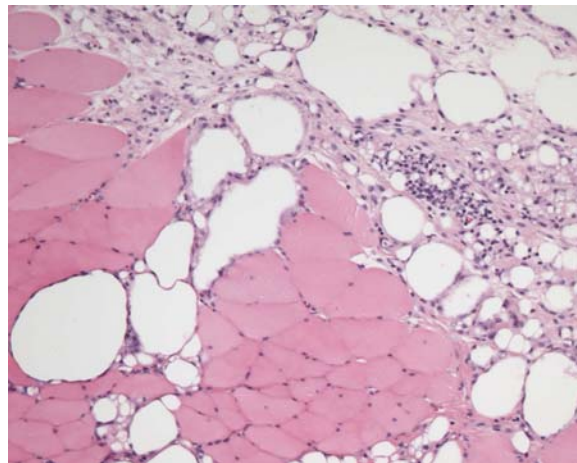


Figure 6.9: H&E staining of specimen from the neck, 50x magnification. This section shows infiltration of LM into the muscle tissues.

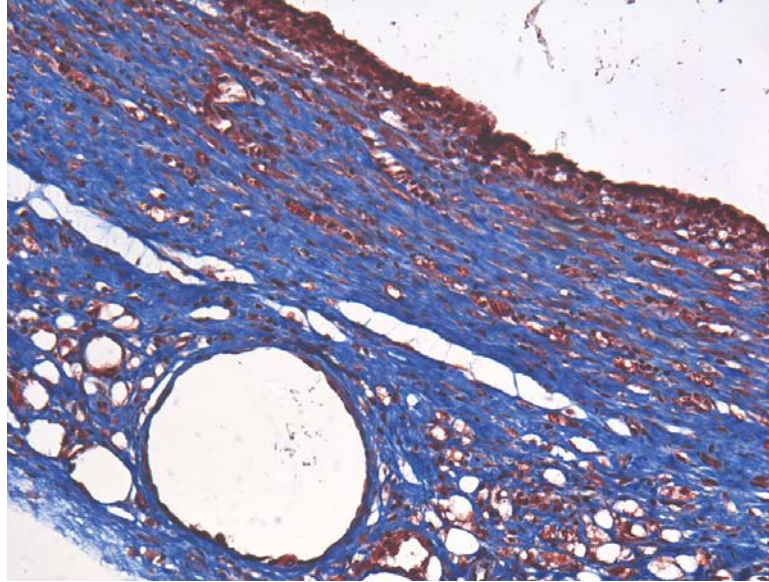


Figure 6.10: Tissue stained with eosin and flt-4, 125x magnification. Flt-4 (VEGF-R3) is a tyrosine kinase receptor associated with earlier lymphatic development.

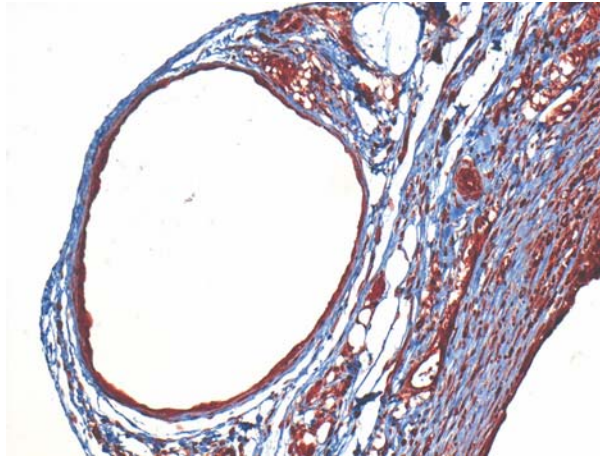
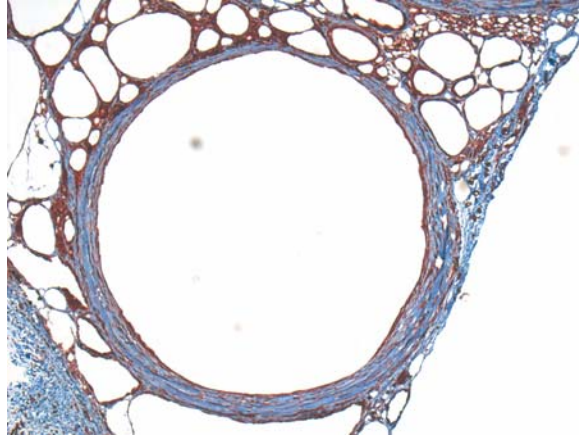


Figure 6.11: Sections stained with eosin and anti-prox-1 at 50x (top) and 100x magnification (bottom). Prox-1 is a homeobox gene identified as a marker of developing lymphatic endothelium. In these specimens, the inner rims of the cysts stain strongly with staining dispersed throughout the surrounding tissue.

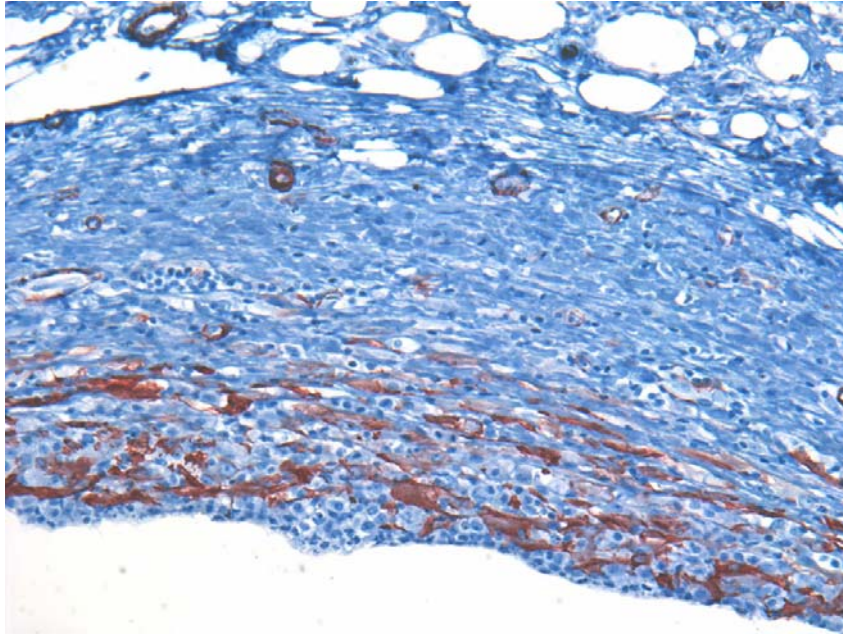


Figure 6.12: Eosin and anti-smooth muscle actin staining of cyst wall, 160 x magnification. The staining pattern is consistent with early deposition and organization of the thickened cyst wall.

REFERENCES

1. Charabi B, Bretlau P, Bille M, Holmelund M. Cystic hygroma of the head and neck--a long-term follow-up of 44 cases. *Acta Otolaryngol Suppl* 2000;543:248-50.
2. Orvidas LJ, Kasperbauer JL. Pediatric lymphangiomas of the head and neck. *Ann Otol Rhinol Laryngol* 2000;109(4):411-21.
3. Hamoir M, Plouin-Gaudon I, Rombaux P, Francois G, Cornu AS, Desuter G, et al. Lymphatic malformations of the head and neck: a retrospective review and a support for staging. *Head Neck* 2001;23(4):326-37.
4. Giguere CM, Bauman NM, Smith RJ. New treatment options for lymphangioma in infants and children. *Ann Otol Rhinol Laryngol* 2002;111(12 Pt 1):1066-75.
5. Burrows PE, Mason KP. Percutaneous Treatment of Low Flow Vascular Malformations. *J Vasc Interv Radiol* 2004;15(5):431-445.
6. Herbreteau D, Riche MC, Enjolras O, Khayata M, Lemarchand-Venencie F, Borsik M, et al. Percutaneous embolization with Ethibloc of lymphatic cystic malformations with a review of the experience in 70 patients. *Int Angiol* 1993;12(1):34-9.
7. Castanon M, Margarit J, Carrasco R, Vancells M, Albert A, Morales L. Long-term follow-up of nineteen cystic lymphangiomas treated with fibrin sealant. *J Pediatr Surg* 1999;34(8):1276-9.
8. Ogita S, Tsuto T, Nakamura K, Deguchi E, Iwai N. OK-432 therapy in 64 patients with lymphangioma. *J Pediatr Surg* 1994;29(6):784-5.
9. Rautio R, Keski-Nisula L, Laranne J, Laasonen E. Treatment of Lymphangiomas with OK-432 (Picibanil). *Cardiovasc Intervent Radiol* 2002;25:6.
10. Giguere CM, Bauman NM, Sato Y, Burke DK, Greinwald JH, Pransky S, et al. Treatment of lymphangiomas with OK-432 (Picibanil) sclerotherapy: a prospective multi-institutional trial. *Arch Otolaryngol Head Neck Surg* 2002;128(10):1137-44.
11. Mancardi S, Stanta G, Dusetti N, Bestagno M, Jussila L, Zweyer M, et al. Lymphatic endothelial tumors induced by intraperitoneal injection of incomplete Freund's adjuvant. *Exp Cell Res* 1999;246(2):368-75.

12. Krishnan J, Kirkin V, Steffen A, Hegen M, Weih D, Tomarev S, et al. Differential in vivo and in vitro expression of vascular endothelial growth factor (VEGF)-C and VEGF-D in tumors and its relationship to lymphatic metastasis in immunocompetent rats. *Cancer Res* 2003;63(3):713-22.

BIBLIOGRAPHY

1. Nanomedicine: grounds for optimism, and a call for papers. *Lancet* 2003;362(9385):673.
2. Achen MG, McColl BK, Stacker SA. Focus on lymphangiogenesis in tumor metastasis. *Cancer Cell* 2005;7(2):121-7.
3. Al-Rawi MA, Mansel RE, Jiang WG. Molecular and cellular mechanisms of lymphangiogenesis. *Eur J Surg Oncol* 2005;31(2):117-21.
4. Al-Rawi MA, Mansel RE, Jiang WG. Lymphangiogenesis and its role in cancer. *Histol Histopathol* 2005;20(1):283-98.
5. Almen A, Mattsson S. On the calculation of effective dose to children and adolescents. *Journal of Radiological Protection* 1996;16(2):81-89.
6. Almen A, Nilsson M. Simple methods for the estimation of dose distributions, organ doses and energy imparted in paediatric radiology. *Physics in Medicine and Biology* 1996;41(7):1093-1105.
7. Alper J. US NCI launches nanotechnology plan. *Nat Biotechnol* 2004;22(11):1335-6.
8. Alqahtani A, Nguyen LT, Flageole H, Shaw K, Laberge JM. 25 years' experience with lymphangiomas in children. *J Pediatr Surg* 1999;34(7):1164-8.
9. Amedee RG, Mann WJ, Lyons GD. Tracheomalacia repair using ceramic rings. *Otolaryngol Head Neck Surg* 1992;106(3):270-4.
10. Andersson H, van den Berg A. Microfabrication and microfluidics for tissue engineering: state of the art and future opportunities. *Lab Chip* 2004;4(2):98-103. Epub 2004 Mar 10.
11. Aquino SL, Shepard JA, Ginns LC, Moore RH, Halpern E, Grillo HC, et al. Acquired tracheomalacia: detection by expiratory CT scan. *J Comput Assist Tomogr* 2001;25(3):394-9.

12. Austin J, Ali T. Tracheomalacia and bronchomalacia in children: pathophysiology, assessment, treatment and anaesthesia management. *Paediatr Anaesth* 2003;13(1):3-11.
13. Baerlocher MO, Asch MR. The future interventional radiologist: clinician or hired gun? *J Vasc Interv Radiol* 2004;15(12):1385-90.
14. Beasley SW, Qi BQ. Understanding tracheomalacia. *J Paediatr Child Health* 1998;34(3):209-10.
15. Becker GJ. The 1999 Charles T. Dotter Lecture. Interventional radiology 2000 and beyond: back from the brink. *J Vasc Interv Radiol* 1999;10(6):681-7.
16. Becker H, Gartner C. Polymer microfabrication methods for microfluidic analytical applications. *Electrophoresis* 2000;21(1):12-26.
17. Becker GJ. 2000 RSNA annual oration in diagnostic radiology: The future of interventional radiology. *Radiology* 2001;220(2):281-92.
18. Benjamin B. Tracheomalacia in infants and children. *Ann Otol Rhinol Laryngol* 1984;93(5 Pt 1):438-42.
19. Berrocal T, Madrid C, Novo S, Gutierrez J, Arjonilla A, Gomez-Leon N. Congenital anomalies of the tracheobronchial tree, lung, and mediastinum: embryology, radiology, and pathology. *Radiographics* 2004;24(1):e17. Epub 2003 Nov 10.
20. Berry JA, Wolf JS, Gray WC. Squamous cell carcinoma arising in a lymphangioma of the tongue. *Otolaryngol Head Neck Surg* 2002;127(5):458-60.
21. Bloom DC, Perkins JA, Manning SC. Management of lymphatic malformations. *Curr Opin Otolaryngol Head Neck Surg* 2004;12(6):500-4.
22. Boone JM, Geraghty EM, Seibert JA, Wootton-Gorges SL. Dose reduction in pediatric CT: a rational approach. *Radiology* 2003;228(2):352-60.
23. Borecky N, Gudinchet F, Laurini R, Duvoisin B, Hohlfeld J, Schnyder P. Imaging of cervico-thoracic lymphangiomas in children. *Pediatr Radiol* 1995;25(2):127-30.
24. Breatnach E, Abbott GC, Fraser RG. Dimensions of the normal human trachea. *AJR Am J Roentgenol* 1984;142(5):903-6.
25. Brewis C, Pracy JP, Albert DM. Treatment of lymphangiomas of the head and neck in children by intralesional injection of OK-432 (Picibanil). *Clin Otolaryngol* 2000;25(2):130-4.

26. Brody AS, Kuhn JP, Seidel FG, Brodsky LS. Airway evaluation in children with use of ultrafast CT: pitfalls and recommendations. *Radiology* 1991;178(1):181-4.
27. Brown RL, Azizkhan RG. Pediatric head and neck lesions. *Pediatr Clin North Am* 1998;45(4):889-905.
28. Brown M, Pysher T, Coffin CM. Lymphangioma and congenital pulmonary lymphangiectasis: a histologic, immunohistochemical, and clinicopathologic comparison. *Mod Pathol* 1999;12(6):569-75.
29. Bugmann P, Rimensberger PC, Kalangos A, Barazzone C, Beghetti M, Lang FJ. Extratracheal biodegradable splint to treat life-threatening tracheomalacia. *Ann Thorac Surg* 2004;78(4):1446-8.
30. Burke AJ, Vining DJ, McGuirt WF, Jr., Postma G, Browne JD. Evaluation of airway obstruction using virtual endoscopy. *Laryngoscope* 2000;110(1):23-9.
31. Carson PL, Giger M, Welch MJ, Halpern H, Kurdziel K, Vannier M, et al. Biomedical Imaging Research Opportunities Workshop: report and recommendations. *Radiology* 2003;229(2):328-39. Epub 2003 Aug 18.
32. Cassese JA, Brody AS, Thomas SR. Utility of simple radiation dose measurements in the evaluation of different CT scanners used for high-resolution CT. *J Thorac Imaging* 2003;18(4):242-5.
33. Castanon M, Margarit J, Carrasco R, Vancells M, Albert A, Morales L. Long-term follow-up of nineteen cystic lymphangiomas treated with fibrin sealant. *J Pediatr Surg* 1999;34(8):1276-9.
34. Castanon Garcia-Alix M, Margarit Mallol J, Martin Hortiguela ME, Salarich de Arbell J. [Fibrin adhesive: a new therapeutic alternative in the treatment of cystic lymphangioma]. *An Esp Pediatr* 1993;38(4):304-6.
35. Chang LK, Garcia-Cardena G, Farnebo F, Fannon M, Chen EJ, Butterfield C, et al. Dose-dependent response of FGF-2 for lymphangiogenesis. *Proc Natl Acad Sci U S A* 2004;101(32):11658-63. Epub 2004 Aug 2.
36. Chang AB, Gaffney JT, Eastburn MM, Faoagali J, Cox NC, Masters IB. Cough quality in children: a comparison of subjective vs. bronchoscopic findings. *Respir Res* 2005;6(1):3.
37. Charabi B, Bretlau P, Bille M, Holmelund M. Cystic hygroma of the head and neck--a long-term follow-up of 44 cases. *Acta Otolaryngol Suppl* 2000;543:248-50.

38. Cheng KH, Cheng YS, Yeh HC, Swift DL. Measurements of airway dimensions and calculation of mass transfer characteristics of the human oral passage. *J Biomech Eng* 1997;119(4):476-82.
39. Claesson G, Kuylenstierna R. OK-432 therapy for lymphatic malformation in 32 patients (28 children). *Int J Pediatr Otorhinolaryngol* 2002;65(1):1-6.
40. Cody DD, Moxley DM, Krugh KT, O'Daniel JC, Wagner LK, Eftekhari F. Strategies for formulating appropriate MDCT techniques when imaging the chest, abdomen, and pelvis in pediatric patients. *AJR Am J Roentgenol* 2004;182(4):849-59.
41. Cogbill TH, Moore FA, Accurso FJ, Lilly JR. Primary tracheomalacia. *Ann Thorac Surg* 1983;35(5):538-41.
42. Coldwell DM, Sewell PE. The expanding role of interventional radiology in the supportive care of the oncology patient: From diagnosis to therapy. *Semin Oncol* 2005;32(2):169-73.
43. Dadras SS, Lange-Asschenfeldt B, Velasco P, Nguyen L, Vora A, Muzikansky A, et al. Tumor lymphangiogenesis predicts melanoma metastasis to sentinel lymph nodes. *Mod Pathol* 2005;1:1.
44. Daniels CB, Lewis BC, Tsopelas C, Munns SL, Orgeig S, Baldwin ME, et al. Regenerating lizard tails: a new model for investigating lymphangiogenesis. *Faseb J* 2003;17(3):479-81. Epub 2003 Jan 2.
45. Dass CR. Oligonucleotide delivery to tumours using macromolecular carriers. *Biotechnol Appl Biochem* 2004;40(Pt 2):113-22.
46. Davis S, Jones M, Kisling J, Angelicchio C, Tepper RS. Effect of continuous positive airway pressure on forced expiratory flows in infants with tracheomalacia. *Am J Respir Crit Care Med* 1998;158(1):148-52.
47. Donnelly LF. Reducing radiation dose associated with pediatric CT by decreasing unnecessary examinations. *AJR Am J Roentgenol* 2005;184(2):655-7.
48. Dubois J, Garel L, Grignon A, David M, Laberge L, Filiatrault D, et al. Imaging of hemangiomas and vascular malformations in children. *Acad Radiol* 1998;5(5):390-400.
49. Dubois J, Garel L. Imaging and therapeutic approach of hemangiomas and vascular malformations in the pediatric age group. *Pediatr Radiol* 1999;29(12):879-93.
50. Duncan S, Eid N. Tracheomalacia and bronchopulmonary dysplasia. *Ann Otol Rhinol Laryngol* 1991;100(10):856-8.

51. Emerich DF, Thanos CG. Nanotechnology and medicine. *Expert Opin Biol Ther* 2003;3(4):655-63.
52. Emerich DF. Nanomedicine--prospective therapeutic and diagnostic applications. *Expert Opin Biol Ther* 2005;5(1):1-5.
53. Esteban MJ, Gutierrez C, Gomez J, Barrios JE, Lluna J, Fernandez MS, et al. [Treatment with Ethibloc of lymphangiomas and venous angiomas]. *Cir Pediatr* 1996;9(4):158-62.
54. Eyles JE, Carpenter ZC, Alpar HO, Williamson ED. Immunological aspects of polymer microsphere vaccine delivery systems. *J Drug Target* 2003;11(8-10):509-14.
55. Eyrich GK, Bruder E, Hilfiker P, Dubno B, Quick HH, Patak MA, et al. Temperature mapping of magnetic resonance-guided laser interstitial thermal therapy (LITT) in lymphangiomas of the head and neck. *Lasers Surg Med* 2000;26(5):467-76.
56. Fageeh N, Manoukian J, Tewfik T, Schloss M, Williams HB, Gaskin D. Management of head and neck lymphatic malformations in children. *J Otolaryngol* 1997;26(4):253-8.
57. Farmand M, Kuttenger JJ. A new therapeutic concept for the treatment of cystic hygroma. *Oral Surg Oral Med Oral Pathol Oral Radiol Endod* 1996;81(4):389-95.
58. Faust RA, Remley KB, Rimell FL. Real-time, cine magnetic resonance imaging for evaluation of the pediatric airway. *Laryngoscope* 2001;111(12):2187-90.
59. Fayon M, Donato L, de Blic J, Labbe A, Becmeur F, Mely L, et al. French experience of silicone tracheobronchial stenting in children. *Pediatr Pulmonol* 2005;39(1):21-7.
60. Fearon B, Whalen JS. Tracheal dimensions in the living infant (preliminary report). *Ann Otol Rhinol Laryngol* 1967;76(5):965-74.
61. Feist JH, Johnson TH, Wilson RJ. Acquired tracheomalacia: etiology and differential diagnosis. *Chest* 1975;68(3):340-5.
62. Filler RM, de Fraga JC. Tracheomalacia. *Semin Thorac Cardiovasc Surg* 1994;6(4):211-5.
63. Filston HC. Hemangiomas, cystic hygromas, and teratomas of the head and neck. *Semin Pediatr Surg* 1994;3(3):147-59.

64. Finder JD. Primary bronchomalacia in infants and children. *J Pediatr* 1997;130(1):59-66.
65. Fliegelman LJ, Friedland D, Brandwein M, Rothschild M. Lymphatic malformation: predictive factors for recurrence. *Otolaryngol Head Neck Surg* 2000;123(6):706-10.
66. Folpe AL, Veikkola T, Valtola R, Weiss SW. Vascular endothelial growth factor receptor-3 (VEGFR-3): a marker of vascular tumors with presumed lymphatic differentiation, including Kaposi's sarcoma, kaposiform and Dabska-type hemangioendotheliomas, and a subset of angiosarcomas. *Mod Pathol* 2000;13(2):180-5.
67. Fonseca C, Simoes S, Gaspar R. Paclitaxel-loaded PLGA nanoparticles: preparation, physicochemical characterization and in vitro anti-tumoral activity. *J Control Release* 2002;83(2):273-286.
68. Franchi A, Gallo O, Massi D, Baroni G, Santucci M. Tumor lymphangiogenesis in head and neck squamous cell carcinoma: a morphometric study with clinical correlations. *Cancer* 2004;101(5):973-8.
69. Fricke BL, Donnelly LF, Frush DP, Yoshizumi T, Varchena V, Poe SA, et al. In-plane bismuth breast shields for pediatric CT: effects on radiation dose and image quality using experimental and clinical data. *AJR Am J Roentgenol* 2003;180(2):407-11.
70. Frush DP, Slack CC, Hollingsworth CL, Bisset GS, Donnelly LF, Hsieh J, et al. Computer-simulated radiation dose reduction for abdominal multidetector CT of pediatric patients. *AJR Am J Roentgenol* 2002;179(5):1107-13.
71. Frush DP. Pediatric CT: practical approach to diminish the radiation dose. *Pediatr Radiol* 2002;32(10):714-7; discussion 751-4. Epub 2002 Aug 29.
72. Frush DP, Donnelly LF, Rosen NS. Computed tomography and radiation risks: what pediatric health care providers should know. *Pediatrics* 2003;112(4):951-7.
73. Fukunaga M. Expression of D2-40 in lymphatic endothelium of normal tissues and in vascular tumours. *Histopathology* 2005;46(4):396-402.
74. Furman RH, Backer CL, Dunham ME, Donaldson J, Mavroudis C, Holinger LD. The use of balloon-expandable metallic stents in the treatment of pediatric tracheomalacia and bronchomalacia. *Arch Otolaryngol Head Neck Surg* 1999;125(2):203-7.
75. Galambos C, Nodit L. Identification of Lymphatic Endothelium in Pediatric Vascular Tumors and Malformations. *Pediatr Dev Pathol* 2005;23:23.

76. Geijer H. Radiation dose and image quality in diagnostic radiology. Optimization of the dose-image quality relationship with clinical experience from scoliosis radiography, coronary intervention and a flat-panel digital detector. *Acta Radiol Suppl* 2002;43(427):1-43.
77. Geller KA, Wells WJ, Koempel JA, St John MA. Use of the Palmaz stent in the treatment of severe tracheomalacia. *Ann Otol Rhinol Laryngol* 2004;113(8):641-7.
78. Giguere CM, Bauman NM, Smith RJ. New treatment options for lymphangioma in infants and children. *Ann Otol Rhinol Laryngol* 2002;111(12 Pt 1):1066-75.
79. Giguere CM, Bauman NM, Sato Y, Burke DK, Greinwald JH, Pransky S, et al. Treatment of lymphangiomas with OK-432 (Picibanil) sclerotherapy: a prospective multi-institutional trial. *Arch Otolaryngol Head Neck Surg* 2002;128(10):1137-44.
80. Griscom NT. Computed tomographic determination of tracheal dimensions in children and adolescents. *Radiology* 1982;145(2):361-4.
81. Griscom NT. Tracheal dimensions. *AJR Am J Roentgenol* 1984;143(6):1352-3.
82. Griscom NT, Wohl ME. Dimensions of the growing trachea related to body height. Length, anteroposterior and transverse diameters, cross-sectional area, and volume in subjects younger than 20 years of age. *Am Rev Respir Dis* 1985;131(6):840-4.
83. Griscom NT, Wohl ME. Dimensions of the growing trachea related to age and gender. *AJR Am J Roentgenol* 1986;146(2):233-7.
84. Griscom NT, Wohl ME, Fenton T. Dimensions of the trachea to age 6 years related to height. *Pediatr Pulmonol* 1989;6(3):186-90.
85. Hachisuka T, Narikiyo M, Yamada Y, Ishikawa H, Ueno M, Uchida H, et al. High lymphatic vessel density correlates with overexpression of VEGF-C in gastric cancer. *Oncol Rep* 2005;13(4):733-7.
86. Hall EJ. Lessons we have learned from our children: cancer risks from diagnostic radiology. *Pediatr Radiol* 2002;32(10):700-6. Epub 2002 Jul 19.
87. Hamoir M, Plouin-Gaudon I, Rombaux P, Francois G, Cornu AS, Desuter G, et al. Lymphatic malformations of the head and neck: a retrospective review and a support for staging. *Head Neck* 2001;23(4):326-37.
88. Hasegawa I, Boiselle PM, Raptopoulos V, Hatabu H. Tracheomalacia incidentally detected on CT pulmonary angiography of patients with suspected pulmonary embolism. *AJR Am J Roentgenol* 2003;181(6):1505-9.

89. Heether J, Whalen T, Doolin E. Follow-up of complex unresectable lymphangiomas. *Am Surg* 1994;60(11):840-1.
90. Hein E, Rogalla P, Hentschel C, Taupitz M, Hamm B. Dynamic and quantitative assessment of tracheomalacia by electron beam tomography: correlation with clinical symptoms and bronchoscopy. *J Comput Assist Tomogr* 2000;24(2):247-52.
91. Herbreteau D, Riche MC, Enjolras O, Khayata M, Lemarchand-Venencie F, Borsik M, et al. Percutaneous embolization with Ethibloc of lymphatic cystic malformations with a review of the experience in 70 patients. *Int Angiol* 1993;12(1):34-9.
92. Hoeben A, Landuyt B, Highley MS, Wildiers H, Van Oosterom AT, De Bruijn EA. Vascular endothelial growth factor and angiogenesis. *Pharmacol Rev* 2004;56(4):549-80.
93. Hojreh A, Kainberger F, Puig S. [Low dose multislice CT in the pediatric patient]. *Radiologe* 2003;43(12):1051-5.
94. Holland AJ, Suriyarachchi CP, Harvey JG, Cooper P, Mellis CM. Tracheomalacia, timing of symptoms, and thymic enlargement: cause or coincidence? *J Pediatr Surg* 2003;38(7):1094-5.
95. Hombreiro Perez M, Zinutti C, Lamprecht A, Ubrich N, Astier A, Hoffman M, et al. The preparation and evaluation of poly(epsilon-caprolactone) microparticles containing both a lipophilic and a hydrophilic drug. *J Control Release* 2000;65(3):429-38.
96. Honnef D, Wildberger JE, Stargardt A, Hohl C, Barker M, Gunther RW, et al. [Multislice spiral CT (MSCT) in pediatric radiology: dose reduction for chest and abdomen examinations]. *Rofo* 2004;176(7):1021-30.
97. Hood JD, Bednarski M, Frausto R, Guccione S, Reisfeld RA, Xiang R, et al. Tumor regression by targeted gene delivery to the neovasculature. *Science* 2002;296(5577):2404-7.
98. Huang HY, Ho CC, Huang PH, Hsu SM. Co-expression of VEGF-C and its receptors, VEGFR-2 and VEGFR-3, in endothelial cells of lymphangioma. Implication in autocrine or paracrine regulation of lymphangioma. *Lab Invest* 2001;81(12):1729-34.
99. Huda W, Scalzetti EM, Roskopf M. Effective doses to patients undergoing thoracic computed tomography examinations. *Medical Physics* 2000;27(5):838-844.
100. Huda W, Ravenel JG, Scalzetti EM. How do radiographic techniques affect image quality and patient doses in CT? *Semin Ultrasound CT MR* 2002;23(5):411-22.

101. Hunold P, Vogt FM, Schmermund A, Debatin JF, Kerkhoff G, Budde T, et al. Radiation exposure during cardiac CT: effective doses at multi-detector row CT and electron-beam CT. *Radiology* 2003;226(1):145-52.
102. Inoue K, Yanagihara J, Ono S, Kubota Y, Iwai N. Utility of helical CT for diagnosis and operative planning in tracheomalacia after repair of esophageal atresia. *Eur J Pediatr Surg* 1998;8(6):355-7.
103. Isaacson G. Tracheomalacia and bronchopulmonary dysplasia. *Ann Otol Rhinol Laryngol* 1992;101(4):372.
104. Jackson DG. Biology of the lymphatic marker LYVE-1 and applications in research into lymphatic trafficking and lymphangiogenesis. *Apmis* 2004;112(7-8):526-38.
105. Jacob AL, Regazzoni P, Steinbrich W, Messmer P. The multifunctional therapy room of the future: image guidance, interdisciplinarity, integration and impact on patient pathways. *Eur Radiol* 2000;10(11):1763-9.
106. Jain RA. The manufacturing techniques of various drug loaded biodegradable poly(lactide-co-glycolide) (PLGA) devices. *Biomaterials* 2000;21(23):2475-90.
107. Jain R, Bandhu S, Sawhney S, Mittal R. Sonographically guided percutaneous sclerosis using 1% polidocanol in the treatment of vascular malformations. *J Clin Ultrasound* 2002;30(7):416-23.
108. Jaquiss RD. Management of pediatric tracheal stenosis and tracheomalacia. *Semin Thorac Cardiovasc Surg* 2004;16(3):220-4.
109. Jeong JC, Lee J, Cho K. Effects of crystalline microstructure on drug release behavior of poly(epsilon-caprolactone) microspheres. *J Control Release* 2003;92(3):249-58.
110. Ji RC. Characteristics of lymphatic endothelial cells in physiological and pathological conditions. *Histol Histopathol* 2005;20(1):155-75.
111. Jiang W, Gupta RK, Deshpande MC, Schwendeman SP. Biodegradable poly(lactic-co-glycolic acid) microparticles for injectable delivery of vaccine antigens. *Adv Drug Deliv Rev* 2005;57(3):391-410.
112. Jilek S, Merkle HP, Walter E. DNA-loaded biodegradable microparticles as vaccine delivery systems and their interaction with dendritic cells. *Adv Drug Deliv Rev* 2005;57(3):377-90.

113. Kalb C. The war on disease goes miniature. *Nanomedicine: drugs and cancer tests, cell by cell*. Newsweek 2000;134(26):89.
114. Kao SC, Kimura K, Smith WL, Sato Y. Tracheomalacia before and after aortosternotomy: dynamic and quantitative assessment by electron-beam computed tomography with clinical correlation. *Pediatr Radiol* 1995;25 Suppl 1:S187-93.
115. Kathary N, Bulas DI, Newman KD, Schonberg RL. MRI imaging of fetal neck masses with airway compromise: utility in delivery planning. *Pediatr Radiol* 2001;31(10):727-31.
116. Katsuno S, Ezawa S, Minemura T. Excision of cervical cystic lymphangioma using injection of hydrocolloid dental impression material. A technical case report. *Int J Oral Maxillofac Surg* 1999;28(4):295-6.
117. Kawakami Y, Nishimura M, Kusaka H. Tracheal dimensions at full inflation and deflation in adolescent twins. *J Appl Physiol* 1991;70(4):1781-6.
118. Kayser O, Lemke A, Hernandez-Trejo N. The impact of nanobiotechnology on the development of new drug delivery systems. *Curr Pharm Biotechnol* 2005;6(1):3-5.
119. Kennedy TL, Whitaker M, Pellitteri P, Wood WE. Cystic hygroma/lymphangioma: a rational approach to management. *Laryngoscope* 2001;111(11 Pt 1):1929-37.
120. Kim H, Dumont DJ. Molecular mechanisms in lymphangiogenesis: model systems and implications in human disease. *Clin Genet* 2003;64(4):282-92.
121. Kim KH, Sung MW, Roh JL, Han MH. Sclerotherapy for congenital lesions in the head and neck. *Otolaryngol Head Neck Surg* 2004;131(3):307-16.
122. Koch BL. Cystic malformations of the neck in children. *Pediatr Radiol* 2005;35(5):463-477. Epub 2005 Mar 23.
123. Koh D-M, Cook GJR, Husband JE. *New Horizons in Oncologic Imaging*. *N Engl J Med* 2003;348(25):2487-2488.
124. Koh DM, Cook GJ, Husband JE. New horizons in oncologic imaging. *N Engl J Med* 2003;348(25):2487-8.
125. Kosucu P, Ahmetoglu A, Koramaz I, Orhan F, Ozdemir O, Dinc H, et al. Low-dose MDCT and virtual bronchoscopy in pediatric patients with foreign body aspiration. *AJR Am J Roentgenol* 2004;183(6):1771-7.

126. Kumasaka T, Seyama K, Mitani K, Sato T, Souma S, Kondo T, et al. Lymphangiogenesis in lymphangioliomyomatosis: its implication in the progression of lymphangioliomyomatosis. *Am J Surg Pathol* 2004;28(8):1007-16.
127. Kyzas PA, Geleff S, Batistatou A, Agnantis NJ, Stefanou D. Evidence for lymphangiogenesis and its prognostic implications in head and neck squamous cell carcinoma. *J Pathol* 2005;206(2):170-7.
128. Laranne J, Keski-Nisula L, Rautio R, Rautiainen M, Airaksinen M. OK-432 (Picibanil) therapy for lymphangiomas in children. *Eur Arch Otorhinolaryngol* 2002;259(5):274-8.
129. Lee BB, Kim YW, Seo JM, Hwang JH, Do YS, Kim DI, et al. Current concepts in lymphatic malformation. *Vasc Endovascular Surg* 2005;39(1):67-81.
130. Lengsfeld CS, Manning MC, Randolph TW. Encapsulating DNA within biodegradable polymeric microparticles. *Curr Pharm Biotechnol* 2002;3(3):227-35.
131. Lev S, Lev MH. Imaging of cystic lesions. *Radiol Clin North Am* 2000;38(5):1013-27.
132. Li Y, Shawgo RS, Tyler B, Henderson PT, Vogel JS, Rosenberg A, et al. In vivo release from a drug delivery MEMS device. *J Control Release* 2004;100(2):211-9.
133. Li KC, Pandit SD, Guccione S, Bednarski MD. Molecular imaging applications in nanomedicine. *Biomed Microdevices* 2004;6(2):113-6.
134. Liddell RP, Weiss CR, Hofmann LV. Therapeutic angiogenesis: the next frontier for interventional radiology. *Tech Vasc Interv Radiol* 2004;7(1):40-8.
135. Lin WJ, Huang LI. Fabrication of porous poly(epsilon-caprolactone) microparticles for protein release. *J Microencapsul* 2001;18(5):577-84.
136. Linton OW, Mettler FA, Jr. National conference on dose reduction in CT, with an emphasis on pediatric patients. *AJR Am J Roentgenol* 2003;181(2):321-9.
137. Long FR, Castile RG. Technique and clinical applications of full-inflation and end-exhalation controlled-ventilation chest CT in infants and young children. *Pediatr Radiol* 2001;31(6):413-22.
138. Lugo-Olivieri CH, Taylor GA. CT differentiation of large abdominal lymphangioma from ascites. *Pediatr Radiol* 1993;23(2):129-30.
139. Luzzatto C, Midrio P, Tchaprassian Z, Guglielmi M. Sclerosing treatment of lymphangiomas with OK-432. *Arch Dis Child* 2000;82(4):316-8.

140. Maddalozzo J, Hughes CA, Huang L, Mu Y, Ludemann J, Crawford S. High angiogenic activity in cells isolated from cystic hygroma: role of bFGF. *Arch Otolaryngol Head Neck Surg* 1999;125(1):45-8.
141. Maher MM, Kalra MK, Toth TL, Wittram C, Saini S, Shepard J. Application of rational practice and technical advances for optimizing radiation dose for chest CT. *J Thorac Imaging* 2004;19(1):16-23.
142. Mainardes RM, Silva LP. Drug delivery systems: past, present, and future. *Curr Drug Targets* 2004;5(5):449-55.
143. Mancardi S, Stanta G, Dusetti N, Bestagno M, Jussila L, Zweyer M, et al. Lymphatic endothelial tumors induced by intraperitoneal injection of incomplete Freund's adjuvant. *Exp Cell Res* 1999;246(2):368-75.
144. Margulis AR, Sunshine JH. Radiology at the turn of the millennium. *Radiology* 2000;214(1):15-23.
145. Marler JJ, Mulliken JB. Current management of hemangiomas and vascular malformations. *Clin Plast Surg* 2005;32(1):99-116, ix.
146. Martinez-Menchon T, Mahiques-Santos L, Febrer-Bosch I, Valcuende-Cavero F, Fortea-Baixaui JM. Lymphangioma circumscriptum: an example of Whimster's hypothesis. *Pediatr Dermatol* 2004;21(6):652-4.
147. Masters IB, Chang AB, Patterson L, Wainwright C, Buntain H, Dean BW, et al. Series of laryngomalacia, tracheomalacia, and bronchomalacia disorders and their associations with other conditions in children. *Pediatr Pulmonol* 2002;34(3):189-95.
148. Mayo JR, Hartman TE, Lee KS, Primack SL, Vedal S, Muller NL. CT of the chest: minimal tube current required for good image quality with the least radiation dose. *AJR Am J Roentgenol* 1995;164(3):603-7.
149. Mayo JR, Aldrich J, Muller NL. Radiation exposure at chest CT: a statement of the Fleischner Society. *Radiology* 2003;228(1):15-21.
150. Mayo JR, Kim KI, MacDonald SL, Johkoh T, Kavanagh P, Coxson HO, et al. Reduced radiation dose helical chest CT: effect on reader evaluation of structures and lung findings. *Radiology* 2004;232(3):749-56. Epub 2004 Jul 29.
151. McNamara VM, Crabbe DC. Tracheomalacia. *Paediatr Respir Rev* 2004;5(2):147-54.

152. McNitt-Gray MF. AAPM/RSNA Physics Tutorial for Residents: Topics in CT. Radiation dose in CT. *Radiographics* 2002;22(6):1541-53.
153. Menei P, Benoit JP, Boisdron-Celle M, Fournier D, Mercier P, Guy G. Drug targeting into the central nervous system by stereotactic implantation of biodegradable microspheres. *Neurosurgery* 1994;34(6):1058-64; discussion 1064.
154. Mikhail M, Kennedy R, Cramer B, Smith T. Sclerosing of recurrent lymphangioma using OK-432. *J Pediatr Surg* 1995;30(8):1159-60.
155. Moaz K, Greatorex RA, Allen JG. Identifying tracheomalacia--an alternative approach. *Br J Anaesth* 2000;85(2):332-3.
156. Moghimi SM, Hunter AC, Murray JC. Nanomedicine: current status and future prospects. *Faseb J* 2005;19(3):311-30.
157. Molitch HI, Unger EC, Witte CL, vanSonnenberg E. Percutaneous sclerotherapy of lymphangiomas. *Radiology* 1995;194(2):343-7.
158. Morgan HT. Dose reduction for CT pediatric imaging. *Pediatr Radiol* 2002;32(10):724-8; discussion 751-4. Epub 2002 Aug 29.
159. Mouta C, Heroult M. Inflammatory triggers of lymphangiogenesis. *Lymphat Res Biol* 2003;1(3):201-18.
160. Nagy JA, Vasile E, Feng D, Sundberg C, Brown LF, Detmar MJ, et al. Vascular permeability factor/vascular endothelial growth factor induces lymphangiogenesis as well as angiogenesis. *J Exp Med* 2002;196(11):1497-506.
161. Naidu SI, McCalla MR. Lymphatic malformations of the head and neck in adults: a case report and review of the literature. *Ann Otol Rhinol Laryngol* 2004;113(3 Pt 1):218-22.
162. Nakamura Y, Yasuoka H, Tsujimoto M, Imabun S, Nakahara M, Nakao K, et al. Lymph vessel density correlates with nodal status, VEGF-C expression, and prognosis in breast cancer. *Breast Cancer Res Treat* 2005;91(2):125-32.
163. Newth CJ, Lipton MJ, Gould RG, Stretton M. Varying tracheal cross-sectional area during respiration in infants and children with suspected upper airway obstruction by computed cinetomography scanning. *Pediatr Pulmonol* 1990;9(4):224-32.
164. Ng JW, Wong MK. The difficulties and risks of surgical treatment of lymphangiomas in the cervicofacial region. *J Pediatr Surg* 1996;31(10):1463-4.

165. Nickoloff EL, Dutta AK, Lu ZF. Influence of phantom diameter, kVp and scan mode upon computed tomography dose index. *Med Phys* 2003;30(3):395-402.
166. Nitta N, Takahashi M, Murata K, Morita R. Ultra low-dose helical CT of the chest: evaluation in clinical cases. *Radiat Med* 1999;17(1):1-7.
167. Nixon C. Tracheal dimensions in childhood. *AJR Am J Roentgenol* 1986;147(5):1094-5.
168. Ogita S, Tsuto T, Nakamura K, Deguchi E, Iwai N. OK-432 therapy in 64 patients with lymphangioma. *J Pediatr Surg* 1994;29(6):784-5.
169. Ogita S, Tsuto T, Nakamura K, Deguchi E, Tokiwa K, Iwai N. OK-432 therapy for lymphangioma in children: why and how does it work? *J Pediatr Surg* 1996;31(4):477-80.
170. Okazaki J, Isono S, Hasegawa H, Sakai M, Nagase Y, Nishino T. Quantitative assessment of tracheal collapsibility in infants with tracheomalacia. *Am J Respir Crit Care Med* 2004;170(7):780-5. Epub 2004 Jul 8.
171. Orford J, Barker A, Thonell S, King P, Murphy J. Bleomycin therapy for cystic hygroma. *J Pediatr Surg* 1995;30(9):1282-7.
172. Orvidas LJ, Kasperbauer JL. Pediatric lymphangiomas of the head and neck. *Ann Otol Rhinol Laryngol* 2000;109(4):411-21.
173. Padera TP, Kadambi A, di Tomaso E, Carreira CM, Brown EB, Boucher Y, et al. Lymphatic metastasis in the absence of functional intratumor lymphatics. *Science* 2002;296(5574):1883-6. Epub 2002 Apr 25.
174. Palazzo FF, Allen JG, Grestorex RA. Laryngeal mask airway and fibre-optic tracheal inspection in thyroid surgery: a method for timely identification of tracheomalacia requiring tracheostomy. *Ann R Coll Surg Engl* 2000;82(2):141-2.
175. Park YW, Kim SM, Min BG, Park IW, Lee SK. Lymphangioma involving the mandible: immunohistochemical expressions for the lymphatic proliferation. *J Oral Pathol Med* 2002;31(5):280-3.
176. Partain CL, Mattrey RF. Report on the NIBIB update and opportunities symposium. *Acad Radiol* 2002;9(9):1115-8.
177. Partanen TA, Alitalo K, Miettinen M. Lack of lymphatic vascular specificity of vascular endothelial growth factor receptor 3 in 185 vascular tumors. *Cancer* 1999;86(11):2406-12.

178. Paston F, Bye M. Tracheomalacia. *Pediatr Rev* 1996;17(9):328.
179. Paterson A, Frush DP, Donnelly LF. Helical CT of the body: are settings adjusted for pediatric patients? *AJR Am J Roentgenol* 2001;176(2):297-301.
180. Patton DF, Kaye R, Dickman P, Blatt J. Partial splenic embolization for treatment of disseminated intravascular coagulation in lymphangiomatosis. *J Pediatr* 1998;132(6):1057-60.
181. Perisinakis K, Damilakis J, Voloudaki A, Papadakis A, Gourtsoyiannis N. Patient dose reduction in CT examinations by optimising scanogram acquisition. *Radiat Prot Dosimetry* 2001;93(2):173-8.
182. Picot C, Monnet P, Bethenod M, Beraud C, Jaubert de Beaujeu M, Salle B. [Tracheomalacia in infants]. *Arch Fr Pediatr* 1969;26(5):493-506.
183. Piskin E, Dincer S, Turk M. Gene delivery: intelligent but just at the beginning. *J Biomater Sci Polym Ed* 2004;15(9):1181-202.
184. Puig S, Casati B, Staudenherz A, Paya K. Vascular low-flow malformations in children: current concepts for classification, diagnosis and therapy. *Eur J Radiol* 2005;53(1):35-45.
185. Pytowski B, Goldman J, Persaud K, Wu Y, Witte L, Hicklin DJ, et al. Complete and specific inhibition of adult lymphatic regeneration by a novel VEGFR-3 neutralizing antibody. *J Natl Cancer Inst* 2005;97(1):14-21.
186. Ramani P, Shah A. Lymphangiomatosis. Histologic and immunohistochemical analysis of four cases. *Am J Surg Pathol* 1993;17(4):329-35.
187. Ramesh R, Ito I, Saito Y, Wu Z, Mhashikar AM, Wilson DR, et al. Local and systemic inhibition of lung tumor growth after nanoparticle-mediated mda-7/IL-24 gene delivery. *DNA Cell Biol* 2004;23(12):850-7.
188. Randestad A, Lindholm CE, Fabian P. Dimensions of the cricoid cartilage and the trachea. *Laryngoscope* 2000;110(11):1957-61.
189. Ratcliffe J, Swanson CE, Hafiz N, Frawley K, Coakley K, Cloake J. Assessment of image quality of a standard and two dose-reducing protocols in paediatric pelvic CT. *Pediatr Radiol* 2003;33(3):177-82.
190. Rautio R, Keski-Nisula L, Laranne J, Laasonen E. Treatment of Lymphangiomas with OK-432 (Picibanil). *Cardiovasc Intervent Radiol* 2002;25:6.

191. Ravenel JG, Scalzetti EM, Huda W, Garrisi W. Radiation exposure and image quality in chest CT examinations. *AJR Am J Roentgenol* 2001;177(2):279-84.
192. Ravi Kumar MN. Nano and microparticles as controlled drug delivery devices. *J Pharm Pharm Sci* 2000;3(2):234-58.
193. Reed ML, Wu C, Kneller J, Watkins S, Vorp DA, Nadeem A, et al. Micromechanical devices for intravascular drug delivery. *J Pharm Sci* 1998;87(11):1387-94.
194. Riechelmann H, Muehlfay G, Keck T, Mattfeldt T, Rettinger G. Total, subtotal, and partial surgical removal of cervicofacial lymphangiomas. *Arch Otolaryngol Head Neck Surg* 1999;125(6):643-8.
195. Rundback JH, Wright K, McLennan G, Lang E, Sullivan K, Bettmann M, et al. Current status of interventional radiology research: results of a CIRREF survey and implications for future research strategies. *J Vasc Interv Radiol* 2003;14(9 Pt 1):1103-10.
196. Saaristo A, Tammela T, Timonen J, Yla-Herttuala S, Tukiainen E, Asko-Seljavaara S, et al. Vascular endothelial growth factor-C gene therapy restores lymphatic flow across incision wounds. *Faseb J* 2004;18(14):1707-9. Epub 2004 Sep 10.
197. Sato J, Davey BL, Suki B, Bates JH. Oscillatory pressure-flow relationships of canine airways: a steady-state model for different gases. *J Appl Physiol* 1994;76(2):923-32.
198. Sewall GK, Warner T, Connor NP, Hartig GK. Comparison of resorbable poly-L-lactic acid-polyglycolic acid and internal Palmaz stents for the surgical correction of severe tracheomalacia. *Ann Otol Rhinol Laryngol* 2003;112(6):515-21.
199. Shankar KR, Roche CJ, Carty HM, Turnock RR. Cystic retroperitoneal lymphangioma: treatment by image-guided percutaneous catheter drainage and sclerotherapy. *Eur Radiol* 2001;11(6):1021-3.
200. Sheng K, Jeraj R, Shaw R, Mackie TR, Paliwal BR. Imaging dose management using multi-resolution in CT-guided radiation therapy. *Phys Med Biol* 2005;50(6):1205-19. Epub 2005 Mar 2.
201. Shin WS, Szuba A, Rockson SG. Animal models for the study of lymphatic insufficiency. *Lymphat Res Biol* 2003;1(2):159-69.
202. Siegel MJ, Schmidt B, Bradley D, Suess C, Hildebolt C. Radiation dose and image quality in pediatric CT: effect of technical factors and phantom size and shape. *Radiology* 2004;233(2):515-22. Epub 2004 Sep 9.

203. Sinha PK, Dubey PK, Singh S. Identifying tracheomalacia. *Br J Anaesth* 2000;84(1):127-8.
204. Smith RJ, Burke DK, Sato Y, Poust RI, Kimura K, Bauman NM. OK-432 therapy for lymphangiomas. *Arch Otolaryngol Head Neck Surg* 1996;122(11):1195-9.
205. Smith RJ. Lymphatic malformations. *Lymphat Res Biol* 2004;2(1):25-31.
206. Stacker SA, Williams RA, Achen MG. Lymphangiogenic growth factors as markers of tumor metastasis. *Apmis* 2004;112(7-8):539-49.
207. Stein M, Hsu RK, Schneider PD, Ruebner BH, Mina Y. Alcohol ablation of a mesenteric lymphangioma. *J Vasc Interv Radiol* 2000;11(2 Pt 1):247-50.
208. Stern EJ, Graham CM, Webb WR, Gamsu G. Normal trachea during forced expiration: dynamic CT measurements. *Radiology* 1993;187(1):27-31.
209. Sudre-Levillain I, Roman S, Nicollas R, Triglia JM. [Tracheomalacia and tracheal dyskinesias]. *Arch Pediatr* 2001;8(7):757-62.
210. Suess C, Chen X. Dose optimization in pediatric CT: current technology and future innovations. *Pediatr Radiol* 2002;32(10):729-34; discussion 751-4. *Epub* 2002 Aug 29.
211. Suto Y, Tanabe Y. Evaluation of tracheal collapsibility in patients with tracheomalacia using dynamic MR imaging during coughing. *AJR Am J Roentgenol* 1998;171(2):393-4.
212. Suzuki K, Morita T, Tokue A. Vascular endothelial growth factor-C (VEGF-C) expression predicts lymph node metastasis of transitional cell carcinoma of the bladder. *Int J Urol* 2005;12(2):152-8.
213. Takes RP, Valdes Olmos RA, Hilgers FJ, Hoefnagel CA, Bruning PF. Intracystic administration of Tc-99m colloid particles to study retention and drainage in lymphangioma of the neck. *Clin Nucl Med* 1994;19(9):792-4.
214. Tao SL, Desai TA. Microfabricated drug delivery systems: from particles to pores. *Adv Drug Deliv Rev* 2003;55(3):315-28.
215. Tasar F, Tumer C, Sener BC, Sencift K. Lymphangioma treatment with Nd-YAG laser. *Turk J Pediatr* 1995;37(3):253-6.

216. Thomas TP, Patri AK, Myc A, Myaing MT, Ye JY, Norris TB, et al. In vitro targeting of synthesized antibody-conjugated dendrimer nanoparticles. *Biomacromolecules* 2004;5(6):2269-74.
217. Tovi M, Herbreteau D, Enjolras O, Merland JJ. [52 patients with cystic lymphatic vascular malformations. Percutaneous sclerotherapy--simple, fast and repeatable]. *Lakartidningen* 1998;95(7):643-7.
218. Triglia JM, Nicollas R, Roman S, Kreitman B. Tracheomalacia associated with compressive cardiovascular anomalies in children. *Pediatr Pulmonol* 2001;Suppl(23):8-9.
219. Turner C, Gross S. Treatment of recurrent suprahyoid cervicofacial lymphangioma with intravenous cyclophosphamide. *Am J Pediatr Hematol Oncol* 1994;16(4):325-8.
220. Uchida K, Inoue M, Araki T, Miki C, Kusunoki M. Huge scrotal, flank, and retroperitoneal lymphangioma successfully treated by OK-432 sclerotherapy. *Urology* 2002;60(6):1112.
221. Verdun FR, Lepori D, Monnin P, Valley JF, Schnyder P, Gudinchet F. Management of patient dose and image noise in routine pediatric CT abdominal examinations. *Eur Radiol* 2004;14(5):835-41. Epub 2004 Jan 13.
222. Vijayanathan V, Thomas T, Thomas TJ. DNA nanoparticles and development of DNA delivery vehicles for gene therapy. *Biochemistry* 2002;41(48):14085-94.
223. Voldman J, Gray ML, Schmidt MA. Microfabrication in biology and medicine. *Annu Rev Biomed Eng* 1999;1:401-25.
224. Walner DL, Ouanounou S, Donnelly LF, Cotton RT. Utility of radiographs in the evaluation of pediatric upper airway obstruction. *Ann Otol Rhinol Laryngol* 1999;108(4):378-83.
225. Weber DO. Nanomedicine. *Health Forum J* 1999;42(4):32, 36-7.
226. Whitesides GM, Ostuni E, Takayama S, Jiang X, Ingber DE. Soft lithography in biology and biochemistry. *Annu Rev Biomed Eng* 2001;3:335-73.
227. Wildberger JE, Mahnken AH, Schmitz-Rode T, Flohr T, Stargardt A, Haage P, et al. Individually adapted examination protocols for reduction of radiation exposure in chest CT. *Invest Radiol* 2001;36(10):604-11.
228. Wildberger JE, Max M, Wein BB, Mahnken AH, Weiss C, Dembinski R, et al. Low-dose multislice spiral computed tomography in acute lung injury: animal experience. *Invest Radiol* 2003;38(1):9-16.

229. Wimmershoff MB, Schreyer AG, Glaessl A, Geissler A, Hohenleutner U, Feuerbach SS, et al. Mixed capillary/lymphatic malformation with coexisting port-wine stain: treatment utilizing 3D MRI and CT-guided sclerotherapy. *Dermatol Surg* 2000;26(6):584-7.
230. Wojno TH. Sotradecol (sodium tetradecyl sulfate) injection of orbital lymphangioma. *Ophthal Plast Reconstr Surg* 1999;15(6):432-7.
231. Wood RE. Localized tracheomalacia or bronchomalacia in children with intractable cough. *J Pediatr* 1990;116(3):404-6.
232. Wright CD. Tracheomalacia. *Chest Surg Clin N Am* 2003;13(2):349-57, viii.
233. Wunderbaldinger P, Paya K, Partik B, Turetschek K, Hormann M, Horcher E, et al. CT and MR imaging of generalized cystic lymphangiomatosis in pediatric patients. *AJR Am J Roentgenol* 2000;174(3):827-32.
234. Yavuzer R, Latifoglu O, Ataoglu O, Cenetoglu S. Lymphatic malformation or lymphovenous malformation. *Plast Reconstr Surg* 1999;104(5):1579-80.
235. Yi CA, Lee KS, Kim TS, Han D, Sung YM, Kim S. Multidetector CT of bronchiectasis: effect of radiation dose on image quality. *AJR Am J Roentgenol* 2003;181(2):501-5.
236. Youan BB, Benoit MA, Baras B, Gillard J. Protein-loaded poly(epsilon-caprolactone) microparticles. I. Optimization of the preparation by (water-in-oil)-in water emulsion solvent evaporation. *J Microencapsul* 1999;16(5):587-99.
237. Ziaie B, Baldi A, Lei M, Gu Y, Siegel RA. Hard and soft micromachining for BioMEMS: review of techniques and examples of applications in microfluidics and drug delivery. *Adv Drug Deliv Rev* 2004;56(2):145-72.
238. Zinman R. Tracheal stenting improves airway mechanics in infants with tracheobronchomalacia. *Pediatr Pulmonol* 1995;19(5):275-81.
239. Zulfiqar MA, Zaleha AM, Zakaria Z, Amin T. The treatment of neck lymphangioma with intralesional injection of bleomycin. *Med J Malaysia* 1999;54(4):478-81.